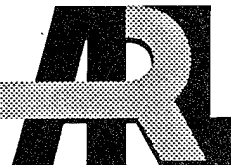ARMY RESEARCH LABORATORY

Multi-Dimensional Simulation of ETC Gun Flowfields

A. Hosangadi
N. Sinha
S. M. Dash

ARL-CR-240

August 1995
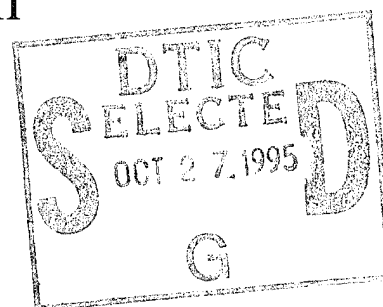
19951026 073

REPORT DOCUMENTATION PAGE

Public reporting burden for this collection of information is estimated to average 1 hour per response, including the time for reviewing instructions, searching existing data sources, gathering and maintaining the data needed, and completing and reviewing the collection of information. Send comments regarding this burden estimate or any other aspect of this collection of information, including suggestions for reducing this burden, to Washington Headquarters Services, Directorate for Information Operations and Reports, 1215 Jefferson Davis Highway, Suite 1204, Arlington, VA 22202-4302, and to the Office of Management and Budget, Paperwork Reduction Project(0704-0188), Washington, DC 20503.

1. AGENCY USE ONLY (Leave blank)	2. REPORT DATE	3. REPORT TYPE AND DATES COVERED
	August 1995	Final, March 1993 - February 1994

4. TITLE AND SUBTITLE	5. FUNDING NUMBERS
Multi-Dimensional Simulation of ETC Gun Flowfields	C: DAAL02-90-0071

6. AUTHOR(S)

A. Hosangadi, N. Sinha, and S. M. Dash

7. PERFORMING ORGANIZATION NAME(S) AND ADDRESS(ES)	8. PERFORMING ORGANIZATION REPORT NUMBER
Science Applications International Corporation Propulsive Sciences Division 501 Office Center Drive, Suite 420 Fort Washington, PA 19034-3211	SAIC/FW TR-121

9. SPONSORING/MONITORING AGENCY NAMES(S) AND ADDRESS(ES)	10.SPONSORING/MONITORING AGENCY REPORT NUMBER
U.S. Army Research Laboratory ATTN: AMSRL-WT-PA Aberdeen Proving Ground, MD 21005-5066	ARL-CR-240

11. SUPPLEMENTARY NOTES

The point of contact for this report is Gloria P. Wren, U.S. Army Research Laboratory, ATTN: AMSRL-WT-PA, Aberdeen Proving Ground, MD 21005-5066.

12a. DISTRIBUTION/AVAILABILITY STATEMENT	12b. DISTRIBUTION CODE
Approved for public release; distribution is unlimited.	

13. ABSTRACT (Maximum 200 words)

Progress made in the development of advanced computational methodology for simulating multi-dimensional processes in ETC guns is described. The CRAFT upwind/implicit Navier-Stokes code has been extended to include complex multiphase capabilities associated with liquid and solid propellant guns. In particular, a gas/bulk liquid equilibrium formulation for liquid propellants and a nonequilibrium Lagrangian fluidized bed formulation for solid propellants has been incorporated along with plasma generation module coupling. Turbulence is simulated using large eddy simulation (LES) methodology. Fundamental studies as well as simulations of liquid and solid propellant ETC gun firings are described.

14. SUBJECT TERMS			15. NUMBER OF PAGES
Navier Stokes (NS) code, combustion, plasma, electrothermal-chemical (ETC) gun, liquid propellant (LP), solid propellant (SP), large eddy simulation (LES), Lagrangian solver, interior ballistics, Roe/TVD numerics, fluidized bed			142
			16. PRICE CODE

17. SECURITY CLASSIFICATION OF REPORT	18. SECURITY CLASSIFICATION OF THIS PAGE	19. SECURITY CLASSIFICATION OF ABSTRACT	20. LIMITATION OF ABSTRACT
UNCLASSIFIED	UNCLASSIFIED	UNCLASSIFIED	UL

INTENTIONALLY LEFT BLANK.

ACKNOWLEDGMENTS

Accesion For		
NTIS CRA&I	☒	
DTIC TAB	☐	
Unannounced	☐	
Justification		
By		
Distribution /		
Availability Codes		
Dist	Avail and / or Special	
A-1		

INTENTIONALLY LEFT BLANK.

TABLE OF CONTENTS

TABLE OF CONTENTS

LIST OF FIGURES

LIST OF FIGURES

LIST OF FIGURES

INTENTIONALLY LEFT BLANK.

MULTI-DIMENSIONAL SIMULATION OF ETC GUN FLOWFIELDS
1.0 INTRODUCTION

This report summarizes progress made to date in the development of advanced computational methodology for simulating multi-dimensional, electrothermal-chemical (ETC) gun flowfields. A research-oriented, first-principles approach was taken which utilized sophisticated, state-of-the-art Roe/TVD upwind/implicit numerics, incorporating the relevant physics and thermochemistry needed to simulate ETC processes in a systematic manner. Our starting point for ETC simulation had involved the use of the "original" CRAFT 3D Navier-Stokes code [1,2] whose applications had been limited to steady-state jet/propulsive flows. CRAFT was an outgrowth of the TUFF 3D Navier-Stokes research code developed by Molvik and Merkle at Penn State [3] under NASA Ames support for hypersonic nonequilibrium flow simulation.

The National AeroSpace Plane (NASP) program prompted the development of a new computational methodology to accurately analyze chemically-reacting flows with strong discontinuities. TUFF was one of three new codes developed and the first that was government-owned. A similar path was taken by Rockwell International Science Center in their development of the "proprietary" USA code [4], and somewhat later by Virginia Polytechnic Institute in the development of the GASP code [5] under NASA Langley support. The "1990's" finite-volume Roe/TVD upwind/implicit numerics that these codes were based upon combined classical "characteristic or Riemann-invariant concepts" with advanced matrix algebra to permit the accurate "capturing" of strong discontinuities (shocks, contact surfaces, flame fronts) in a non-oscillatory manner, without the need for stabilizing artificial-dissipation terms. This "revolutionary" breakthrough in computational fluid dynamics was accompanied by the additional finding that this class of numerics was also optimal for the treatment of "acoustic-driven" problems as exhibited by the research of Beddini and students at the University of Illinois in analyzing combustion instabilities [6].

The ETC gun flowfield problem involves varied disciplines as schematized in Figure 1.1 which shows the ingredients that the CRAFT code required for simulation. From a numerical viewpoint, requisite baseline ingredients were already in place. The Roe/TVD formulation that CRAFT already contained, provided the ability to both capture strong discontinuities

PHYSICS
- LES Turbulence
- Plasma Coupling
- Projectile Aero

THERMOCHEMICAL
- Viral EOS
- Liquid EOS

CRAFT CODE NUMERICAL FRAMEWORK
- Conservative, Upwind, Non-Dissipative
  - Instabilities
- Stongly-Coupled/Implicit Treatment of Noneq. Source Terms
- Generalized Non-Reflective, Riemann Based Boundary Conditions

GRID
- Dynamic/Adaptive Gridding
- Grid Embedding
- Grid Blanking

MULTI-PHASE
- Equilibrated Mixtures
- Multi-phase Noneq.
  - Eulerian
  - Lagrangian
- Droplet Formation
- Particle Burning

Figure 1.1. ETC gun disciplines embodied in CRAFT Navier-Stokes code.

in a non-oscillatory manner, and, to produce solutions of near-acoustic accuracy with negligible numerical dissipation. Earlier numerical schemes (FCT, MacCormack) did not provide this requisite behavior. A second principal ingredient is the "fully" implicit numerics — convective/diffusive/source terms and boundary conditions are all treated implicitly which provides full-coupling of equations throughout the flow domain. A question raised in the course of this work was the requirement to use a fully-implicit procedure for the analysis of time-accurate flows where large Courant numbers could degrade the solution. The answer resided in the need to adequately resolve all flow regions and thus use a non-uniform grid where cell volumes could vary by orders of magnitude. An implicit code can operate at an "average" Courant number of unity, minimizing wave dispersion errors. An explicit code is restricted to operate at a Courant number of unity for the smallest cells. All other cells will operate well below unity and hence, the averaged Courant number can be significantly less than one which degrades the solution.

2

The inclusion of the requisite physical, thermodynamic, multiphase and combustion modeling parameters into CRAFT for ETC simulation have involved very significant extensions, as have the specialized numerical upgrades required to simulate the dynamic interior ballistic environment. It has been opportune to have had synergistic programs with several other government agencies. These have provided a framework for "piggy-backing" the varied developments achieved in applying CRAFT to several different problem areas. In addition to CRAFT developmental support from the U.S. Army Research Laboratory for ETC gun simulation (and most recently, for LPG investigations – Ref. 7), additional support was provided by:

- U.S. Army Missile Command (MICOM), Redstone Arsenal, AL, for tactical missile aero/propulsive simulation [8-20].

- Naval Surface Warfare Center (NSWC), Dahlgren, VA, for missile vertical launcher system simulation [21-24].

- Air Force Office of Scientific Research (AFOSR)/Phillips Lab-Armament Directorate, Eglin AFB, FL, for ram accelerator simulation [25-28].

- NASA Langley Research Center, Hampton, VA, for jet/acoustics research [29-36].

- Air Force Wright Laboratory, Wright-Patterson AFB, OH, for simulation of aircraft plume/wake interactions for signatures and countermeasures [15, 37-38].

The specific extensions to CRAFT in the areas of numerics, thermochemistry, multiphase flow, and turbulence over the past 5 years is summarized below in Tables I to IV, respectively, including the principal funding agency for each extension. The CRAFT ETC developmental work has entailed problem-specific extensions to CRAFT, such as direct-coupling with a plasma capillary model, and varied extensions involving shared technology such as large eddy simulation (LES) turbulence modeling for liquid propellants (shared with jet/acoustic simulation activities) and Lagrangian particulate modeling for solid propellants (shared with solid rocket motor simulation activities).

In the course of developing varied CRAFT extensions, ETC concepts were changing rapidly — often, faster than developments could keep pace with. Our starting point in ETC simulation involved analyzing a liquid

Table I. CRAFT Extensions / Numerics

(Gantt-style timeline chart, 1990–1995)

- Full Stress Terms (NASP)
- Dynamic Grids (ARL)
- Patching (MICOM)
- Embedding (ARL)
- Generalized BC's (MICOM)
- Thermal Coupling (AFOSR)
- Hybrid Str'd/Unstr'd (MICOM)
- Spatial Option (MICOM)
- Structural Coupling (ARL)
- Preconditioning (MICOM)

1990 1991 1992 1993 1994 1995
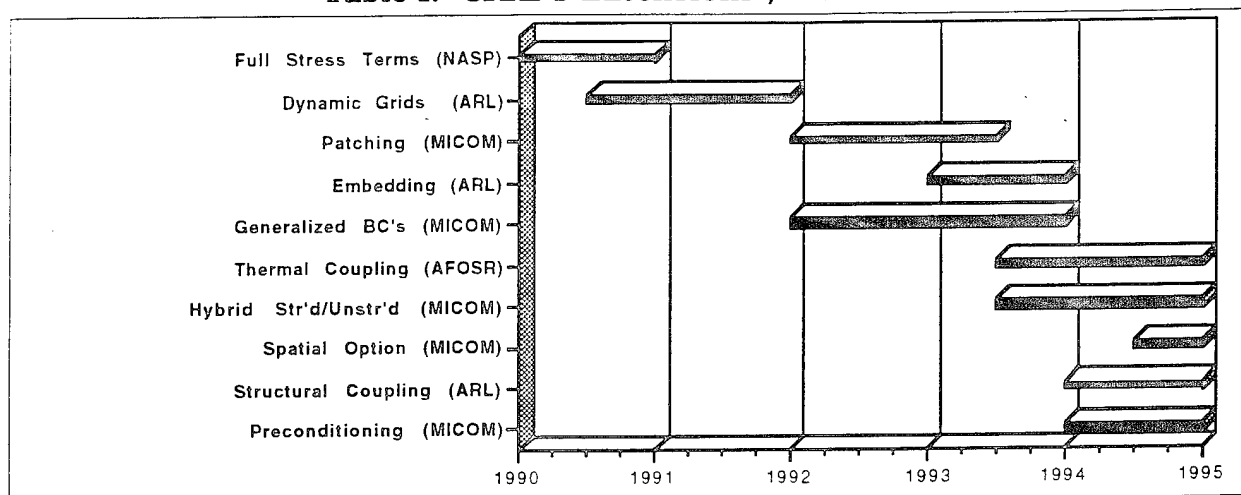
Table II. CRAFT Extensions / Thermochemistry

(Gantt-style timeline chart, 1990–1995)

- Generalized Hydrogen-Air Chemistry (MICOM)
- Virial Equation of State (ARL)
- Backward JANNAF Reaction Rate (MICOM)
- One Step, Infinite Rate Chemistry (MICOM)
- Pressure Dependent Droplet Combustion (ARL)
- Plasma Module Coupling (ARL)

1990 1991 1992 1993 1994 1995
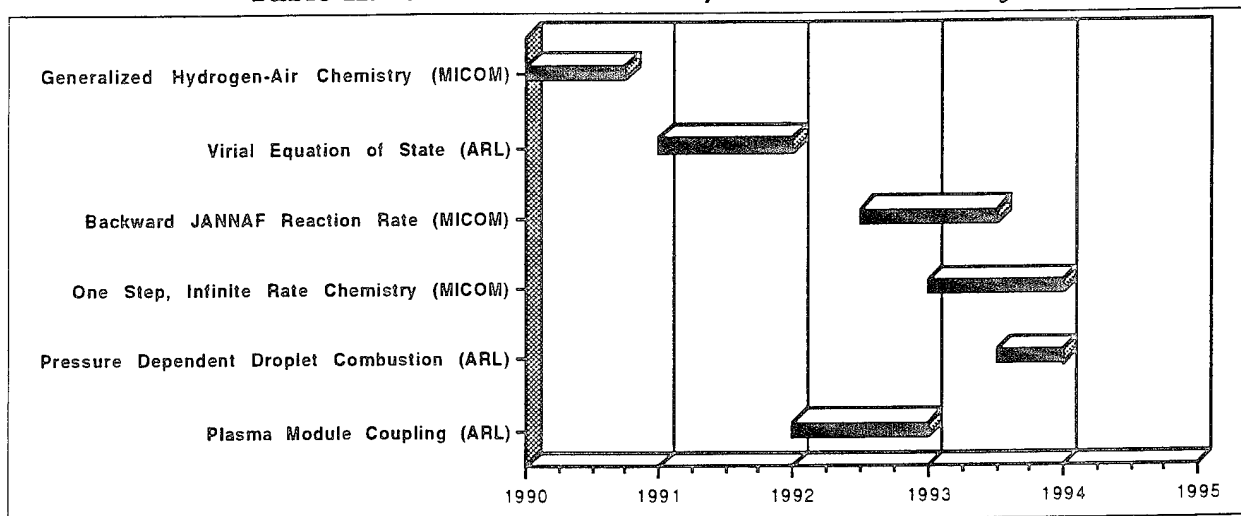
Table III. CRAFT Extensions / Multiphase Flow

(Gantt-style timeline chart, 1990–1995)

- Eulerian/NS (NSWC/MICOM)
- Eulerian/PNS (MICOM)
- Lagrangian: Dilute/NS (MICOM)
- Lagrangian: Non-Dilute/NS (ARL)
- Surface Interactions (NSWC)
- Bulk Liquid (ARL)
- Gas/Liquid (ARL)
- Droplet/Particle Combustion (ARL)
- Fluidized Beds/Propellant Grains (ARL)

1990 1991 1992 1993 1994 1995

4
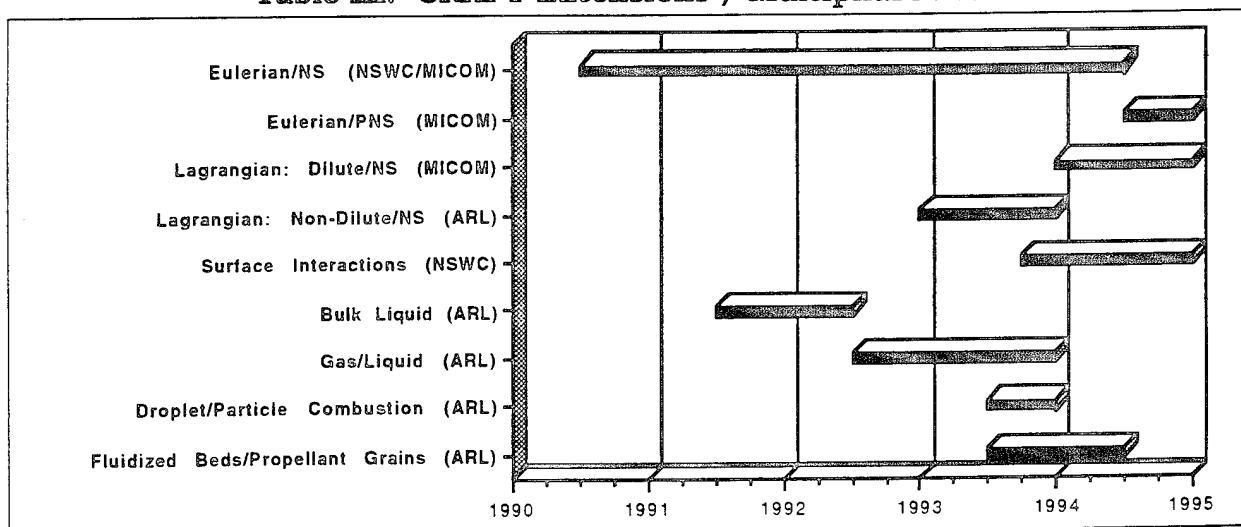
Table IV. CRAFT Extensions / Turbulence

Basic ke Model (NASP)
Chien Near Wall (MICOM)
kW Model (NASA)
ke/Pope Correction (NASA)
keCD Modification (NASA)
LES (NASA/ARL/AFOSR)
Reynolds Stress (NASA)
Scalar Fluctuations (USAF)

1990 1991 1992 1993 1994 1995
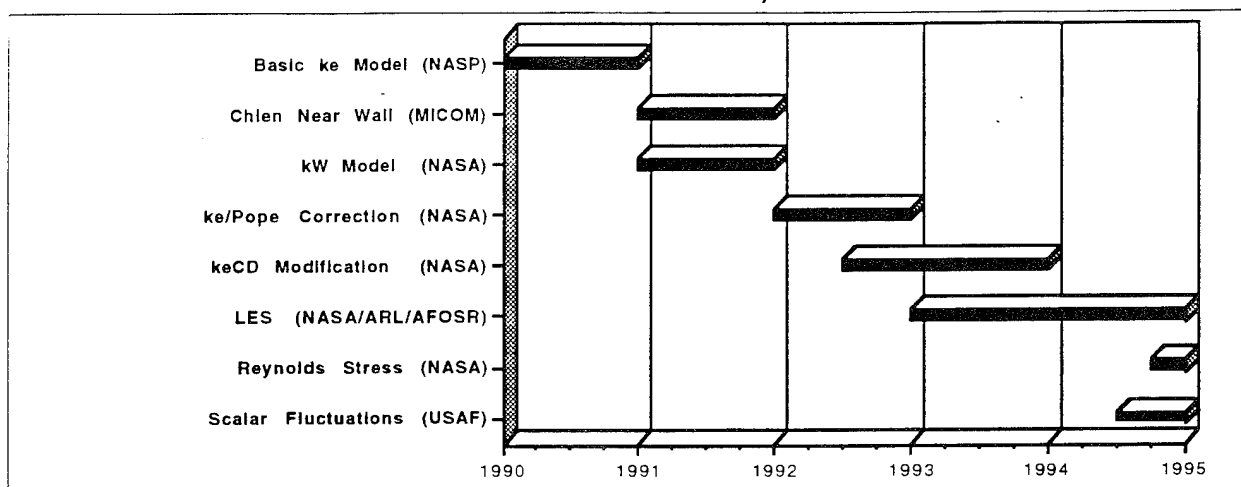
propellant working fluid with end injection of the plasma. This changed to analysis of central ullage tube concepts with "burst-start," and piccolo tube variants. Liquid propellant extensions focussed on the inclusion of gas/liquid interactions and combustion modeling capabilities into CRAFT, and, on simulating the large-scale turbulent structure for which LES methodology was found to be extremely promising.

As our work with liquid propellants started to show great promise, propellant concepts changed and we had to shift gears quite rapidly to extend CRAFT to deal with solid propellant ETC guns. Early work entailed a simplified fixed-bed representation of the solid propellant. This was extended to a sophisticated fluidized bed representation using a Lagrangian formulation which treated the interactions (fluid/thermal) of each deterred propellant ball discretely. The new formulation in CRAFT was shown to accurately simulate solid propellant interior ballistic flows via detailed unit problem comparative studies with XKTC described in Ref. 39.

Our work to date in simulating ETC gun flowfields with CRAFT has been described in a number of JANNAF Combustion Subcommittee Meeting papers and related workshop presentations [40-47]. This report will provide a unified description of this work, presenting more global details of the numerical methodology not heretofore documented. An overview of CRAFT as a general purpose interior ballistics flowfield solver with applications to ETC, LPG and RAMAC problems; to venting/muzzle blast; and, to projectile flyout and thermal heating, is described in Ref. 48.

5

2.0 CRAFT CODE OVERVIEW AND SELECTED STUDIES

2.1 OVERVIEW OF METHODOLOGY AND FEATURES

Interior ballistic flowfields share common problems of transient combustion with complex wave processes. The CRAFT code has been applied to simulate interior ballistic flowfields encompassing electrothermal (ETC) guns, liquid propellant (LP) guns, and ram accelerators (as well as to simulate other propulsive-oriented problems as discussed earlier). The present overall features of the CRAFT code are listed below in Table V.

Table V. CRAFT Code Features

NUMERICS	• 1D/2D/AXI/3D Finite-Volume Discretization
	• Implicit, Higher-Order Upwind (Roe/TVD) Formulation
	• Fully Implicit Source Terms/Boundary Conditions
GRID FEATURES	• Grid Dynamics to Account for Moving Boundaries
	• Grid Patching/Blanking for Complex Geometries
	• Solution-Adaptive Gridding
	• Hybrid Structured/Unstructured Formulation for Multi-Body Problems
THERMO-CHEMISTRY	• Real Gas Mixtures (Calorically and Thermally Imperfect/JANNAF Thermo Tables/Virial EOS)
	• Finite-Rate Chemistry/Arbitrary Number of Species and Reactions
	• Fully Implicit Source Term Linearization
MULTI-PHASE FLOW	• Nonequilibrium Particle/Droplet Solvers (Eulerian and Lagrangian Formulations)
	• Gas/Liquid Equilibrium Formulation
	• Grain/Ablative Coupling Including Surface Recession and Interior Burning
HEAT/MASS TRANSFER & VIBRATION	• Coupling with 3D Transient Heat Conduction Solution
	• Generalized Mass Transfer Boundary Conditions and Phase-Change
	• Coupling with 3D Structural Solver (in Progress)
TURBULENCE	• k-ε Formulation with Compressibility/Vortical Upgrades and Several Low Re Near-Wall Formulations
	• LES Subgrid Scale Models of Menon and Madabhushi
	• Particle Dispersion Formulations
APPLICATIONS	• Electrothermal Chemical (ETC) Gun – Liquid and Solid
	• Regenerative Liquid Propellant Gun (RLPG)
	• Ram Accelerator
	• Solid/Liquid Propellant Rocket Motors/Exhausts
	• Ducted Rocket
	• Vertical Launcher Interactions
	• Turbulence/Multi-Phase Jet Research

CRAFT is structured in a finite volume framework and utilizes implicit/upwind numerics which entails sophisticated and complex matrix multiplications. While transient interior ballistic flowfield problems have

6

traditionally used explicit numerics, the viewpoint taken here is that implicit numerics are <u>requisite</u> to analyze problems with highly non-uniform geometric scales. Turbulent scales in near-wall regions require grids whose cell volumes are orders of magnitude smaller than average cell volumes. Explicit solvers are restricted by stability limitations to operate at time steps associated with the smallest cell volume. Hence, wave processes will suffer from substantive dispersive errors via operating at very small Courant numbers. Implicit numerics avoid such limitations and provide additional stability for complex combusting flows. The Riemann based upwind numerical flux computation procedure is chosen since it permits the accurate representation of strong gradients and discontinuities (e.g. shocks, flame fronts, propellant grain-ullage boundaries) by aligning the numerical stencil with wave/convective directions via matrix manipulations. Consequently these discontinuities are captured sharply without the characteristic oscillations associated with earlier schemes which typically require the use of artificial dissipation terms to suppress these spurious oscillations.

The thermochemistry in the CRAFT code has been enhanced from the original gas-phase capability to include gas-liquid mixtures with a discrete phase of either droplets or propellant grains. The modelling of complex thermochemistry associated with mixtures of gas, bulk liquid and liquid/ solid particulates within this upwind numerical framework has required significant developmental work to the code and will be described in the sections that follow. A number of enhanced grid capabilities such as grid dynamics, grid blanking, and grid embedding have been incorporated to better handle complex geometries whose volumes change and deforms in time. The treatment of turbulence in CRAFT is a major philosophical departure from previous interior ballistic codes. For the highly transient flowfields of interest here, we simulate turbulence using a large-eddy scale (LES) approach where large vortical structures are captured as part of the unsteady flow computation and only the subscale turbulence effects are modeled. We note that the development of the code has proceeded in a systematic fashion wherein each additional upgrade has been incorporated as necessitated, guided by experimental data and emphasizing an improved understanding of the physical phenomena. In the sections to follow, we will describe the above features and methodology in detail. In the next section,

we will describe the basic numerical framework and upwind flux algorithm as designed originally for ideal gas mixtures. Thermochemical upgrades required to allow for treatment of non-ideal gases and gas-liquid mixtures within the original upwind framework are described in the subsequent section.

2.2 FINITE-VOLUME FRAMEWORK AND ORIGINAL GAS PHASE EQUATIONS FOR MULTI-SPECIES, COMBUSTING FLOWS

The conservation equations for multi-species gas flows may be written in an integral form for an arbitrary control-volume as follows:

$$\frac{\partial}{\partial t} \int_V Q dV + \int_S \bar{n} \circ \bar{F} dS = \int_V D dV \qquad (2.2.1)$$

where V is the volume of the control volume, $\bar{n} \circ dS$ is a vector element of the control surface with outward normal $\bar{n}$, $\bar{F}$ represents both the inviscid and viscous flux of the conserved quantities Q through the control surfaces, and D contains any source terms. In a finite volume framework, the arbitrary control-volume is replaced with a generalized six sided cell as shown in Figure 2.2.1 for both a Cartesian and polar coordinate system. For this gen-
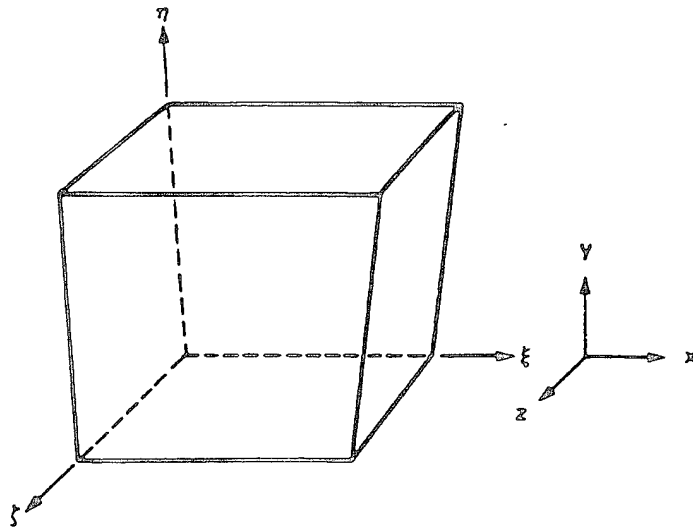
Fig. 2.2.1. Three-dimensional finite-volume cell.

eralized cell volume, the flux quantity in Eq. (2.2.1) is rewritten as an integral over each face thereby yielding

8

$$\frac{\partial}{\partial t}\iiint Q\,dV + \iint\left(E_{i+1/2} - E_{i-1/2}\right)d\eta\,d\zeta$$

$$+\iint\left(F_{j+1/2} - F_{j-1/2}\right)d\xi\,d\zeta + \iint\left(G_{k+1/2} - G_{k-1/2}\right)d\xi\,d\eta$$

$$=\frac{1}{Re}\iint\left(R_{i+1/2} - R_{i-1/2}\right)d\eta\,d\zeta + \frac{1}{Re}\iint\left(S_{j+1/2} - S_{j-1/2}\right)d\xi\,d\zeta$$

$$+\frac{1}{Re}\iint\left(T_{k+1/2} - T_{k-1/2}\right)d\xi\,d\eta + \iiint D\,dV$$

(2.2.2)

Here, ξ is the generalized streamwise coordinate, η is the normal coordinate, and ζ is the meridional coordinate. The indices i,j,k represent the cell location. The vector Q contains the conservation variables which are defined at the center of the cell i,j,k. The fluxes are defined at the cell interfaces which are represented by non-whole indices. The vectors E,F, and G represent the inviscid flux through the cell interfaces in the ξ, η, and ζ directions, respectively. R, S, and T are the respective viscous stress/transport vectors, and D contains source terms resulting from combustion. We note that since the finite-volume formulation works with the physical cell surface and volume, we are able to solve for 1D, 2D/AXI, or 3D flows within a single unified code by supplying the appropriate control volumes. Hence, even for a 2D/AXI flow, two grid planes in the azimuthal direction are defined thereby providing a physical volume to the grid cells.

For a gas mixture of multi-component species, the conserved variable Q and the inviscid fluxes are defined as follows:

$$
Q = \begin{bmatrix} \rho \\ \rho u \\ \rho v \\ \rho w \\ e \\ \rho_i \\ \vdots \\ \rho_{n-1} \end{bmatrix}; \quad
E = \begin{bmatrix} \rho U \\ (\rho Uu + \ell_x P) \\ (\rho Uv + \ell_y P) \\ (\rho Uw + \ell_z P) \\ (e+P)U \\ \rho_i U \\ \vdots \\ \rho_{n-1} U \end{bmatrix}; \quad
F = \begin{bmatrix} \rho V \\ (\rho Vu + m_x P) \\ (\rho Vv + m_y P) \\ (\rho Vw + m_z P) \\ (e+P)V \\ \rho_i V \\ \vdots \\ \rho_{n-1} V \end{bmatrix}; \quad
G = \begin{bmatrix} \rho W \\ (\rho Wu + n_x P) \\ (\rho Wv + n_y P) \\ (\rho Ww + n_z P) \\ (e+P)W \\ \rho_i W \\ \vdots \\ \rho_{n-1} W \end{bmatrix}
$$

(2.2.3)

The metric quantities ℓ_x, ℓ_y, and ℓ_z are components of the cell face normal L pointing in the ξ direction with magnitude equal to the cell face area. Similarly, the other metric quantities are the components of the vectors M and N, which are the normal vectors to the other families of the cell faces. The quantity U denotes the volume of the flux through the cell face in the ξ direction and is defined as $U = \ell_x u + \ell_y v + \ell_z w$, while V and W are the corresponding volume fluxes through the η and ζ faces. The first five equations solve for the conservation of the mixture mass (ρ), momentum, and total energy per unit volume (e). The subsequent equations solve for the partial densities of (n-1) chemical species (different species that are accounted for). The nth species is partial density, ρ_n, determined by the following mass balance for the mixture density:

$$\sum_{s=1}^{n-1} \rho_s + \rho_n = \rho \qquad (2.2.4)$$

The equation of state for the gaseous mixture follows Dalton's law of partial pressures and is written as follows:

$$P = \frac{\rho \bar{R} T}{M} \qquad (2.2.5)$$

Here, M is the mixture molecular weight which is obtained from the individual species molecular weights as given below

$$M = \left(\sum_{s=1}^{n} \frac{c_s}{M_s} \right)^{-1} \qquad (2.2.6)$$

Here, c_s is the mass fraction of the sth species ($= \rho_s / \rho$).
The expression for the total internal energy is given by

$$e = \rho \left[h + \frac{\left(u^2 + v^2 + w^2 \right)}{2} \right] - P \qquad (2.2.7)$$

where the enthalpy of the mixture, h, is determined by summing the enthalpies of the individual species as follows:

$$h = \sum_{s=1}^{n} c_s \left(h_s^{of} + h_s \right) \qquad\qquad \textbf{(2.2.8)}$$

Note that the individual species enthalpy includes the heat of formation, h_s^{of}, in addition to the sensible enthalpy, h_s. Consequently, the energy conservation equation does not contain a separate heat release source term since this is implicitly defined through the heat of formation for each species. This point will be further clarified in the next section, when we discuss the thermochemistry and temperature decode procedure. We note, as Eq. (2.2.5) indicates, that CRAFT was originally configured to model thermally-perfect gas mixtures only. The extensions to include thermally-imperfect virial equations of state and a gas-liquid equilibrium formulation will be described in a later section.

2.3   GAS-PHASE THERMOCHEMISTRY AND TEMPERATURE DECODING

The thermochemistry within the CRAFT code allows for analyzing a mixture of calorically imperfect gas species. Hence, the sensible enthalpy and specific heat of each species are allowed to vary as functions of temperature as denoted below

$$h_s = h_s(T)$$

$$C_{P,s} = \frac{dh_s}{dT} = C_{P,s}(T) \qquad\qquad \textbf{(2.3.1)}$$

In the code, the enthalpy and specific heat are specified in tabular form as functions of temperature. These tabular values are then fitted with a cubic spline to obtain a generalized functional relationship for the thermochemistry over the entire temperature range.

To complete the thermochemical specification, we still have to decode the temperature of the gas mixture for given values of internal energy and species concentrations. Since, the enthalpy of each species is itself a function of temperature, the internal energy becomes an implicit function of temperature. Therefore, we have to resort to an iterative procedure to decode the temperature from the thermodynamic internal energy (ε) and the mass fractions of the species. A Newton-Raphson procedure was adapted which is illustrated below,

$$\varepsilon = g\left(T^k\right) = \sum_{s=1}^{n} c_s \left[h_s^{of} + h_s\left(T^k\right)\right] - \frac{\overline{R}T^k}{M_s}$$

$$g'\left(T^k\right) = \sum_{s=1}^{n} c_s \left[C_{P,s}\left(T^k\right)\right] - \frac{\overline{R}}{M_s} \qquad\qquad (2.3.2)$$

$$T^{k+1} = T^k - \frac{g\left(T^k\right) - \varepsilon}{g'\left(T^k\right)}$$

Here, the index k corresponds to the Newton-Raphson iterative index. The iterations are continued until convergence is achieved i.e. the thermodynamic internal energy is matched for a given temperature value. We note that for a combusting case, the differences in the heat of formation between the reactants and products ensures the correct heat release and temperature increase, while ensuring that the internal energy is conserved exactly.

2.4 RELEVANT MATRIX ALGEBRA

As a precursor to our discussion of the upwind flux methodology and the implicit solution procedure, we will introduce some of the relevant matrix manipulations and their physical interpretations in this section. To simplify the algebra, we will deal with the one-dimensional inviscid subset of Eq. (2.2.2) given below in its differential form,

$$\frac{\partial Q}{\partial t} + \frac{\partial E}{\partial \xi} = 0 \qquad\qquad (2.4.1)$$

While Eq. (2.4.1) does not contain the viscous terms or the chemical source terms, it is still adequate for the purpose of mathematically describing the wave characteristics of the system. We begin by defining the Jacobian of the flux vector E as follows:

$$A(Q) = \frac{\partial E(Q)}{\partial Q} \qquad\qquad (2.4.2)$$

The Jacobian, A, can also be viewed as a transformation matrix to linearize the non-linear flux vector, E, in time as per Eq. (2.4.3) below

$$E^{n+1} = E^n + \frac{\partial E^n}{\partial Q}\frac{\partial Q}{\partial t}\Delta t$$

$$\therefore E^{n+1} = E^n + A^n \Delta Q \left[\Delta Q = Q^{n+1} - Q^n\right] \qquad\qquad (2.4.3)$$

12

Using Eq. (2.4.2), we rewrite Eq. (2.4.1) in its non-conservative form:

$$\frac{\partial Q}{\partial t} + A\frac{\partial Q}{\partial \xi} = 0 \qquad (2.4.4)$$

Note that in Eq. (2.4.4), the mass, momentum and energy equations remain strongly coupled to each other since the Jacobian A is a full matrix. Therefore, to obtain the individual wave systems in the full system of equations we have to decouple the components in Eq. (2.4.4).

The system of equations in Eq. (2.4.4) are decoupled via the right and left eigenvectors of the Jacobian, A. We define a matrix, L, which contains the left eigenvectors of the Jacobian, A, while its inverse contains the right eigenvectors, R. By definition,

$$LAR = \Lambda \qquad (2.4.5)$$

where the matrix Λ contains the eigenvalues of the Jacobian, A. To decouple the equation system in Eq. (2.4.4) we premultiply it by the matrix L

$$L\frac{\partial Q}{\partial t} + LARL\frac{\partial Q}{\partial \xi} = 0 \qquad (2.4.6)$$

Defining a new vector $d\hat{Q} = LdQ$, Eq. (2.4.6) may be written as

$$\frac{\partial \hat{Q}}{\partial t} + \Lambda\frac{\partial \hat{Q}}{\partial \xi} = 0 \qquad (2.4.7)$$

In Eq. (2.4.7), the individual equations of the system are now decoupled from each other since Λ is a diagonal matrix. Physically, each individual equation is now a mathematical representation of a propagating wave whose propagation speed is its eigenvalue and the quantity that is conserved by the wave is the Riemann invariant $\hat{Q}$.

For the full system of equations in Eq. (2.2.3) the Jacobian, A, for the flux vector E is given below

1 3

$$\hat{A} = \begin{bmatrix}
0 & \ell_x & \ell_y & \ell_z & 0 & 0 & 0 & \cdots & 0 \\[4pt]
-Uu + \ell_x\frac{\partial p}{\partial \rho} & U + \ell_x u + \ell_x\frac{\partial p}{\partial \rho u} & \ell_y u + \ell_x\frac{\partial p}{\partial \rho v} & \ell_z u + \ell_x\frac{\partial p}{\partial \rho w} & \ell_x\frac{\partial p}{\partial e} & \ell_x\frac{\partial p}{\partial \rho_1} & \ell_x\frac{\partial p}{\partial \rho_2} & \cdots & \ell_x\frac{\partial p}{\partial \rho_{n-1}} \\[4pt]
-Uv + \ell_y\frac{\partial p}{\partial \rho} & \ell_x v + \ell_y\frac{\partial p}{\partial \rho u} & U + \ell_y v + \ell_x\frac{\partial p}{\partial \rho v} & \ell_z v + \ell_y\frac{\partial p}{\partial \rho w} & \ell_y\frac{\partial p}{\partial e} & \ell_y\frac{\partial p}{\partial \rho_1} & \ell_y\frac{\partial p}{\partial \rho_2} & \cdots & \ell_y\frac{\partial p}{\partial \rho_{n-1}} \\[4pt]
-Uw + \ell_z\frac{\partial p}{\partial \rho} & \ell_x w + \ell_z\frac{\partial p}{\partial \rho u} & \ell_y w + \ell_z\frac{\partial p}{\partial \rho v} & U + \ell_z w + \ell_z\frac{\partial p}{\partial \rho w} & \ell_z\frac{\partial p}{\partial e} & \ell_z\frac{\partial p}{\partial \rho_1} & \ell_z\frac{\partial p}{\partial \rho_2} & \cdots & \ell_z\frac{\partial p}{\partial \rho_{n-1}} \\[4pt]
-UH + \frac{\partial p}{\partial \rho}U & \ell_x H + U\frac{\partial p}{\partial \rho u} & \ell_y H + U\frac{\partial p}{\partial \rho v} & \ell_z H + U\frac{\partial p}{\partial \rho w} & \left(1 + \frac{\partial p}{\partial e}\right)U & \frac{\partial p}{\partial \rho_1}U & \frac{\partial p}{\partial \rho_2}U & \cdots & \frac{\partial p}{\partial \rho_{n-1}}U \\[4pt]
-c_1 U & c_1 \ell_x & c_1 \ell_y & c_1 \ell_z & 0 & U & 0 & \cdots & 0 \\[4pt]
c_2 U & c_2 \ell_x & c_2 \ell_y & c_2 \ell_z & 0 & 0 & U & \cdots & 0 \\[4pt]
\vdots & \vdots & \vdots & \vdots & \vdots & \vdots & \vdots & \ddots & \vdots \\[4pt]
-c_{n-1} U & c_{n-1} \ell_x & c_{n-1} \ell_y & c_{n-1} \ell_z & 0 & 0 & 0 & \cdots & U
\end{bmatrix} \quad (2.4.8)$$

Similar expressions follow for Matrices B and C where $B = \partial F / \partial Q$ and $C = \partial G / \partial Q$. These matrices are written in a generalized form accommodating the analysis of arbitrary thermodynamics. The algebra involved in determining matrix elements entails making derivatives of the pressure with respect to various conservation quantities e.g., $\frac{\partial p}{\partial \rho} \cdot \frac{\partial p}{\partial e}$, etc. This is where the mixture thermodynamics comes in. Since the matrices are cast in generalized form, the inclusion of complex thermodynamics is straightforward and is performed "off-line." The details of this derivation for a mixture of calorically perfect gases are given in the paper by Molvik and Merkle [3]. The corresponding derivation for a gas-liquid mixture will be described in later subsection of this section.

The eigenvalues of the Jacobian defined in Eq. (2.4.8) are represented as

$$\Lambda = DIAG.(U + C, U - C, U, \ldots, U)$$
$$U = \ell_x u + \ell_y v + \ell_z w \qquad (2.4.9)$$
$$C = c\sqrt{\ell_x^2 + \ell_y^2 + \ell_z^2}$$

where c is the sound speed of the gaseous mixture and is defined as

$$c = \sqrt{\frac{\gamma_m p}{\rho}} \qquad (2.4.10)$$

The eigenvalues in Eq. (2.4.9) are associated with acoustic waves traveling in opposite directions propagating pressure information at the speed of sound, and with the waves convecting at the speed of the fluid transporting scalar quantities such as entropy and chemical species. The elements of the right and left eigenvectors for these eigenvalues are described in Ref. 3.

2.5   UPWIND FLUX COMPUTATION

The inviscid fluxes the cell interfaces are calculated via an approximate Riemann procedure described by Roe [49]. In this approach, the flux is computed as the sum of the contributions of individual waves crossing the boundary. The contribution of each individual wave takes its propagation direction into account thus providing the upwind characteristics to the scheme. The flux at a cell interface, i+1/2, in the ξ direction (see Figure 2.2.1) is given below

$$E_{i+1/2} = \frac{1}{2}\left[E_i + E_{i+1} + \Delta E^-_{i+1/2} - \Delta E^+_{i+1/2}\right] + \textit{Higher Order Fluxes} \qquad \textbf{(2.5.1)}$$

Here, ΔE^+ and ΔE^- represent the flux changes associated with waves traveling in the positive and negative directions respectively. The direction of travel for each wave is obtained from the eigenvalues as discussed earlier. The flux differences ΔE^+ and ΔE^- are defined as

$$\Delta E^{\pm}_{i+1/2} = \frac{1}{2}\left[R_{i+1/2}(\Lambda \pm |\Lambda|)_{i+1/2} L_{j+1/2}\right](Q_{i+1} - Q_i) \qquad \textbf{(2.5.2)}$$

where the matrix $\Lambda \pm |\Lambda|$ serves as an effective filter to distinguish between positive and negative traveling waves.

A higher order inviscid flux is obtained by adding corrective terms to the first order flux in Eq. (2.5.1). Since higher order corrections can induce spurious oscillations, these terms are checked to ensure that they satisfy the Total Variation Diminishing (TVD) criteria [50]. The higher order flux is written as

$$E^{HO}_{i+\frac{1}{2}} = E^{1^{st}}_{i+\frac{1}{2}}$$

$$-R_{i+\frac{1}{2}} \Lambda^-_{i+\frac{1}{2}} \left\{ \frac{1-\phi}{4}\left[\Delta\tilde{\alpha}_{i+\frac{3}{2}}\right] + \frac{1-\phi}{4}\left[\Delta\tilde{\alpha}_{i+\frac{1}{2}}\right] \right\}$$

$$+R_{i+\frac{1}{2}} \Lambda^+_{i+\frac{1}{2}} \left\{ \frac{1-\phi}{4}\left[\Delta\tilde{\alpha}_{i+\frac{1}{2}}\right] + \frac{1-\phi}{4}\left[\Delta\tilde{\tilde{\alpha}}_{i-\frac{1}{2}}\right] \right\} \qquad \textbf{(2.5.3)}$$

where $\phi=1/3$ for a third order scheme. The characteristic variable difference, $(\Delta\alpha)$, is the quantity which is checked for TVD criteria. The characteristic variable is defined as

$$\Delta\alpha_{i+1/2} = L_{i+1/2}\left(Q_{i+1} - Q_i\right) \qquad \textbf{(2.5.4)}$$

The flux limiters are defined using minmod operators as follows:

$$\left(\tilde{\circ}\right)_{i+1/2} = \text{minmod}\left[(\circ)_{i+1/2}, \beta(\circ)_{i-1/2}\right]$$

$$\left(\tilde{\circ}\right)_{i+1/2} = \text{minmod}\left[(\circ)_{i+1/2}, \beta(\circ)_{i+3/2}\right] \qquad \textbf{(2.5.5)}$$

where the minmod operator is defined as

$$\text{minmod}[x, y] = \text{sign}(x) * \max\left[0, \min\{|x|, y*\text{sign}(x)\}\right] \qquad \textbf{(2.5.6)}$$

and β is the compression parameter that is restricted to lie in the range

$$1 < \beta < \frac{3-\phi}{1-\phi} \qquad \textbf{(2.5.7)}$$

For additional details on TVD schemes the reader is referred to Ref. 50.

2.6 IMPLICIT SOLUTION PROCEDURE

To formulate the implicit solution procedure, we begin by linearizing the inviscid flux terms, the viscous terms, and the source terms with respect to the conserved variables Q. The linearized terms, when combined, yield a sparse block-pentadiagonal matrix for 2D cases and a block-septadiagonal matrix for 3D problems. These sparse matrices are not inverted ex-

actly since it is computationally expensive, but instead an approximate Alternate-Direction-Implicit (ADI) procedure is employed. The linearization procedure for the inviscid flux terms and the resulting ADI operator are described below.

The first order linear flux in Eq. (2.5.1) is rewritten as

$$E_{i+1/2}^{n+1} = \frac{1}{2}\left[E_{i+1}^{n+1} + E_i^{n+1}\right] + \left(A^- - A^+\right)_{i+1/2}\left(Q_{i+1}^{n+1} - Q_i^{n+1}\right) \qquad (2.6.1)$$

where

$$A_{i+1/2}^- = \left(R\Lambda^- L\right)_{i+1/2}$$

$$A_{i+1/2}^+ = \left(R\Lambda^+ L\right)_{i+1/2} \qquad (2.6.2)$$

Linearizing Eq. (2.6.1) by making use of Eq. (2.4.3) we obtain

$$E_{i+1/2}^{n+1} = E_{i+1/2}^n + \frac{1}{2}\left[A_{i+1}^n + \left(A^- - A^+\right)_{i+1/2}^n\right]\Delta Q_{i+1} + \frac{1}{2}\left[A_i^n + \left(A^- - A^+\right)_{i+1/2}^n\right]\Delta Q_i$$

$$= E_{1+1/2}^n + \left(A^R\right)_{i+1/2}\Delta Q_{i+1} + \left(A^L\right)_{i+1/2}\Delta Q_i \qquad (2.6.3)$$

where ΔQ is the change in the conserved variable and is defined as

$$\Delta Q_i = \left(Q_i^{n+1} - Q_i^n\right) \qquad (2.6.4)$$

The flux terms in the η and ζ directions can similarly be linearized to yield expressions corresponding to Eq. (2.6.1). The viscous terms and the chemical source terms can be linearized in a similar fashion as well. For the sake of notational simplicity, we will denote the linearized Jacobians for these terms as W without going into the details which are provided in Ref. 3.

Combining the linearized terms we obtain

$$\left[I - W + \delta_\xi A_i + \delta_\eta B_j + \delta_\zeta C_k\right]\Delta Q_{ijk} = -\Delta t\left[\frac{\partial Q}{\partial t} + \frac{\partial E}{\partial \xi} + \frac{\partial F}{\partial \eta} + \frac{\partial G}{\partial \zeta} - V_{\xi,\eta,\zeta} - D\right] \qquad (2.6.5)$$

Here the operator $\delta_\xi A_i$ is defined as

$$\left(\delta_\xi A_i\right)\Delta Q_{ijk} = A_{i+1/2}^R\Delta Q_{i+1,jk} + \left\{A_{i+1/2}^L - A_{i-1/2}^R\right\}\Delta Q_{ijk} - A_{i-1/2}^L\Delta Q_{i-1,jk} \qquad (2.6.6)$$

while the corresponding operators $\delta_\eta B_j$ and $\delta_\zeta C_k$ are defined as

17

$$\left(\delta_\eta B_j\right)\Delta Q_{ijk} = B^R_{j+1/2}\Delta Q_{i,j+1,k} + \left\{B^L_{j+1/2} - B^R_{j-1/2}\right\}\Delta Q_{ijk} - B^L_{j-1/2}\Delta Q_{i,j-1,k}$$

$$\left(\delta_\zeta C_k\right)\Delta Q_{ijk} = C^R_{k+1/2}\Delta Q_{i,j,k+1} + \left\{C^L_{k+1/2} - C^R_{k-1/2}\right\}\Delta Q_{ijk} - C^L_{k-1/2}\Delta Q_{i,j,k-1}$$

(2.6.7)

As Eq. (2.6.5) indicates, the block matrix on the left hand side is a septadiagonal (since we are formulating for the 3D equation system). To invert this large matrix in a cost effective manner, we employ the ADI procedure.

The ADI operator inverts the large septadiagonal matrix (or pentadiagonal matrix in a 2D case) by splitting the operator as a product of three independent sweeps in the ξ, η, and ζ directions. The ADI approximation for the implicit matrix is given as

$$\left[I + \delta_\xi A_i - W\right]\left[I - W\right]^{-1}\left[I + \delta_\eta B_j - W\right]\left[I - W\right]^{-1}\left[I + \delta_\zeta C_k - W\right]\Delta Q$$

$$= -\left[\frac{\partial E}{\partial \xi} + \frac{\partial F}{\partial \eta} + \frac{\partial G}{\partial \zeta} - V_{\xi,\eta,\zeta} - D\right]\Delta t$$

(2.6.8)

We note that the operator in each sweep is now only a tridiagonal matrix which can be inverted efficiently using the Thomas algorithm. Furthermore, while the ADI operator introduces an error into the solution from the approximations it entails, this error can be reduced by performing iterations at each time step and converging to a time-accurate solution [51].

2.7   TURBULENCE MODELING: kε AND LES

Turbulent flows are characterized by the existence of spatially and temporally fluctuating fields with a wide range of length and time scales. Depending on how the various length and time scales are resolved, three approaches are currently used in the numerical simulation of turbulent flows: the time-averaged or Reynolds-Averaged (RANS) approach, the Direct Numerical Simulation (DNS) approach, and the Large Eddy Simulation (LES) approach. In the RANS approach, the ensemble-averaged Navier-Stokes equations are solved along with turbulence closure models for the Reynolds-stresses. The RANS turbulence models are calibrated using experimental observations and often incorporate heuristic corrections. RANS is the approach utilized for simulating most steady or slowly varying flows. The large scale features of flowfields differ considerably from one flow to

18

another, e.g., ducted flows, aerodynamic flows, jet/wake flows, stratified flows, etc., all have significantly different flow structures. RANS models use a single scale equation to represent a broad range of turbulent length scales. The invariance of modeling coefficients cannot be made very general for differing flows with any reliability. For flows with rapid temporal variations such at ETC, use of RANS time-averaged assumptions are very questionable.

In DNS, the non-averaged/time-dependent Navier-Stokes equations are solved with resolution of all temporal and spatial scales of the flow required eliminating the need for turbulence modeling. The results from the DNS approach are very accurate and reveal valuable information on the turbulence structures. Since the direct numerical simulations resolve all length scales, the computational demands are very large (requiring hundreds of hours of CPU time on super computers). Also, because of the scaling of CPU time and memory with powers of Reynolds number, direction numerical simulations are limited to analyzing low Reynolds number flows.

A compromise to the DNS approach is the technique of Large Eddy Simulations (LES) in which the large scales of turbulence are directly simulated while the small (inner) scales(subgrid scales or SGS) are modeled. The large scales represent the anisotropic part of the energy spectrum and contain most of the energy. The small scales are more isotropic in nature and relatively independent from the resolved part of the spectrum (grid scales). The results from the LES can be quite accurate because the only approximation involved is the modeling of the SGS terms which do not contain much energy. LES has the advantage of reduced empiricism over the RANS approach and is applicable to flows with rapid temporal variations. It does not require the fine grids entailed in DNS simulation and is thus applicable to higher Reynolds number flows.

2.7.1 $k\varepsilon$ Model

A popular turbulence model in the RANS framework is the two-equation $k\varepsilon$ model in which partial differential equations are solved for the transport of turbulent kinetic energy (k) and turbulent dissipation (ε), and the eddy viscosity is related to these two quantities. The basic high Reynolds number form of the $k\varepsilon$ equations [Launder et al., 1972] (Ref. 52) is given by:

$$\rho \frac{Dk}{Dt} \quad = \quad \frac{\partial}{\partial x_i}\left(\frac{\mu_t}{\sigma_k}\frac{\partial k}{\partial x_i}\right) \quad + \quad P \quad - \quad \rho\varepsilon$$

[Convection] [Diffusion] [Production] [Dissipation] **(2.7.1.1)**

$$\rho \frac{D\varepsilon}{Dt} \quad = \quad \frac{\partial}{\partial x_i}\left(\frac{\mu_t}{\sigma_\varepsilon}\frac{\partial \varepsilon}{\partial x_i}\right) \quad + \quad C_1\left(\frac{\varepsilon}{k}\right)P \quad - \quad C_2\left(\frac{\varepsilon}{k}\right)\rho\varepsilon$$

where the turbulent production, P, is given by:

$$P = -\rho\overline{u_i u_j}\frac{\partial U_i}{\partial x_j} \qquad (2.7.1.2)$$

and the turbulent stress, $\rho\overline{u_i u_j}$, is evaluated using the eddy viscosity assumption:

$$-\rho\overline{u_i u_j}\frac{\partial U_i}{\partial x_j} = \mu_t\left(\frac{\partial U_i}{\partial x_j}+\frac{\partial U_j}{\partial x_i}\right) - \frac{2}{3}\rho k\delta_{ij} \qquad (2.7.1.3)$$

The turbulent viscosity, μ_t, is defined by:

$$\mu_t = C_\mu\rho\frac{k^2}{\varepsilon} \qquad (2.7.1.4)$$

and the "standard" coefficients are as follows:

$$C_\mu = .09, \quad C_i = 1.45, \quad C_2 = 1.9, \quad \sigma_k = 1.0, \quad \sigma_\varepsilon = 1.3$$

The presence of solid boundaries affects turbulence characteristics in the near vicinity of the wall. The basic high Reynolds form of the kε equation has to be modified in order to extend its applicability to the wall. This involves the addition of "low Reynolds number" terms to the equations whose influence is strongest close to the wall and diminishes away from the wall. In the CRAFT code, the low Reynolds number variant of Chien [53] has been incorporated. In this model, the source terms are modified as:

$$k \text{ eqn:} \quad P - \rho\varepsilon - \frac{2\mu_t k}{L^2} \qquad (2.7.1.5)$$

ϵ eqn:

$$\frac{\epsilon}{k}\left[C_1 P - C_2 F \rho \epsilon - \frac{2\mu_t k e^{\left(-C_4 y^+\right)}}{L^2}\right] \qquad \textbf{(2.7.1.6)}$$

where

$$F = 1 - \frac{2}{9} e^{\left(-\rho k^2 / 6\mu\epsilon\right)^3} \qquad \textbf{(2.7.1.7)}$$

$$\mu_t = C_\mu \rho \frac{k^2}{\epsilon}\left[1 - \exp\left(C_3 y^+\right)\right] \qquad \textbf{(2.7.1.8)}$$

and the coefficients are now given by:

$$C_1 = 1.35, \quad C_2 = 1.8, \quad C_3 = .0115, \quad C_4 = 0.5, \quad C_\mu = 0.09$$

Here L is the distance from the closest wall and μ is the laminar viscosity. The $k\epsilon$ equations are solved in a coupled manner with the rest of the equations (k and $k\epsilon$ are added to the Q array and matrix sizes are expanded). The $k\epsilon$ model in CRAFT has been used primarily for steady or slowly changing flow calculations.

2.7.2 Large Eddy Simulation (LES)

For high Reynolds number flows of practical interest, direct numerical simulation resolving all spatial and temporal scales is not feasible and the turbulence must be modeled. Conventional time-averaged Reynolds-stress (RS) modeling for unsteady flows requires that turbulent time-scales are small in comparison to convective time scales. Such averaging may be adequate for slowly accelerating flows or flows with low frequency periodic behavior. It is not generally adequate for short-duration transient flows and flows with higher frequency periodic behavior. For such flows, the time scales of the large scale turbulent structure and the convective processes are comparable. A large-eddy simulation (LES) procedure provides a workable method for transient flows whereby the large scale turbulent structure is directly simulated by the flow solver and the finer scale, dissipative structure (which cannot be resolved numerically with practical grids) is modeled. The modeling involves a spatial filtering process which involves subgrid stress (SGS) terms as will be discussed below. Table VI summarizes the basic distinctions between RANS and LES modeling approaches.

Table VI. RANS and LES Modeling Distinctions

LES vs RANS OVERVIEW / INCOMPRESSIBLE

1. DECOMPOSITION

○ **LES** $u = \tilde{u} + u''$

$\tilde{u}$ – *resolveable* $\tilde{u} = \tilde{u}(t)$

u'' – *nonresolveable* $u'' = u''(t)$

○ **RANS** $u = \bar{u} + u'$

$\bar{u}$ – *mean* $\bar{u} \neq \bar{u}(t)$

u' – *fluctuating* $u'' = u''(t)$

2. AVERAGING

○ **LES** → SPATIAL FILTER TO ELIMINATE HIGH FREQUENCY COMPONENTS

○ **RANS** → TIME-AVERAGING, INTERVAL MUST BE <u>LARGER</u> THAN CONVECTIVE MOTION OF LARGE SCALE STRUCTURE; NOT APPLICABLE FOR SHORT-DURATION FLOWS

3. TERMS FROM AVERAGING

○ **LES** $\overline{u_i'' u_j''} + \left(\overline{\bar{u}_i \bar{u}_j} - \bar{u}_i \bar{u}_j \right) + \left(\overline{\bar{u}_i u_j''} + \overline{u_i'' \bar{u}_j} \right)$ →   INVARIANT?

○ **RANS** $\overline{u_i' u_j'}$ →   NOT INVARIANT, COEFFICIENTS ARE PROBLEM-DEPENDENT

Reliable SGS models for non-homogeneous turbulent compressible flows are still in the developmental stage [54,55]. Issues such as the backscatter of turbulent kinetic energy from small scales to the large scales, etc., need further investigation especially when high Reynolds number flows are simulated with moderate resolution. In studies described in this report, a simple subgrid model which is a compressible extension of the Smagorinsky model [56] is used where the effect of subgrid scales is assumed to be only dissipative.

The simulation of turbulence using LES methodology begins with the filtering of the small scale effects from the large scale motion in the full Navier-Stokes equations. The filtering for Favré-averaged variables is given as

$$\tilde{\phi} = \frac{\overline{\rho \phi}}{\bar{\rho}} = \frac{1}{\bar{\rho}} \iiint \rho \phi \left[\prod_{i=1}^{3} G_i \left(X_i - X_i', \Delta_i \right) \right] dv' \qquad (2.7.2.1)$$

22

Here, $G_i\left(X_i - X_i', \Delta_i\right)$ is the filter function and is linked to the filter width, Δ_i. The time varying variable ϕ is now expressed as

$$\phi = \tilde{\phi} + \phi'$$ (2.7.2.2)

where $\tilde{\phi}$ is the Favré-averaged large scale component of ϕ, and ϕ', is the small scale component.

Applying the filtering described above, the Navier-Stokes equations are expressed as

$$\frac{\partial \overline{\rho}}{\partial t} + \frac{\partial}{\partial x_i}\left(\overline{\rho}\tilde{u}_i\right) = 0 \ \{Mass\}$$

$$\frac{\partial}{\partial t}\left(\overline{\rho}\tilde{u}_i\right) + \frac{\partial}{\partial x_j}\left[\left(\overline{\rho}\tilde{u}_i\tilde{u}_j\right) + \overline{P}\delta_{ij} - \overline{\tau}_{ij}\right] + \frac{\partial}{\partial x_j}\tau_{ij}^{SGS} = 0 \ \{Momentum\}$$ (2.7.2.3)

$$\frac{\partial}{\partial t}\left(\overline{\rho}\tilde{E}\right) + \frac{\partial}{\partial x_i}\left[\left(\overline{\rho}\tilde{E} + \overline{P}\right)\tilde{u}_i - \left(\tilde{u}_j\overline{\tau}_{ij} - \overline{q}_i\right)\right] + \frac{\partial}{\partial x_i}\left[E_i^{SGS} + P_i^{SGS} - \sigma_i^{SGS}\right] = 0 \ \{Energy\}$$

$$\overline{P} = \overline{\rho}R\tilde{T}$$

The terms superscripted SGS denote the small scale terms which have to be modelled.

The SGS terms in the momentum equation, when expanded, can be viewed as a sum of three terms: Leonard Stress, Cross Stress, and Reynolds Subgrid Stress as given below

$$\tau_{ij}^{SGS} = \overline{\rho}\left(\widetilde{u_i u_j} - \tilde{u}_i\tilde{u}_j\right)$$

$$= \overline{\rho}\left[\widetilde{\tilde{u}_i\tilde{u}_j} - \tilde{u}_i\tilde{u}_j\right] + \overline{\rho}\left[\widetilde{\tilde{u}_i u_j'} + \widetilde{\tilde{u}_j u_i'}\right] + \overline{\rho}\left(\widetilde{u_i' u_j'}\right)$$ (2.7.2.4)

$$= L_{ij} + C_{ij} + R_{ij}$$

Here, L, C, and R, are the Leonard, Cross (forward scattering) and Reynolds subgrid (backward scattering) terms, respectively. These three terms are modeled using a simplified compressible generalization of the Smagorinsky model [56] which assumes that the subgrid scale turbulence kinetic energy is smaller than the thermodynamic pressure. The simplification yields

23

$$\tau_{ij}^{SGS} = -2\bar{\rho}\nu_T\left(S_{ij} - \frac{1}{3}S_{kk}\delta_{ij}\right) \qquad (2.7.2.5)$$

where S_{ij} is the strain tensor of the Favré-averaged large scale component, given by

$$S_{ij} = \frac{1}{2}\left[\frac{\partial \tilde{u}_i}{\partial x_j} + \frac{\partial \tilde{u}_j}{\partial x_i}\right] \qquad (2.7.2.6)$$

and the subgrid eddy viscosity is given by

$$\nu_T = C_R\Delta^2\left|S_{ij}S_{ij}\right|^{1/2} \qquad (2.7.2.7)$$

Here, Δ is the effective filter width, given by

$$\Delta = \left(\Delta_x\Delta_y\Delta_z\right)^{1/3} \qquad (2.7.2.8)$$

$\Delta_x, \Delta_y, \Delta_z$ are the filter widths in the x, y, and z directions.

In our use of CRAFT, the filter widths are approximated by the respective grid spacings. A value of 0.02 is used for C_R. The subgrid terms in the energy equation are given by

$$E_i^{SGS} = \bar{\rho}\left(\widetilde{Eu_i} - \tilde{E}\tilde{u}_i\right)$$

$$P_i^{SGS} = \left(\widetilde{pu_i} - \bar{p}\tilde{u}_i\right) \qquad (2.7.2.9)$$

$$\sigma_i^{SGS} = \left(\widetilde{u_i\tau_{ji}} - \tilde{u}_i\tilde{\tau}_{ji}\right)$$

The SGS terms in the energy equation are modeled using scale similarity yielding

$$E_i^{SGS} + P_i^{SGS} - \sigma_i^{SGS} = -\bar{\rho}\left\{\frac{\nu_T}{Pr_T}\frac{\partial \tilde{h}}{\partial x_i}\right\} - \tilde{u}\tau_{ji}^{SGS} \qquad (2.7.2.10)$$

where the subgrid kinetic energy is neglected when accounting for the fluctuations of the total energy.

2 4

By definition, filtering is implicit in any numerical simulation using a finite number of grid points because length scales smaller than the grid size cannot be resolved. This implicit filtering is called a top-hat or box filter in finite-difference representation and a sharp cut-off filter in a spectral (Fourier) representation. In addition to the implicit filtering, an explicit filter can also be applied, such as the popular Gaussian filter, with filter widths different from the local grid spacing. This explicit filtering is usually referred to as "prefiltering" and the argument in its favor is that since the length scale used in the SGS model is decided by the filter width, it would be prudent to make the SGS model independent of the numerical resolution by applying a prefilter.

2.8   SPECIALIZED GRID FEATURES

In this section we highlight upgrades to the grid methodology in CRAFT which enhances its capabilities for geometrically complex, dynamic volume, interior ballistic flowfields. The three primary upgrades are as follows:

  a) Dynamic Grids
  b) Grid Blanking
  c) Grid Embedding

In the following paragraphs, we will briefly describe the salient features of each of these three upgrades.

2.8.1 Dynamic Grids

Dynamic grid techniques allow for the motion and expansion of the cell volume as the flow domain changes in time. The grid movement is coupled to the flow solution and the additional fluxes as well as the volumetric effects generated from the movement of the grid are incorporated into the numerical procedure. Our methodology in CRAFT closely follows the formulation of Vinokur (Ref. 57) and we refer the reader to his report for details.

The modified form of the integral conservation equations for a time-varying grid are given as

$$\int_{t_2} Q dV - \int_{t_1} Q dV + \int_{t_1}^{t_2} \int_{S(t)} \bar{n} \bullet \bar{F} dS = \int_{t_1}^{t_2} \int_{V(t)} D dV \qquad \textbf{(2.8.1.1)}$$

25

We note that in comparison with Eq. (2.2.1), Equation (2.8.1.1) reveals an additional integral in time since the cell volumes and areas are changing. The discretized form of Eq. (2.8.1.1) after taking the additional time integral into account is written as follows (Ref. 57):

$$
\overbrace{\left(\frac{Q^{n+1}}{\Delta t}\right)V^{n+1} + Q^n\left(\frac{V^{n+1} - V^n}{\Delta t}\right)}^{\text{TERM } I} + \overbrace{\left[\frac{E_{i+1/2} - E_{i-1/2}}{\Delta \xi} + \frac{F_{j+1/2} - F_{j-1/2}}{\Delta \eta} + \frac{G_{k+1/2} - G_{k-1/2}}{\Delta \zeta}\right]}^{\text{TERM } II} \qquad (2.8.1.2)
$$

$$
= \overbrace{D^{n+1}V^n}^{\text{TERM } III}
$$

The modifications arising from the dynamic grid movement are classified into three sets of terms. Term I generates a volumetric source term for the conserved variables. This term ensures that provided there is no net flux or combustion, the change in volume proportionally alters the mass and energy per unit volume. Term II contains the changes to the flux vectors (E, F, and G) which now have to account for additional flux being generated by the movement of each face of the generalized finite-volume cell. For instance, the flux vectors E and F are written as

$$
E = \begin{bmatrix} \rho(U - U_r) \\ \rho u U + \bar{\ell}_x P - \rho u U_r \\ \rho v U + \bar{\ell}_y P - \rho v U_r \\ \rho w U + \bar{\ell}_z P - \rho w U_r \\ (e + P)U - e U_r \\ \rho_i(U - U_r) \\ \vdots \\ \rho_{n-1}(U - U_r) \end{bmatrix}; \qquad
F = \begin{bmatrix} \rho(V - V_r) \\ \rho u V + \bar{m}_x P - \rho u V_r \\ \rho v V + \bar{m}_y P - \rho v V_r \\ \rho w V + \bar{m}_z P - \rho w V_r \\ (e + P)V - e V_r \\ \rho_i(V - V_r) \\ \vdots \\ \rho_{n-1}(V - V_r) \end{bmatrix} \qquad (2.8.1.3)
$$

Here U_r is the additional volumetric flux generated by the movement of the ξ face, while V_r is the corresponding movement of the η face. These additional fluxes due to face movement are computed using the following relationship:

$$
U_r = \frac{\delta V_\xi}{\Delta t} \qquad (2.8.1.4)
$$

26

Here δV_ξ is the volume swept by the ξ face over the period of the time step. Similar relationships are also defined for the η and ζ faces as well. The metrics that are used to evaluate the flux vectors ($\bar{l}_x, \bar{l}_y, \bar{l}_z$, etc.) are the average surface area of the cell over the time step. Finally, Term III contains the volumetric changes to the source terms.

To evaluate the upwind flux terms ($E_{i+1/2}$) at the cell interfaces, we recompute the eigenvalues of the modified flux vectors. The new eigenvalues are derived to be

$$\Lambda = DIAG.(U' + C, U' - C, U', \ldots U') \qquad (2.8.1.5)$$

where

$$U' = U - U_r \qquad (2.8.1.6)$$

Hence by modifying the definition of the volume flux through each face, the upwind flux relationships derived in Section 2.5 may be used unchanged. The dynamic grid formulation described above has been tested extensively to ensure that the code's conservation capabilities do not deteriorate when strong grid movement and distortion are present.

2.8.2 Grid Blanking

Grid blanking increases the versatility of the CRAFT code for problems involving complex geometries. The grid blanking feature in CRAFT has been adapted from the PARC code [58] and works in conjunction with the ADI procedure to invert the matrix arrays in the implicit sweep. Grid blanking is achieved by using a patching algorithm which logically decomposes a grid containing internal boundaries into a family of patches. In addition to simplifying gridding issues, grid blanking also permits a very generalized boundary specification procedure since each boundary plane can now be broken up into segments having different boundary conditions.

The grid blanking feature in CRAFT is illustrated by a computation of the venting/muzzle blast from a gun barrel (see Figure 2.8.2.1). One end of the gun barrel is shut while the other end is opened to the atmosphere at t=0. The transient flow inside the barrel, and the external plume are computed concurrently using grid blanking. The single rectangular grid implemented for the problem is shown in Figure 2.8.2.2. It is clear that
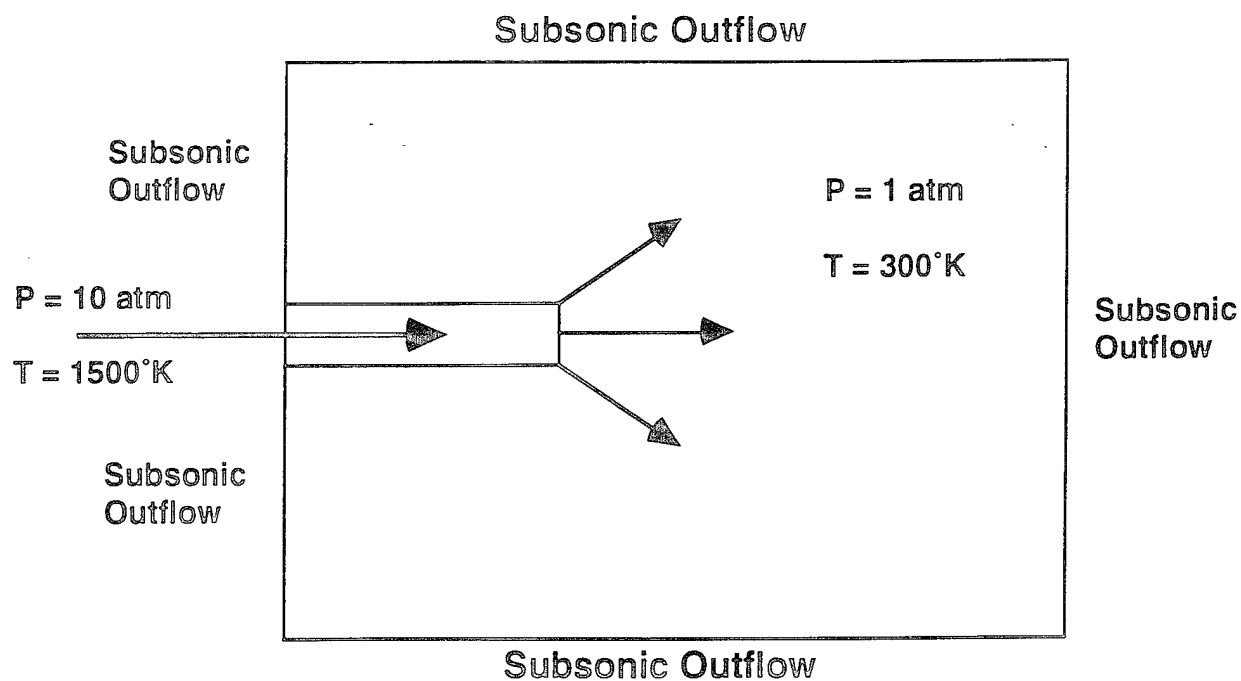
Fig. 2.8.2.1. Schematic of transient venting problem from a gun barrel.
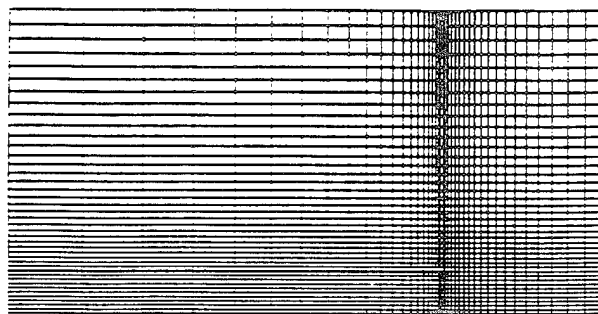
Fig. 2.8.2.2. Numerical grid for venting problem.

since the gun barrel lies in the interior of the grid, analyzing this problem requires the use of grid patching since two sets of boundary conditions are required – one for the interior surface of the barrel wall, and one for the exterior surface of the barrel wall which is exposed to the ambience. The grid patches used for this problem are shown in Figure 2.8.2.3.

28
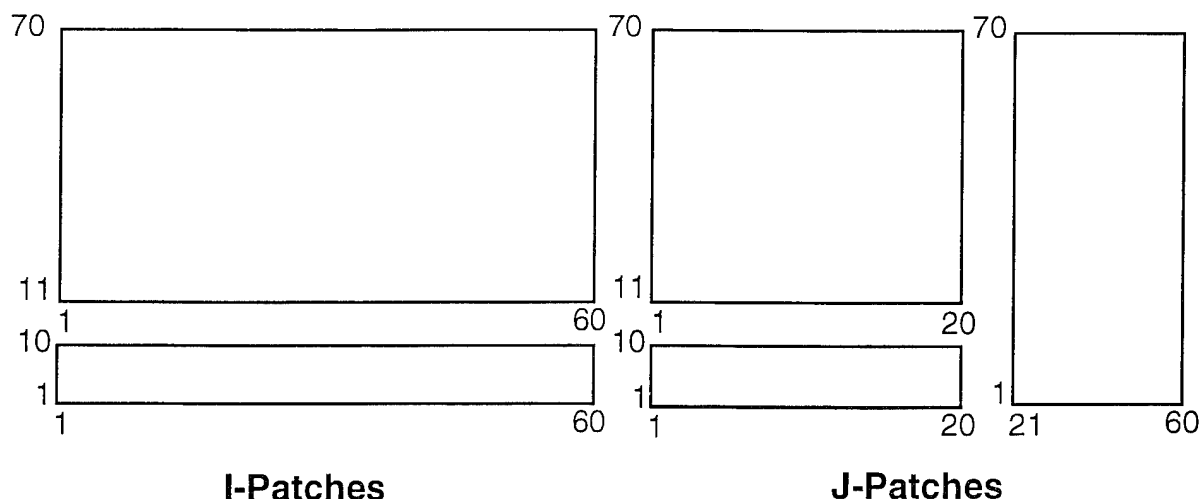
I-Patches   **J-Patches**

Fig. 2.8.2.3. Grid patches generated for flux and boundary condition calculations.

In Figure 2.8.2.4, we track the exhaust from the gun barrel by plotting the stagnation enthalpy contours at 1, 2, and 3 ms respectively. The initial condition of the gas in the barrel has a pressure and temperature ratio 10 times that of the respective ambient conditions outside. At 1 ms, the high pressure gas in the barrel sends an underexpanded plume out creating a blast wave. By 2 ms, the plume expands further out thereby reducing the pressure within the barrel since there is only a finite amount of gas within the barrel. By 3 ms, the gas within the barrel overexpands below the pressure of the plume outside. The higher back pressure sends a compression back into the barrel and flow reversal occurs which is clearly seen in the stagnation enthalpy contours. In problems with finite-thickness solid volumes, grid points within the volume are blanked out. In our recent work on the ram accelerators [27,28] a coupled 3D transient conduction capability has been added so that the transient wall temperature can be calculated as part of the basic computational procedure. The solid grid points blanked out now serve to solve the conduction equation.

2.8.3 Grid Embedding

The grid embedding feature is necessary for unsteady flows where the flow domain is changing substantially in volume as in interior ballistic problems. This feature is used in conjunction with the dynamic movement of the grid. If a grid cell expands and becomes larger than a user-specified

29
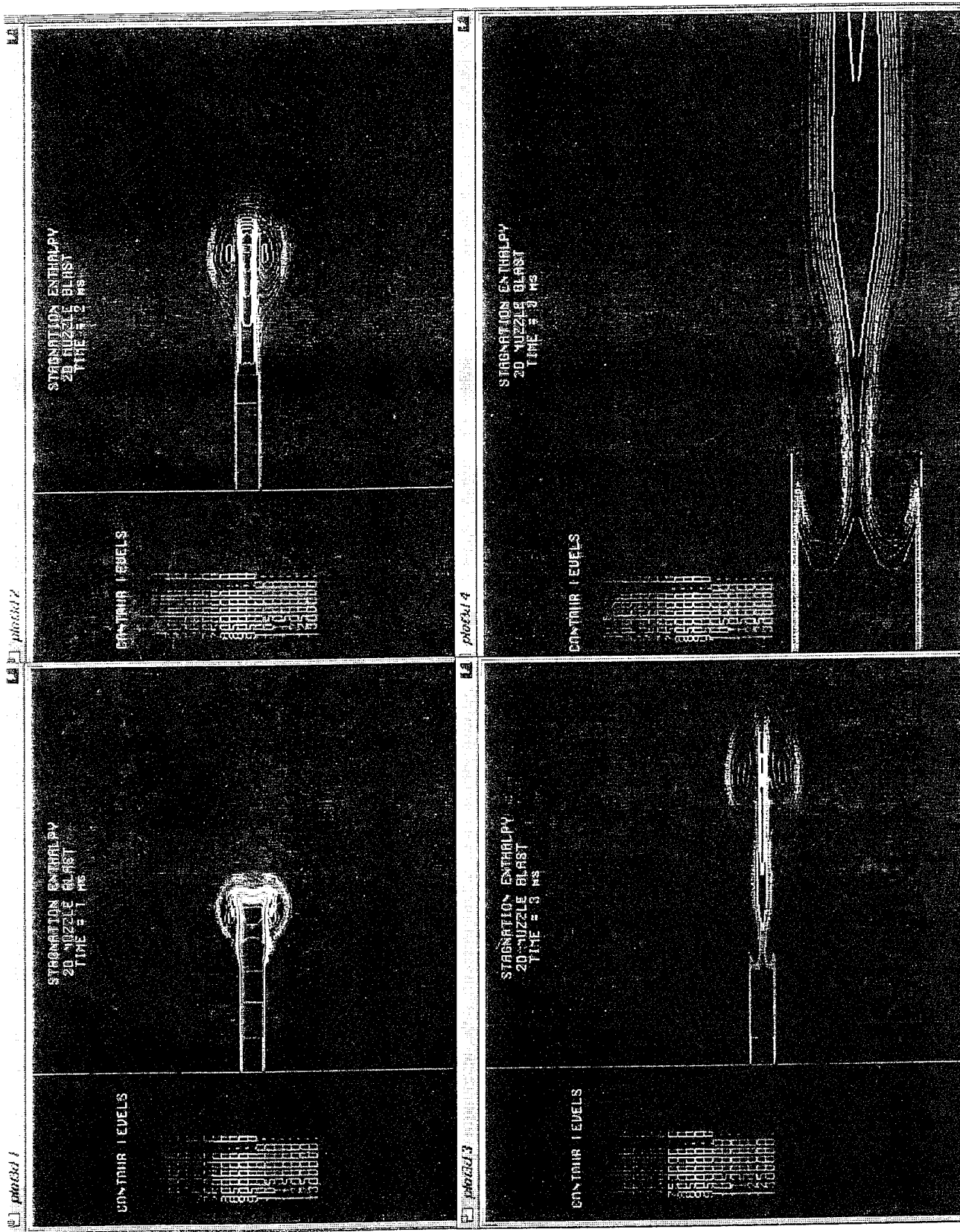
Fig. 2.8.2.4. Stagnation enthalpy contours plotted at three time levels during venting of the plume.

limit, it is subdivided into smaller cells. This ensures that as the domain of interest increases, the grid continues to resolve spatial gradients accurately. The flow properties in the divided cell are obtained by interpolating from the original coarser grid each time a division occurs. To illustrate this feature, we plot the initial grid in a ballistic chamber in Figure 2.8.3.1a. In Figure 2.8.3.1b, we plot the corresponding grid in the chamber later in the ballistic cycle at which point the domain has expanded considerably. As is apparent even though the spatial domain shows a three fold increase, the ability to capture discontinuities or to resolve wave motion is unimpaired because the grid embedding procedure has added an adequate number of grid points to maintain the original spatial accuracy.

(a).

(b).
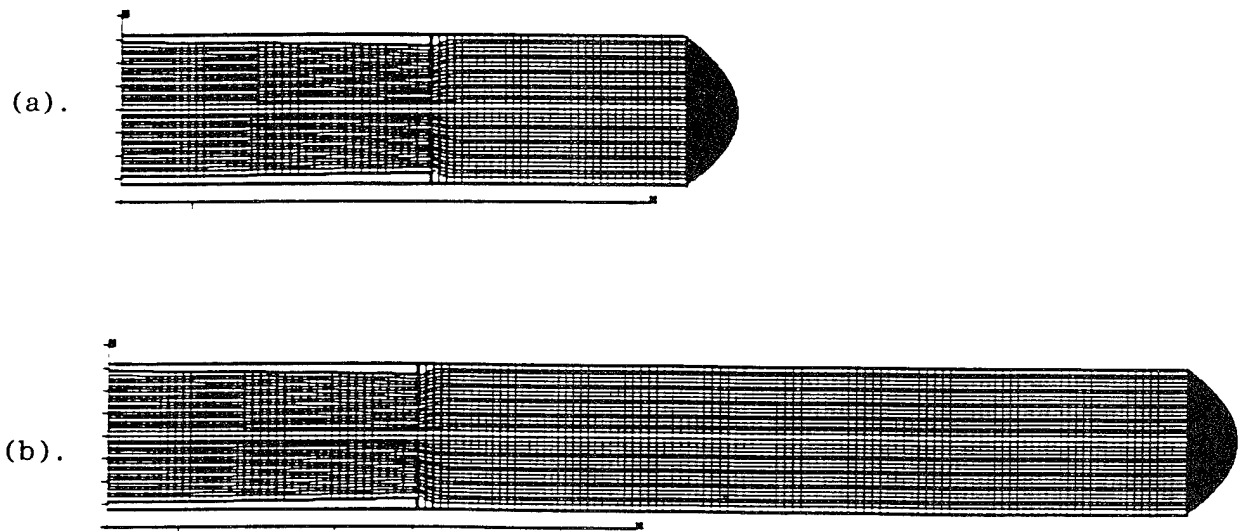
Fig. 2.8.3.1. Grid inside gun barrel at two time levels exhibiting grid embedding procedure.

2.9 BOUNDARY CONDITIONS

In this section, we discuss the boundary condition procedures in CRAFT that are applied in a manner consistent with the finite volume formulation. We focus attention here on inviscid flow conditions since viscous boundary layers were generally not resolved in our ETC gun simulations. However, generalized viscous wall conditions are operational in CRAFT and we refer the reader to our ram accelerator publications [28], where we describe the analysis of wall viscous effects for transient flows.

31

The inviscid boundary condition methodology is based on the method of characteristics. In this procedure, we determine the number of waves entering the flow domain from the outside at each boundary and apply boundary conditions to account for the information they convect in. For the remainder of the waves which reach the boundary from within the flowfield, the information is computed from the equations of motion. The direction of propagation for each wave is determined from its eigenvalue i.e. a positive eigenvalue denotes a wave traveling in the positive direction and vice versa.

The classes of inviscid boundary conditions that are of interest in ETC interior ballistic flow problems include subsonic/supersonic inflows and wall reflection/centerline conditions. The boundary condition for supersonic inflows is straightforward since all the eigenvalues are positive and hence all the characteristics (or waves) are entering the boundary from outside the flow domain. Therefore, all flow variables are specified as boundary conditions and the flux at the boundary face is completely defined. Subsonic inflow boundary conditions are more involved, since one eigenvalue (U − C) is negative while the remaining four (U+C, U, U, U) are positive. Hence four boundary conditions are specified. Typically the following four conditions are applied for steady inflows:

(1)   Total Enthalpy (H_T)

(2)   Total Pressure (P_T)

(3,4) Cross-flow angularity (V/U and W/U) which is not typically obtainable and assumed to be zero in the plane parallel to the in-flow boundary condition (V, W) which ensures that the inflow is perpendicular to the boundary plane.

The fifth condition which corresponds to the negative characteristic is obtained by extrapolating the characteristic variable corresponding to this wave. This is accomplished through the solution of the following equation between the boundary and the interior point:

$$\ell_2 \left[\frac{\partial Q}{\partial t} + \frac{\partial E}{\partial \xi} \right] = 0 \qquad\qquad (2.9.1)$$

Here ℓ_2 is the row of the left eigenvector matrix L which corresponds to the (U − C) eigenvalue. The boundary conditions result in five nonlinear

32

equations which are solved in a coupled matrix form via a Newton-Raphson iterative procedure to obtain the flow quantities.

For unsteady applications, the two conditions on P_T and H_T are not utilized since these are appropriate only at steady state. These two conditions are replaced with

$$L_1 \frac{\partial Q}{\partial t} = 0, \quad L_5 \frac{\partial Q}{\partial t} = 0 \qquad (2.9.2)$$

Equation(2.9.2) allows for waves to pass through the inflow and provides a non-reflective boundary condition.

Inviscid wall boundary as well as centerline symmetry conditions are handled by generating fictitious cells outside of the computational domain so the cell interface flux that coincides with the wall or the symmetry plane can be handled as if it were an interior plane. The flow variables of the cells inside the domain are reflected about the symmetry plane to produce a mirror cell on the other side. The scalar flow variables in the reflected cell (e.g. density and energy) are identical to the interior cell values and are given by

$$\begin{aligned} \rho^r &= \rho \\ e^r &= e \\ \rho_s^{\ r} &= \rho_s \quad (s = 1, 2, ..., n-1) \end{aligned} \qquad (2.9.3)$$

On the other hand, the gas velocities in the two cells are mirror images to ensure that the net normal mass flux through the boundary is zero although there still is a pressure flux. The velocities in the reflected cell are given by

$$\begin{aligned} u^r &= u - 2\ell_x \left(\ell_x u + \ell_y v + \ell_z w \right) \\ v^r &= v - 2\ell_y \left(\ell_x u + \ell_y v + \ell_z w \right) \\ w^r &= w - 2\ell_z \left(\ell_x u + \ell_y v + \ell_z w \right) \end{aligned} \qquad (2.9.4)$$

The unit metrics in the above expressions are those of the boundary cell under consideration. This transformation preserves the magnitude of the velocity while reorienting its direction.

33

2.10 SELECTED FUNDAMENTAL STUDIES

In this section, we describe several fundamental studies which demonstrate the ability of the CRAFT code to accurately analyze problems involving finite-rate combustion, turbulence with large scale vortical structures, and, transient wave processes in interior ballistic chambers. We begin by describing some very basic studies for shock tubes with high pressure ratios to emphasize the ability of CRAFT to capture strong shocks without spurious oscillations. In the next subsection, we describe fundamental combustion studies in premixed hydrogen-air mixtures where we focus on the need to accurately resolve the spatial structure. This is followed by simulations of classical shear layer experiments with large density gradients where large scale turbulent vortical structures were first identified experimentally. Finally, we discuss some preliminary simulations of ETC like configurations where high pressure gas is injected into a gun chamber and the resulting wave processes are tracked.

2.10.1 Shock Tube Studies

The ability of CRAFT to simulate unsteady flowfield phenomena is assessed by computing one-dimensional solutions for a shock tube sealed at both ends. A shock tube 10 units in length was selected with a diaphragm located midway, separating the high-pressure chamber on the left from the low-pressure chamber on the right. Initial studies were conducted for a pressure ratio of 10 across the diaphragm. Figure 2.10.1.1 shows a time history of the pressure distribution along the shock tube. Figure 2.10.1.2 shows a corresponding plot for a subsequent study conducted with an initial pressure ratio of 1000. In both cases, the code was found to operate very robustly with minimal numerical diffusion, and a shock pattern which did not attenuate with time. Further, it was found that the code operated very satisfactorily at large CFL numbers – a feature which is directly attributable to the implicit, strongly-coupled, higher-order, upwind numerical formulation of CRAFT.

2.10.2 Gas-Phase Combustion Studies

For applications (such as the Ram Accelerator), where the principal phenomena is premixed gas-phase combustion, the accuracy of the numerical simulation hinges on the code's ability to capture flame fronts as well as
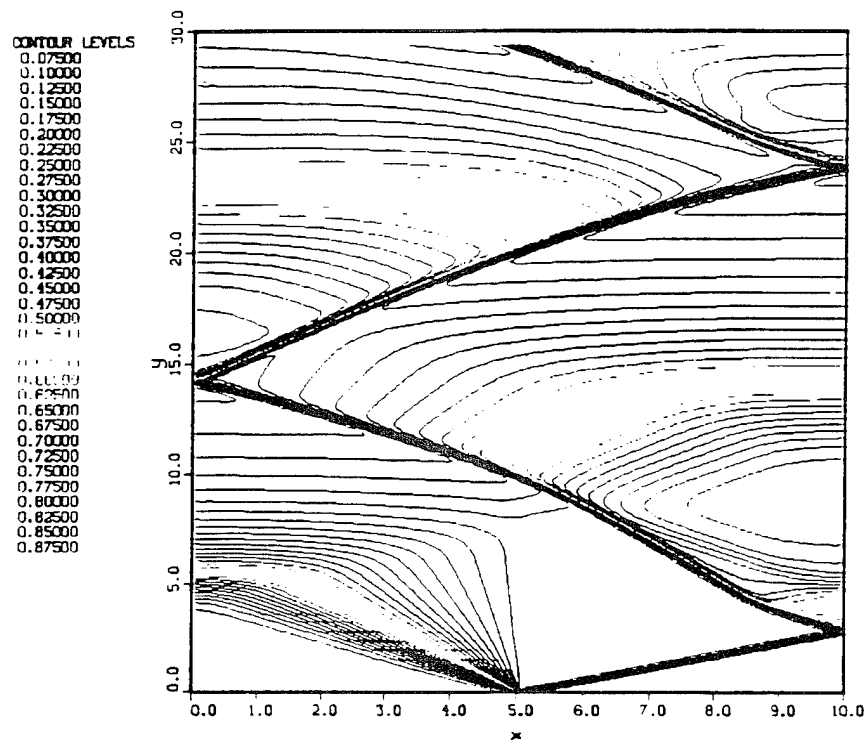
Fig. 2.10.1.1. Pressure variation with time for 10:1 shock tube.
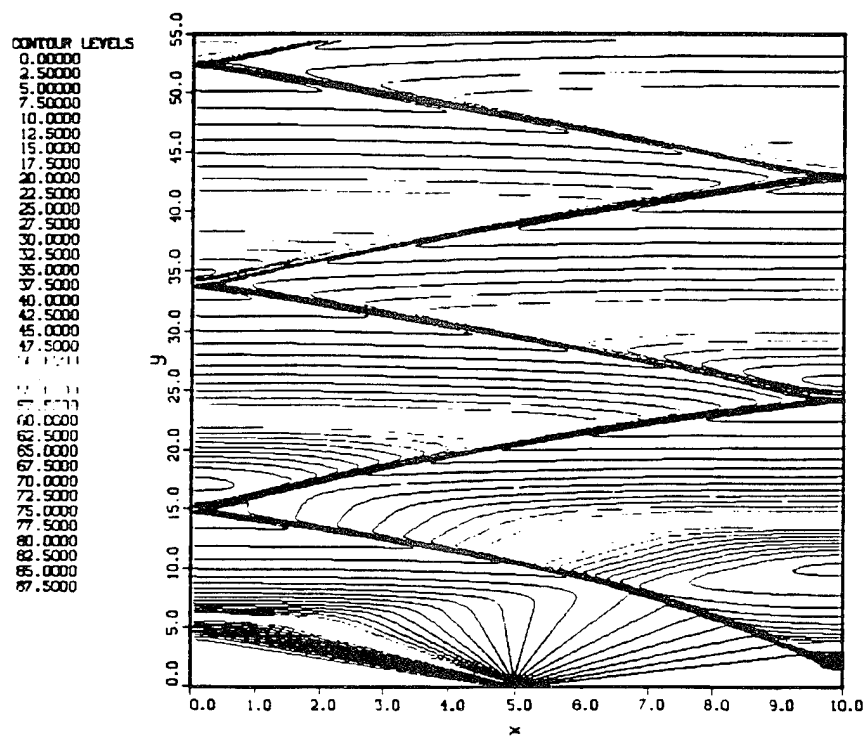
Fig. 2.10.1.2. Pressure variation with time for 1000:1 shock tube.

3 5

shock waves. We have performed some fundamental combustion studies to evaluate the ability of the CRAFT code to capture flame fronts in premixed combusting flows using as test cases, the shock induced combustion experiments of Lehr [59]. Two sets of calculations have been performed. The first for a steady combustion front and the second for an oscillating flame front. Recently, these cases have been numerically simulated by other authors [60,61] using different algorithms as well as different procedures for evaluating the chemistry. CRAFT utilizes strongly-coupled methodology with a "full" linearization of the chemical production term, $\dot{\omega}_i$, with respect to the Q array. Computing these test cases provides a rigorous evaluation of the ability of CRAFT to compute such flows.

The first test case simulated is for a steady shock-induced combustion front. The geometry is a 15mm diameter sphere-cylinder, moving at Mach 6.46 into a stoichiometric mixture of hydrogen and air. The premixed gas is at a pressure of 0.42 atm and a temperature of 292 K. The simulation was first performed on a relatively coarse, uniform grid of 71 x 71 as shown in Figure 2.10.2.1a. The reaction systems utilized are summarized in Table VII [62,63]. The computed density contours for the uniform grid are plotted

a. Uniform Grid   b. Density Contours
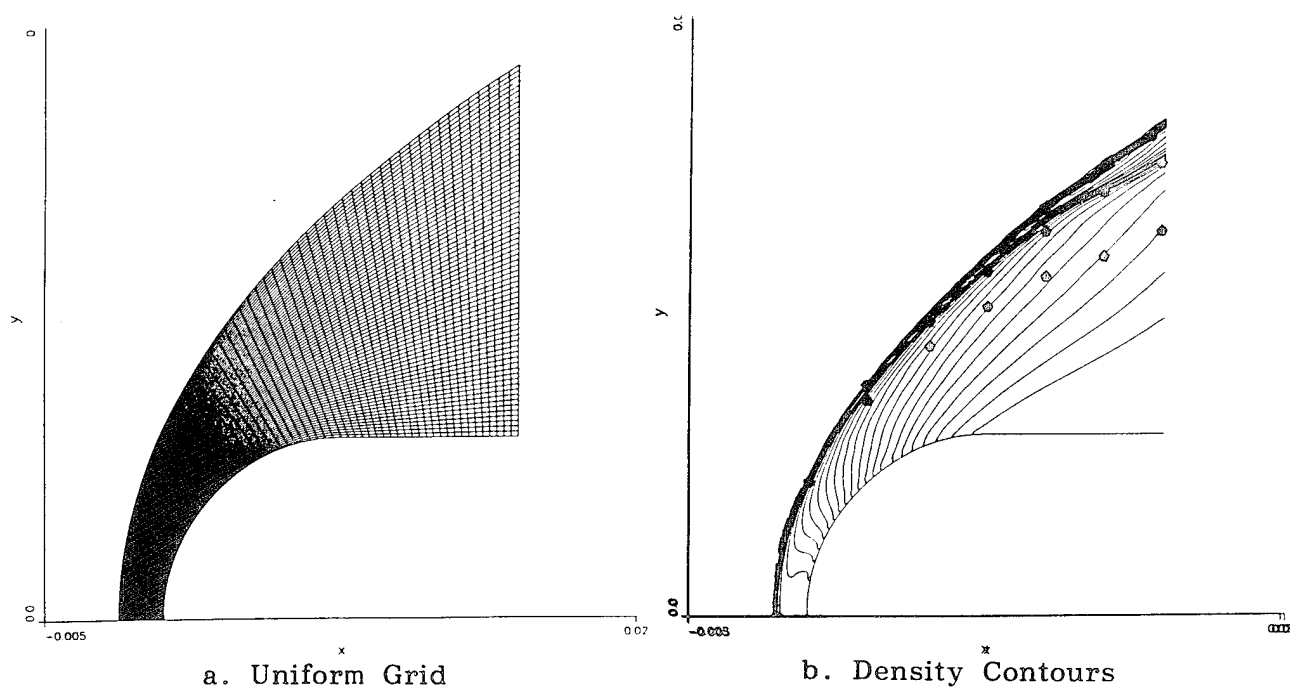
Fig. 2.10.2.1. Uniform numerical grid and computed density contours shown for steady shock-induced combustion.

plotted in Figure 2.10.2.1b while the experimental values for the shock and flame front are plotted as circles. As is evident from Figure 2.10.2.1b, with a uniform grid the numerical calculation underpredicts the induction zone significantly, away from the centerline. A similar observation has also been made by Sussman [61]. Both sets of reactions were found to produce comparable results.

Table VII. HYDROGEN/AIR RATES

$$k = AT^n \exp(-\Theta / T)$$

	Reactions			Jachimowski (1988)			Evans & Schexnayder (1979)		
				A	n	Θ	A	n	Θ
1.	$OH + H_2$	$\rightarrow$	$H + H_2O$	2.16×10^8	1.51	1726	2.0×10^{13}	0	2600
2.	$H + O_2$	$\rightarrow$	$O + OH$	1.91×10^{14}	0	8273	2.19×10^{14}	0	8455
3.	$O + H_2$	$\rightarrow$	$H + OH$	5.06×10^4	2.67	3166	7.5×10^{13}	0	5586
4.	$H + HO_2$	$\rightarrow$	$H_2 + O_2$	2.5×10^{13}	0	349	--	--	--
5.	$H + HO_2$	$\rightarrow$	$OH + OH$	1.5×10^{14}	0	505	--	--	--
6.	$O + HO_2$	$\rightarrow$	$OH + O_2$	2.0×10^{13}	0	0	--	--	--
7.	$OH + HO_2$	$\rightarrow$	$H_2O + O_2$	2.0×10^{13}	0	0	--	--	--
8.	$H + O_2 + M$	$\rightarrow$	$HO_2 + M$	8.0×10^{17}	-0.8	0	--	--	--
9.	$H + OH + M$	$\rightarrow$	$H_2O + M$	8.62×10^{21}	-2.0	0	4.39×10^{20}	-1.5	0
10.	$H + H + M$	$\rightarrow$	$H_2 + M$	7.3×10^{17}	-1.0	0	1.799×10^{18}	-1.0	0
11.	$H + O + M$	$\rightarrow$	$OH + M$	2.6×10^{16}	-0.6	0	7.1×10^{18}	-1.0	0
12.	$O + O + M$	$\rightarrow$	$O_2 + M$	1.14×10^{17}	-1.0	0	4.0×10^{17}	-1.0	0
13.	$OH + OH$	$\rightarrow$	$O + H_2O$	1.5×10^9	1.14	0	5.3×10^{12}	0	503
				8 SPECIES			7 SPECIES		
				13 REACTIONS			8 REACTIONS		

To improve upon the computed predictions without increasing the grid size, the uniform 71 x 71 grid was adapted using SAGE [64] employing density as the controlling variable. The final adapted grid is shown in Figure 2.10.2.2a and the computed results using this grid are shown in Figure 2.10.2.2b. The results for the adapted grid compare well with the experimental values – the induction zone spacing is captured accurately as it

a. Adapted Grid   b. Density Contours
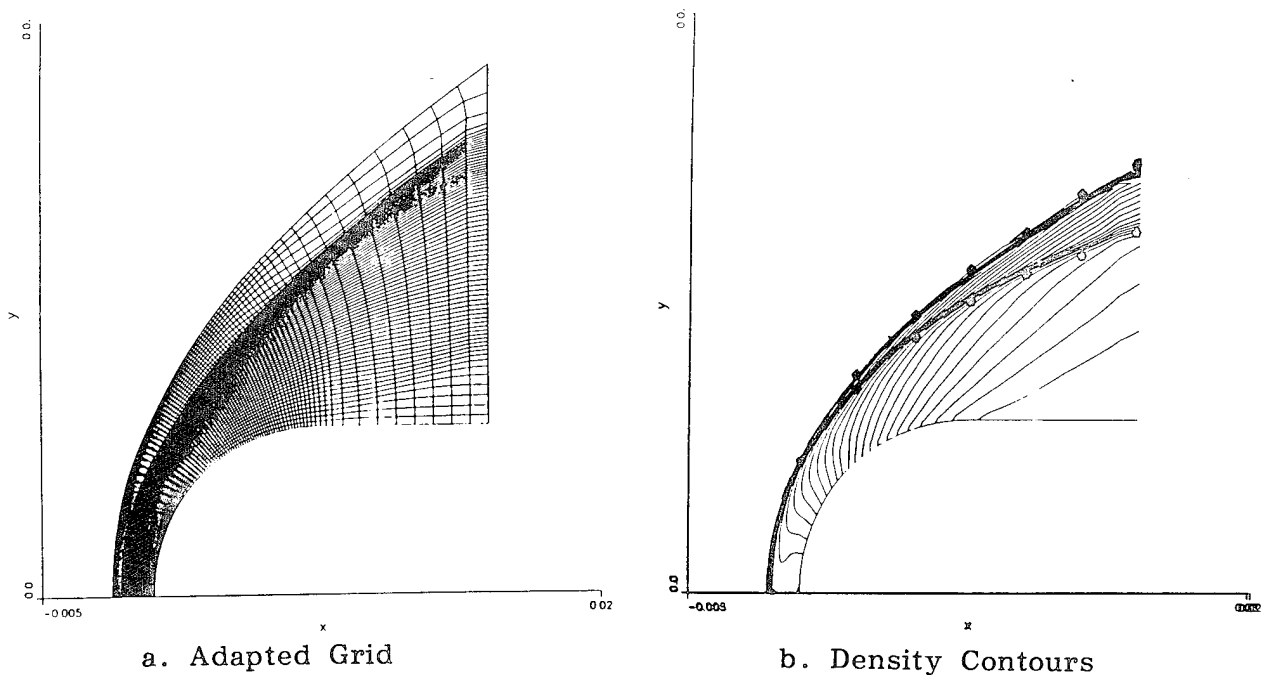
Fig. 2.10.2.2. Adapted grid and computed density contours shown for
steady shock-induced combustion.

broadens in the streamwise direction. This improvement is attributed solely
to the additional grid points in the induction zone resulting from adaption
and, again, the results with both reaction sets were comparable. Sussman
[61] states that in addition to grid adaptation, he had to modify the treat-
ment of the chemical source term to accurately compute the induction zone.
Our experience with CRAFT, indicates that when an appropriately adapted
grid is used, the induction zone can be captured without any modifications.
Note the very sharp capturing of the flame front by CRAFT.

The second test case simulates an unsteady, shock-induced combus-
tion flowfield. The geometry and mixture are the same as in the previously
described steady case, but the freestream Mach Number now has a lower
value of 4.79. In the experiment, high frequency oscillations are observed in
the shadowgraphs (Figure 2.10.2.3). This oscillatory behavior is thought to
be the result of combustion instabilities caused by the interaction between
the bow shock and the compression waves generated by the energy release.
A detailed discussion of the proposed instability mechanisms can be found in
Ref. 60.

38
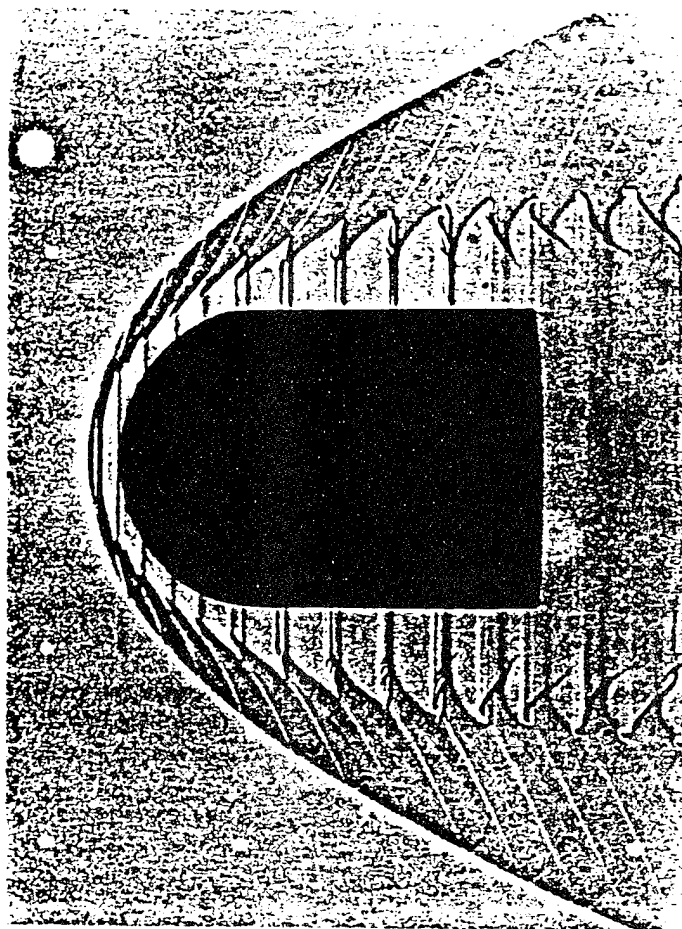
Fig. 2.10.2.3. Shadowgraph of unsteady M=4.79 case from Lehr.

The simulation was performed on an evenly spaced 166 x 121 grid utilizing the first reaction system[62] employed in the steady case. Second-order time-accuracy was employed for this unsteady calculation. Figure 2.10.2.4a shows density contours at one point in time illustrating the "pulsating" behavior of the energy release front. Figure 2.10.2.4b presents an x vs t diagram of density contours plotted along the centerline between the bow shock and the projectile nose. This figure illustrates the periodic movement of the energy release zone. The estimated frequency of this oscillation is approximately 450-500 KHz which is lower than the experimental value of 720. These results are similar to those obtained by Wilson & Sussman [60]. They demonstrated the sensitivity of the oscillation frequency to the $H-O_2$ chain branching reaction and were able to improve upon the predicted frequency by utilizing the rate expressions of Jachimowski [63]. We plan to repeat this unsteady calculation with these rates to assess this sensitivity.

(a).

(b).

| PRESSURE | DENSITY | DENSITY WEIGHTED H₂ MASS FRACTION |
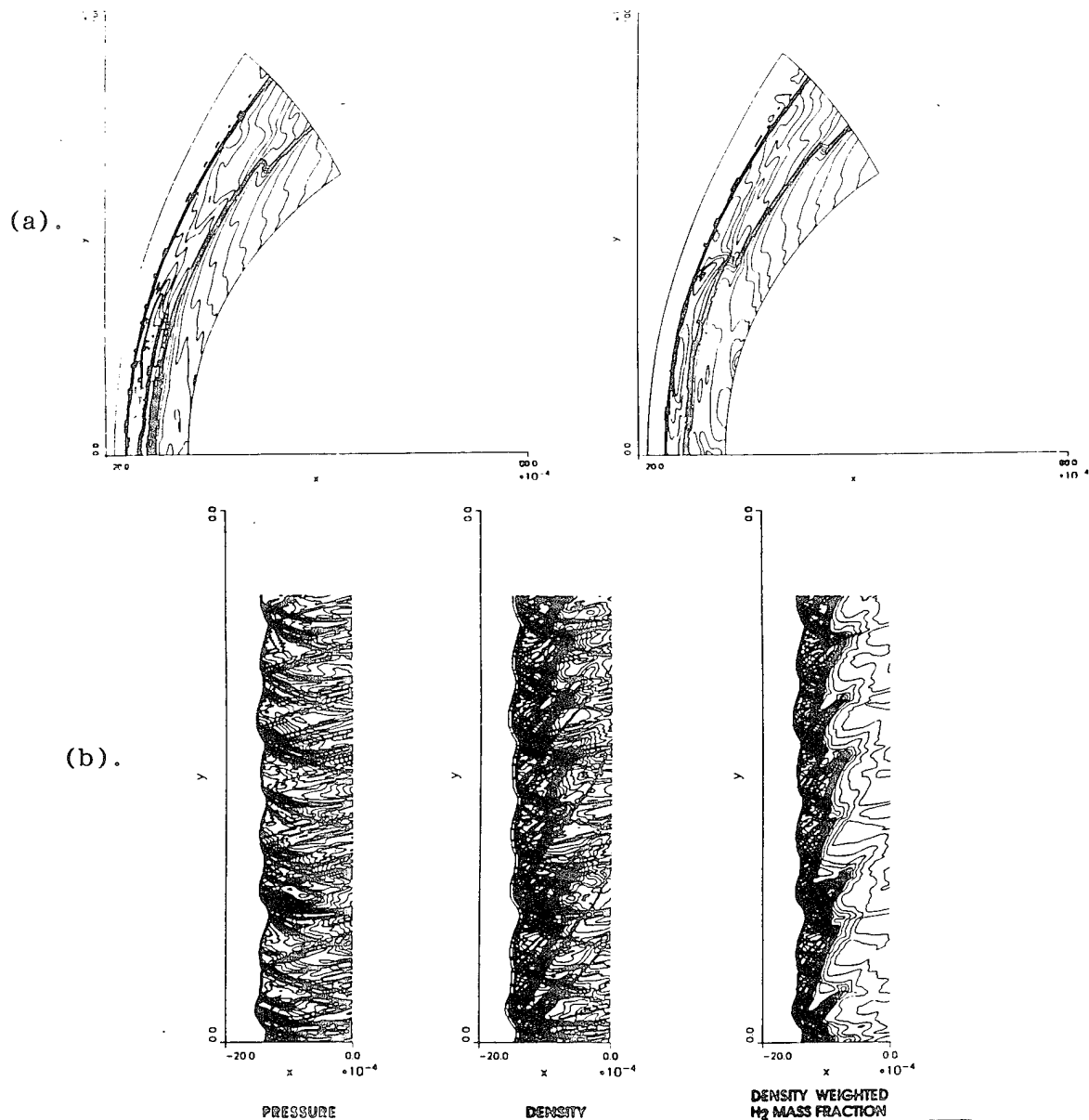
Fig. 2.10.2.4. Unsteady shock-induced combustion results: a)density contours at 3µs interval; and b) x-t along stagnation streamline.

2.10.3 Unsteady Turbulence Studies

Brown & Roshko[65] were amongst the earliest researchers to identify large scale coherent structures in shear layers with density gradients and their data has formed the basis for many unsteady simulations (see, e.g., the Euler simulation of Chien [66] with excitation forced at the dominant instability modes). The case of interest is described in Figure 2.10.3.1 (for helium and nitrogen streams) which shows the time-averaged

$$u_2 / u_1 = .33, \quad \rho_2 / \rho_1 = T_1 / T_2 = 7$$
$$M_1 = M_2 = .29$$

U VELOCITY
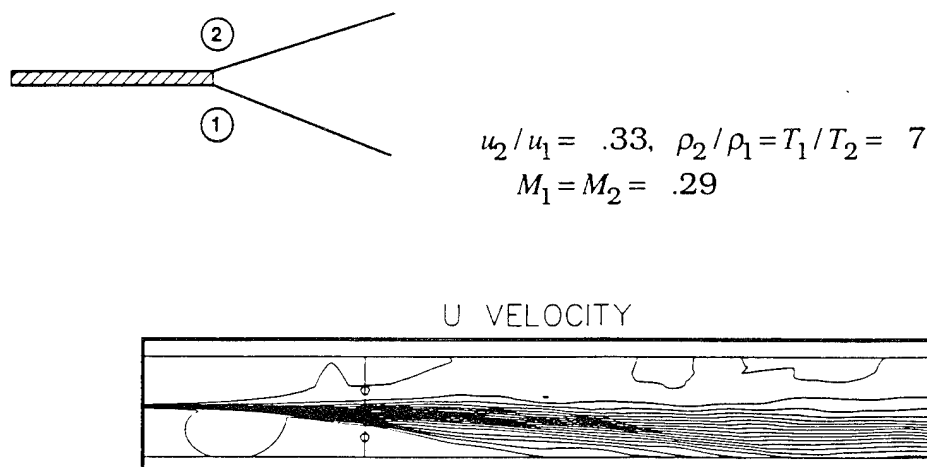
Fig. 2.10.3.1. Unsteady shear layer simulation with large density variations: a) schematic; and b) time-averaged solution.

structure of the shear layer in a reduced transverse domain (the computational domain extends well beyond what is displayed). The calculation is continuously processed to ascertain when time-invariance is achieved (via averaging over ~1,000 steps) and at what axial position asymptotic similarity is achieved. Conventional Favré-averaging is implemented to obtain mean and rms turbulent variables/stresses as summarized below in Table VIII which omits the subscale stress terms.

Table VIII. Density-Weighted (Favré) Averaging of Unsteady Flow Solutions

SOLUTION $\Rightarrow$ $\mathfrak{Q}$ $(X_i, t) = [\rho, \rho u, \rho v, \rho w, \rho e_t]$

PRIMITIVE VARIABLES

$\bar{\rho} = \int \rho dt \ / \ \Delta t$ where $\Delta t = \int dt$ over averging interval

$\tilde{u} = \int \rho u dt \ / \ \bar{r} Dt, \tilde{v} = ..., \tilde{w} = ...$

$\bar{P} = \int P dt \ / \ \Delta t$ where $P = (\gamma - 1)\left[\rho e_t - \frac{1}{2}(\rho u_i)^2 / \rho\right]$

$\tilde{T} = \int \rho T dt \ / \ \rho \Delta t = \bar{P}(\bar{\rho} R)$

RMS CORRELATION/STRESSES

$\overline{\rho' \rho'} = \int (\rho - \bar{\rho})^2 dt \ / \ \Delta t \qquad \overline{P'P'} = \int (P - \bar{P})^2 dt \ / \ \Delta t$

$\overline{u'u'} = \int (u - \tilde{u})^2 dt \ / \ \Delta t \ ; \ \overline{v'v'} = ...; \ \overline{w'w'} = ...$

$\overline{u'v'} = \int (u - \tilde{u})(v - \tilde{v}) / \Delta t \ ; \ \overline{u'w'} = ...; \ \overline{v'w'} = ...$

$\overline{T'T'} = \int (T - \tilde{T})^2 dt \ / \ \Delta t \ ; \ ...$

$\overline{T'u'} = \int (T - \tilde{T})(u - \tilde{u}) dt \ / \ \Delta t \ ;$

41

Figure 2.10.3.2 shows instantaneous contours of nitrogen mass fraction and clearly indicates the presence of unsteady large scale turbulent structures. Referring to Figure 2.10.3.1, a stable asymptotic state is achieved at the vertical position indicated. Figure 2.10.3.3 exhibits the time variation of axial velocity at 4 points in this shear layer (see Figure 2.10.3.1 for the positions). Figure 2.10.3.4 exhibits the Favré and Reynolds time-averaged mean axial velocity profile at this axial position and at several positions downstream (the downstream solutions still exhibit some unsteadiness indicating that the calculation is not yet fully time-invariant). Figure 2.10.3.5 exhibits axial rms velocity fluctuations profiles ($\overline{u'}$). Analogous results for instantaneous density fluctuations at the same 4 points, and, for the rms density ($\overline{\rho'}$) fluctuation profiles at the same 4 axial stations are shown in Figures 2.10.3.6 and 2.10.3.7, respectively. The qualitative characteristics of the results obtained are quite satisfying and were obtained with low frequency/low amplitude forcing with and without the utilization of a subscale stress model (differences were found to be negligible). Quantitative comparisons with time-averaged density fluctuation data are quite good as shown in Figure 2.10.3.8.
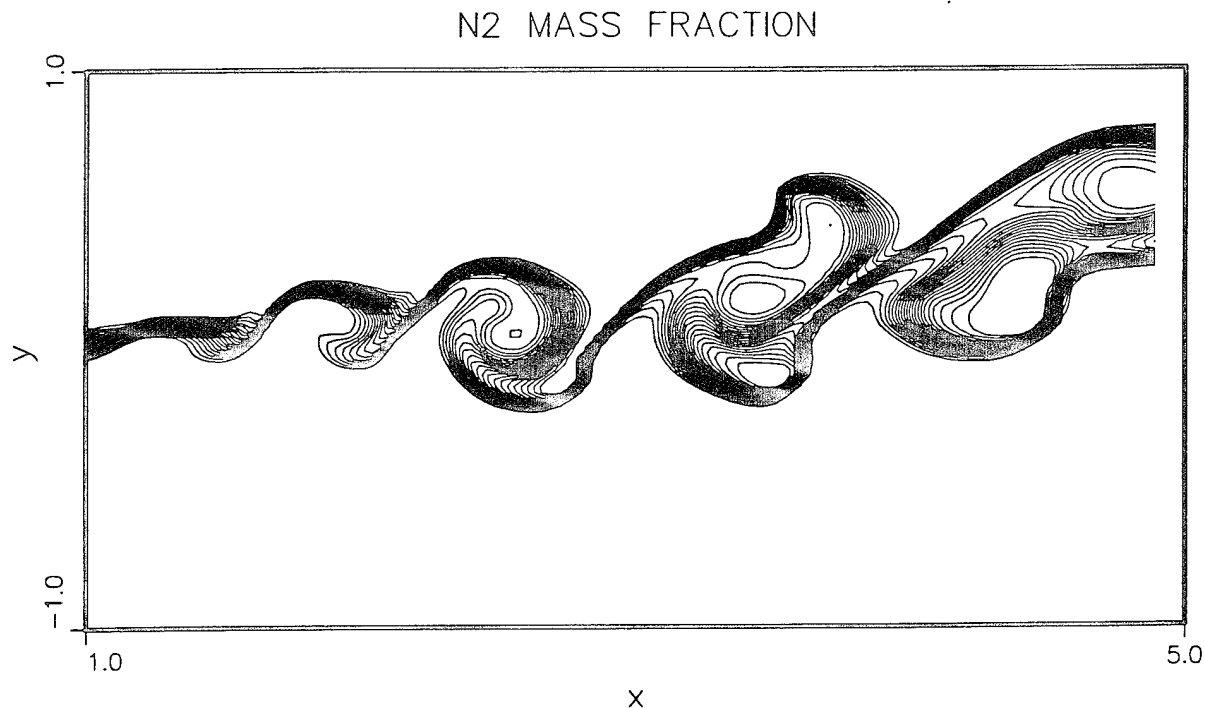
N2 MASS FRACTION

Fig. 2.10.3.2. Instantaneous contours of Nitrogen mass fraction.
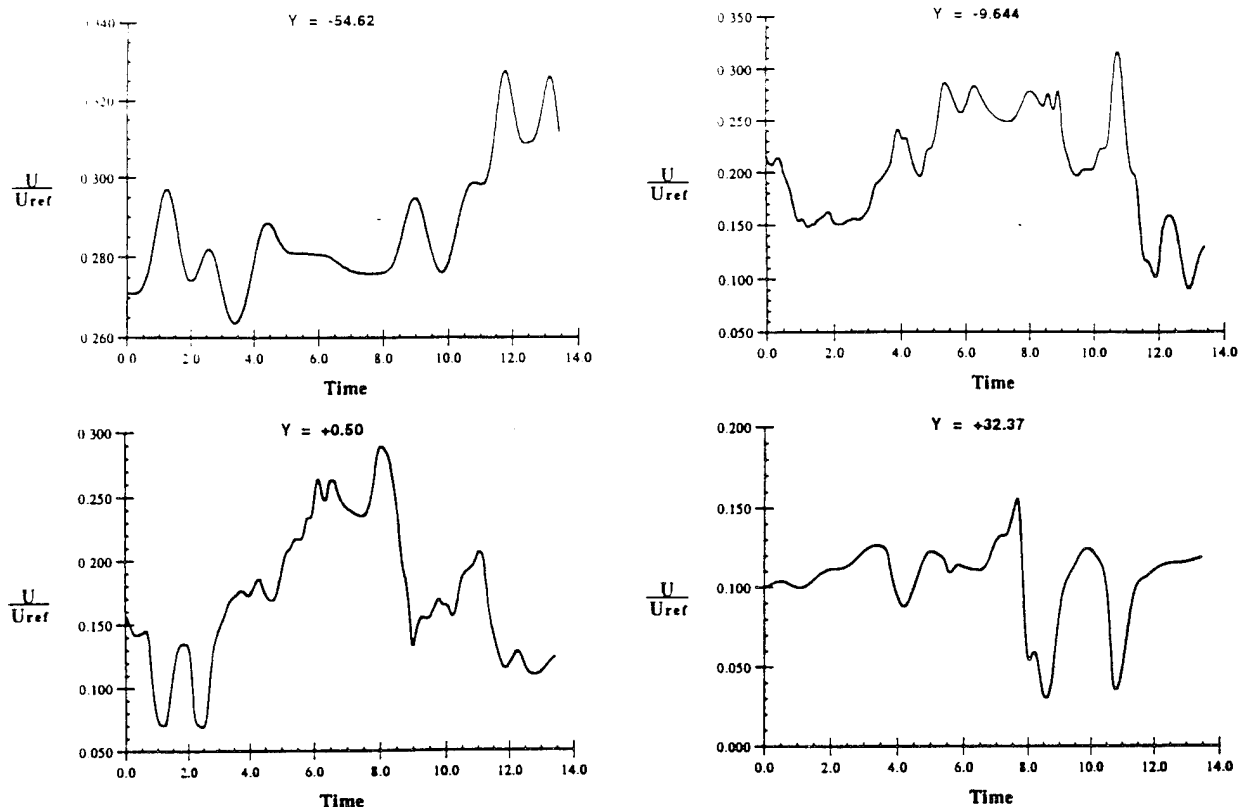
Fig. 2.10.3.3. Instantaneous axial velocity at four positions in shear layer.
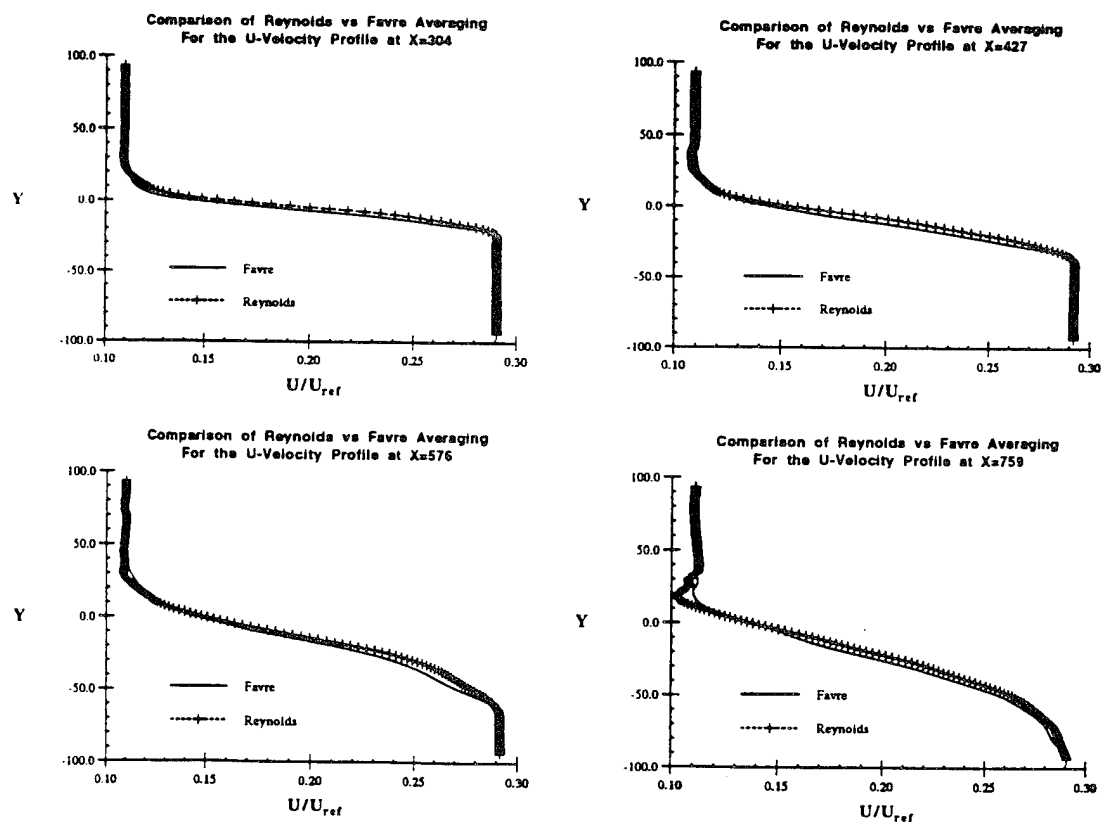
Fig. 2.10.3.4. Time-averaged mean axial velocity profiles at several axial stations.

43
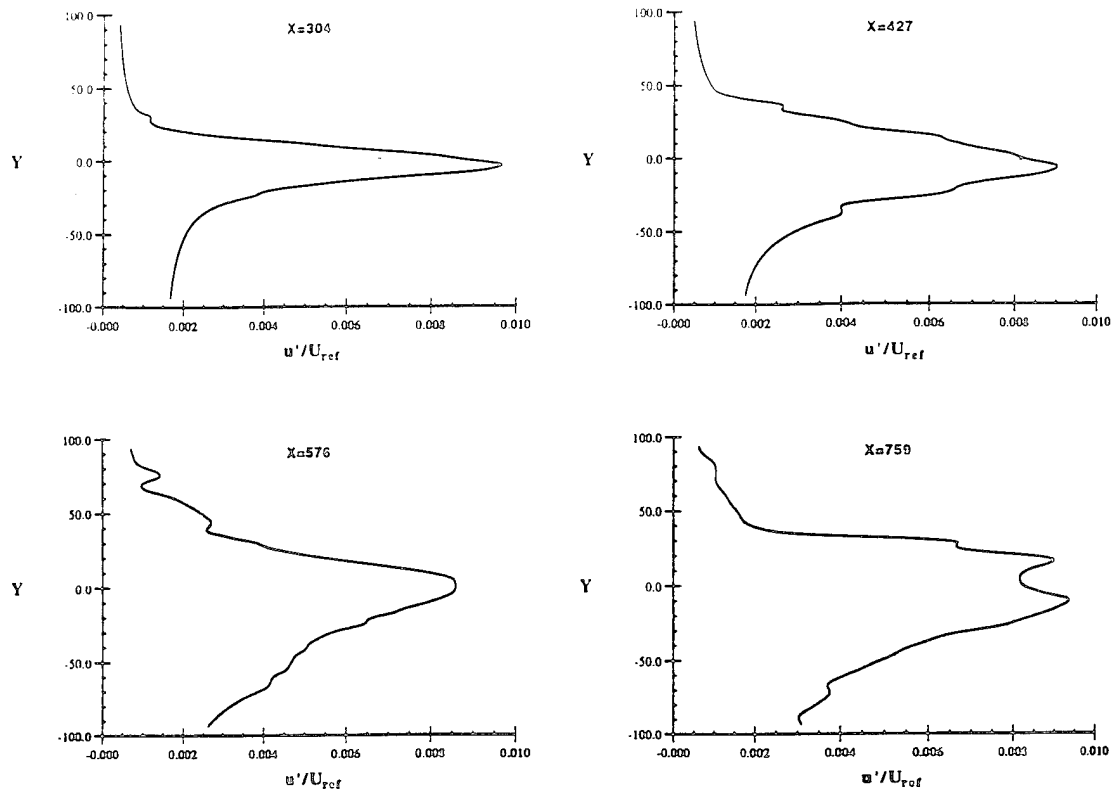
Fig. 2.10.3.5. RMS axial velocity fluctuation profiles at several axial stations.
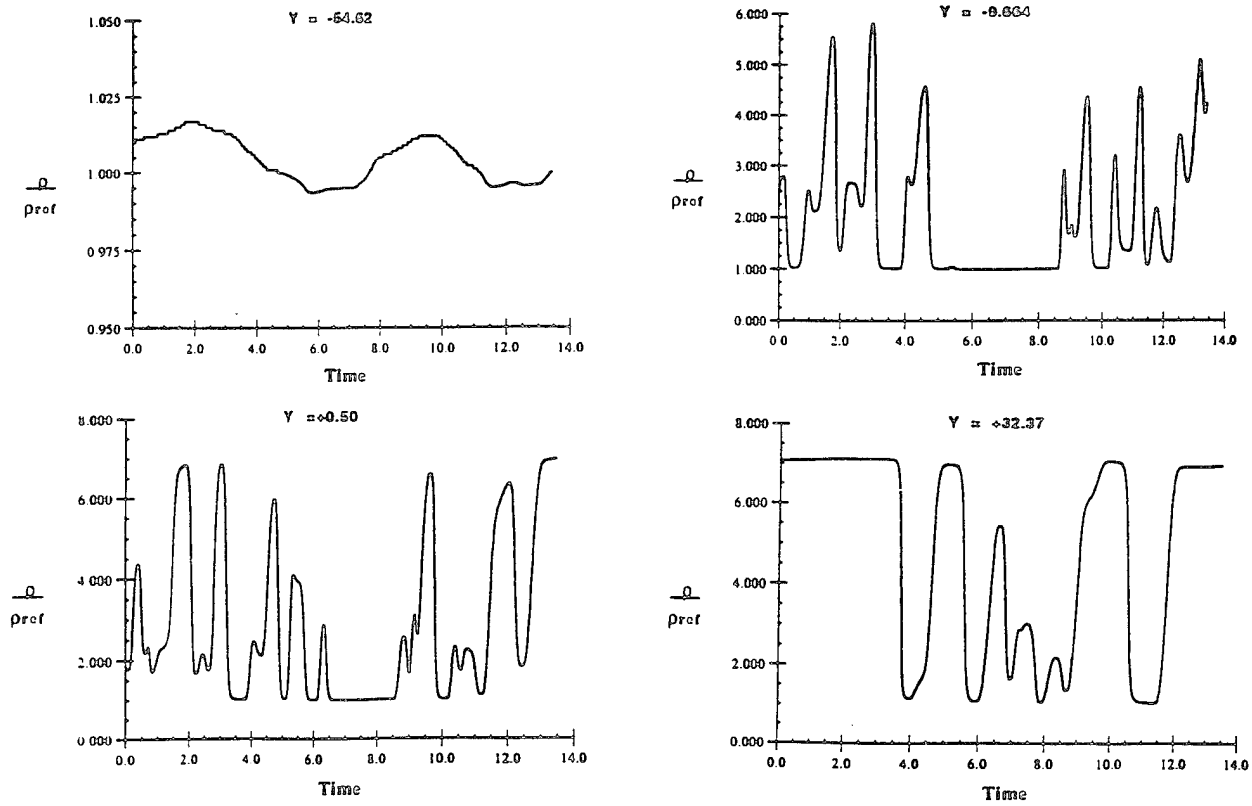
Fig. 2.10.3.6. Instantaneous densities at four positions in shear layer.

44
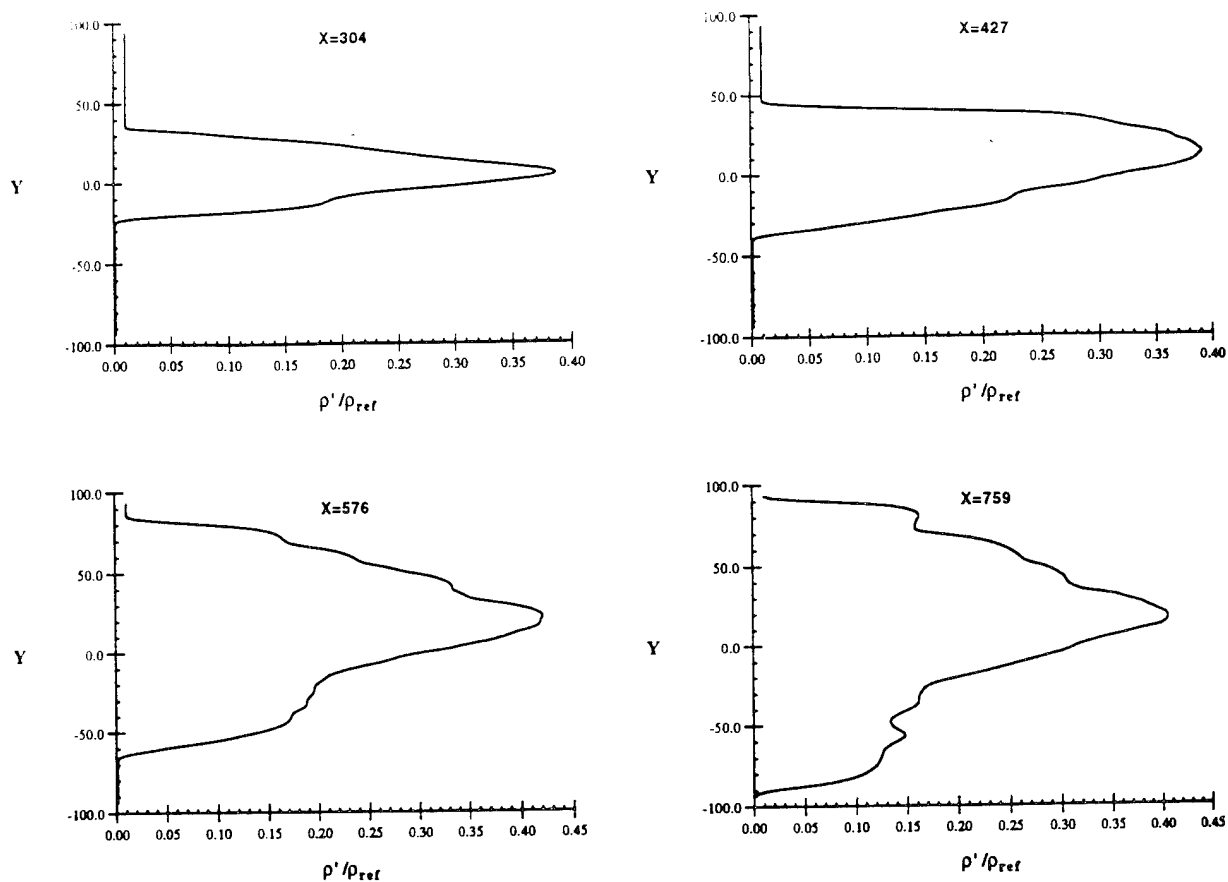
Fig. 2.10.3.7. RMS density fluctuation profiles at several axial stations.
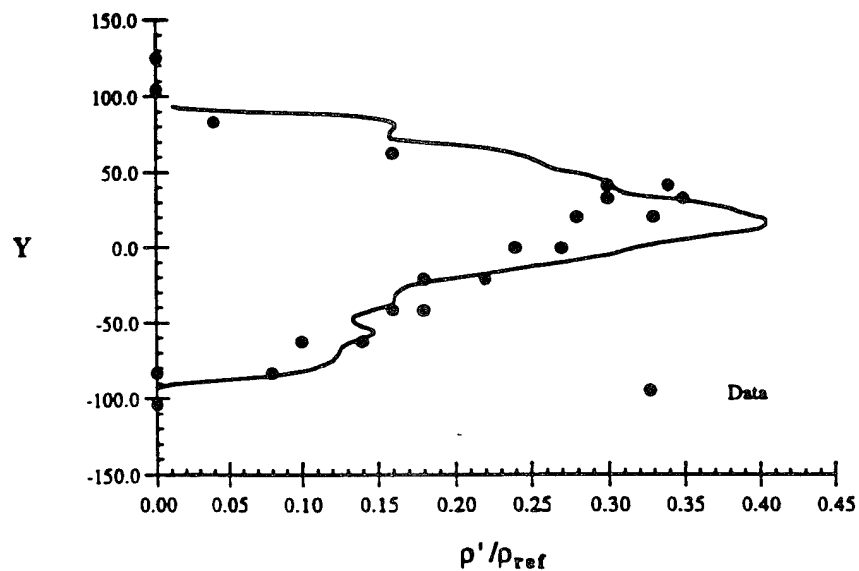
Fig. 2.10.3.8. Comparison of RMS density fluctuation with data for shear layer with density gradients.

45

2.10.4 Gas/Gas Gun Chamber Studies

Simulations of high-pressure, plasma injection into a gun chamber and subsequent projectile acceleration were performed at early stages of our ETC work as an initial assessment of numerics. For the case described, both the plasma and propellant were represented by air and a non-combusting firing was simulated. The plasma was injected into the gun mixing chamber and a total duration of ~2ms was simulated. During the plasma injection process, a complex flow structure was observed in the chamber with strong, embedded discontinuities. Multiple shock reflections occurred and a Mach disc formed downstream of the plasma injector. An unsteady shear layer is found to emanate from the Mach disc triple point and separates the hot core from the tube walls. The plasma shock wave travels to the base of the projectile protrusion and minor reflections are observed. However, most of the blast wave travels along the projectile protrusion until it reflects from the far end. This initiates projectile motion while the reflected shock rapidly travels back to interact with the Mach disc structure. At this point (the end of simulation), the injector is close to "unstarting." Contours of pressure and temperature are shown in Figures 2.10.4.1 and 2.10.4.2 at various time instances to provide snapshots of the flowfield while Figure 2.10.4.3 shows the variation of pressure along the centerline of the mixing chamber at different times.

"LOG PRESSURE IN CHAMBER"
"TIME 0.39 ms"

"LOG PRESSURE IN CHAMBER"
"TIME 0.64 ms"

"LOG PRESSURE IN CHAMBER"
"TIME 0.87 ms"
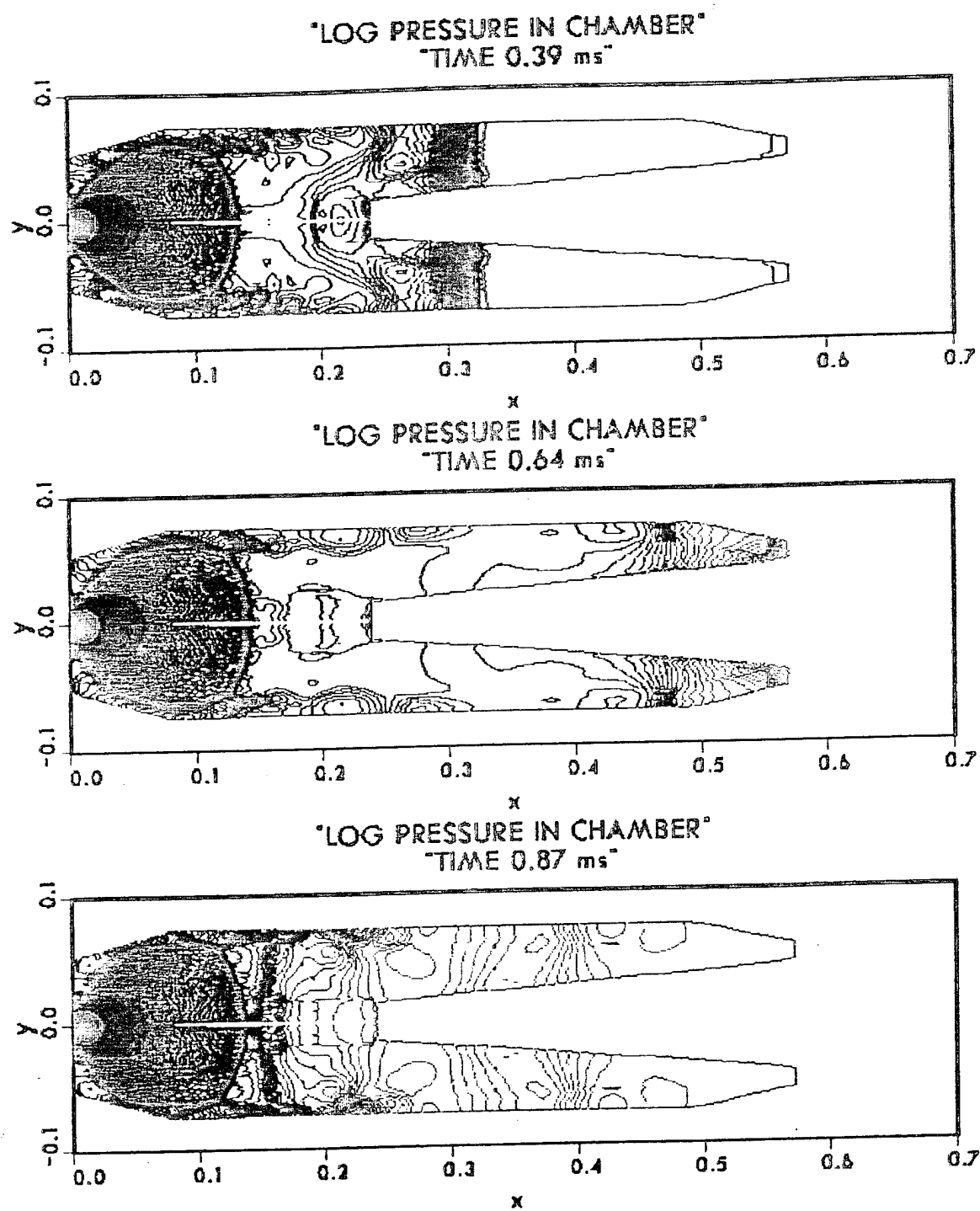
Fig. 2.10.4.1. Pressure contours at: a) 0.39ms; b) 0.64ms; c) 0.87ms.

47

"TEMPERATURE IN CHAMBER"
"TIME 0.39 ms"

"TEMPERATURE IN CHAMBER"
"TIME 0.64 ms"

"TEMPERATURE IN CHAMBER"
"TIME 0.87 ms"
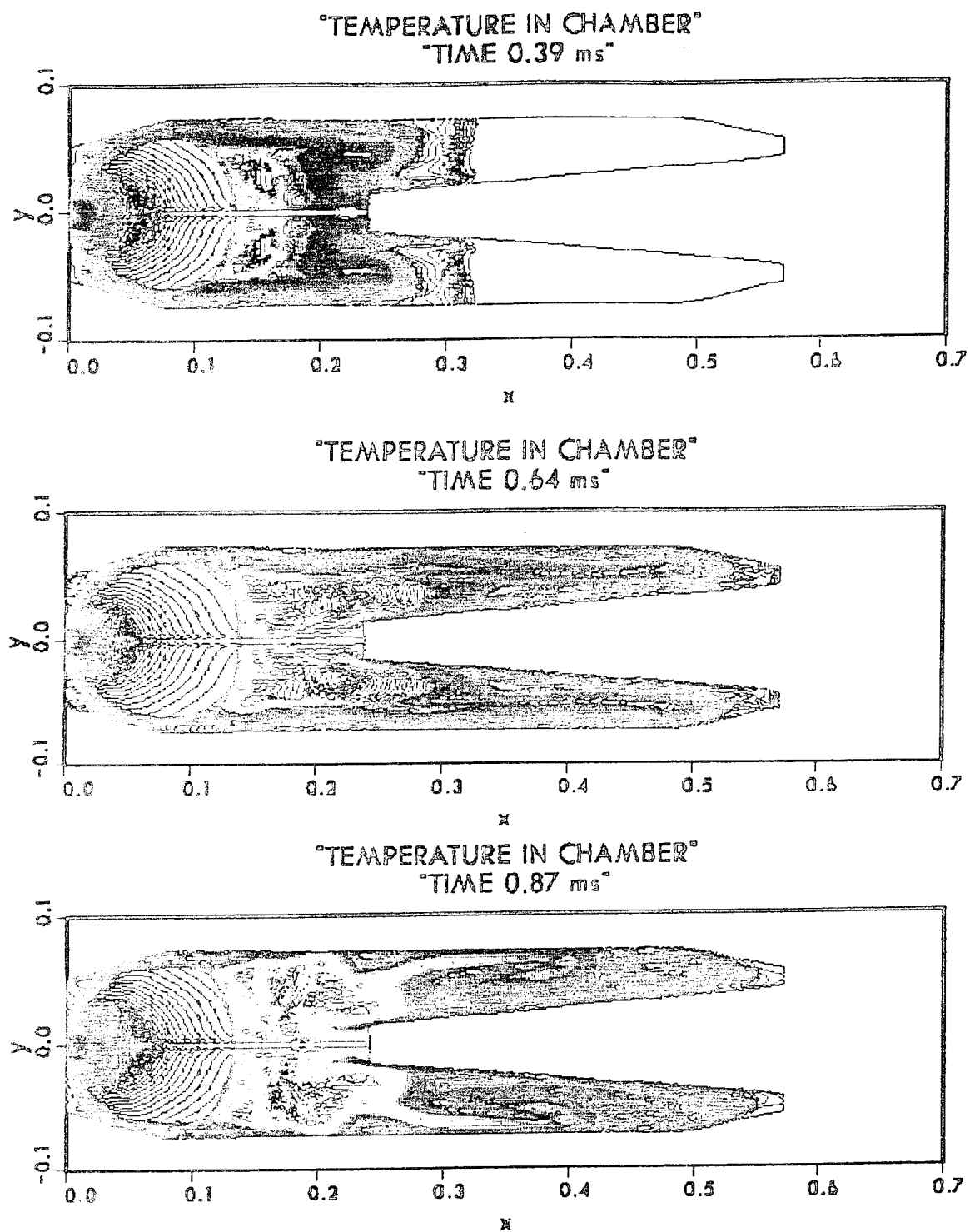
Fig. 2.10.4.2. Temperature contours at: a) 0.39ms; b) 0.64ms; c) 0.87ms.

48
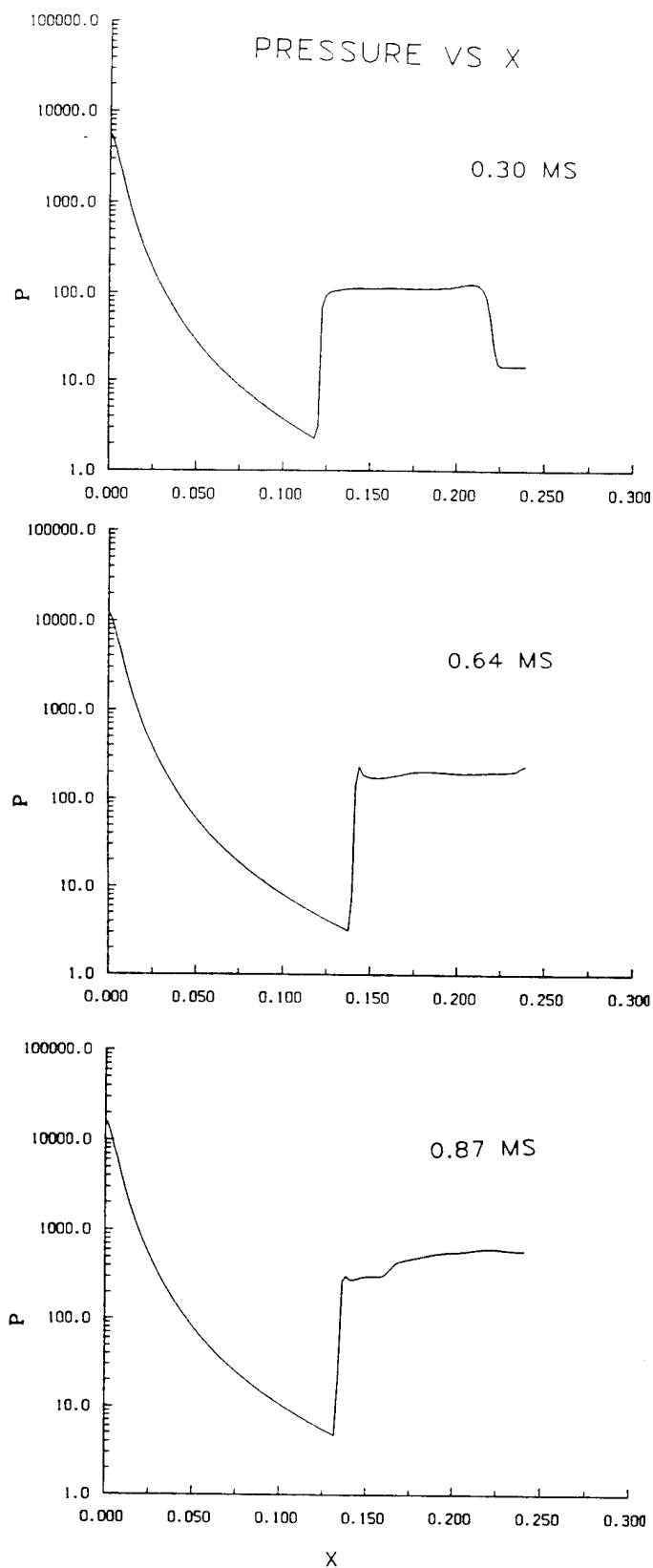
Fig. 2.10.4.3. Pressure distribution along centerline at: a) 0.30ms;
b) 0.64ms; c) 0.87ms.

49

3.0 MULTI-PHASE FORMULATION IN CRAFT FOR GAS/LIQUID SYSTEMS

Newer gun design concepts, such as the Electrothermal-Chemical (ETC) gun and the Regenerative Liquid Propellant Gun (RLPG), have utilized liquid propellants, either wholly or in conjunction with solid propellants, to provide enhanced performance. The attraction of liquid propellants lies in their high chemical energy content. Furthermore, they offer a potential for better control and tailoring of the pressure-time curve since the interaction between the gas and liquid phases plays a dominant role in the combustion process. For example, one of the proposed designs for the electrothermal-chemical gun involves using bulk liquid propellant whose combustion is controlled by injecting high pressure plasma which ignites and energizes the liquid propellant. The transient mixing processes at the interface of the liquid and gaseous plasma are very complex and involve the generation of droplets from the bulk liquid phase. The simulation of such complex multiphase processes requires an integrated code which permits a gas-phase, a bulk-liquid phase, and a discrete droplet phase to coexist, with each phase potentially being in non-equilibrium with the other phases. A first-principles simulation of droplet formation in this environment is possible at a fundamental level, but would entail substantive research and very specialized solution adaptive gridding to make it into a practicable component of an engineering-oriented code. Empirical models of droplet formation [67] are not catered to the ETC environment and no relevant modeling work in this area has been performed to date. In view of the state-of-the-art having such inadequacies, an approximate gas-liquid equilibrium approach was formulated as a first step towards the subsequent development of a more generalized non-equilibrium approach (to be described in Section 6). The gas-liquid equilibrium formulation is described in what follows.

3.1 GAS-LIQUID EQUILIBRIUM FORMULATION

The basic premise of the gas-liquid equilibrium formulation is the assumption of dynamic and thermal equilibrium between the two distinct phases i.e. the gas and liquid phases have identical velocity and temperature at any spatial point in which they coexist. The equilibrium assumption allows us to combine the conservation equations for each individual phase to

50

obtain a unified set of equations for the mixture. The equation system is completed by enforcing Amagat's law between the phases – the gas and liquid phase pressures are identical while the partial volumes sum up to the cell volume. The conservation equations are supplemented by the equations of state for the gas and liquid phases. The gas-phase has a generalized virial equation of state to account for compressibility effects at high pressures, as will be discussed in detail later. The liquid equation of state can be specified either in a tabular form, or as an analytical function. The basis of the gas-liquid equilibrium formulation is summarized in Table IX. The methodology described has been adapted from procedures employed by Coffee [68] for RLPG simulation.

Table IX. Basis of Gas/Liquid Equilibrium Formulation

$$
\boxed{
\begin{array}{c}
P_L, \vec{U}_L, T_L, V_L \\
\textit{LIQUID} \\
\hline
P_G, \vec{U}_G, T_G, V_G \\
\textit{GAS}
\end{array}
}
$$

- TWO-PHASE MIXTURE IS GOVERNED BY AMAGAT'S LAW
  TOTAL VOLUME = SUM OF PARTIAL VOLUMES
  $$\phi_G + \phi_L = 1$$

  PRESSURE IS IDENTICAL IN BOTH PHASES
  $$P_G = P_L$$

- GAS AND LIQUID PHASES TAKEN TO BE IN EQUILIBRIUM
  $$\bar{U}_G = \bar{U}_L$$
  $$T_G = T_L$$

THIS ALLOWS US TO FORMULATE GLOBAL CONSERVATION EQUATIONS FOR THE MIXTURE
RATHER THAN SEPARATE EQUATIONS FOR EACH PHASE

The conservation equations for the gas-liquid mixture are written in vector form as

$$
\begin{aligned}
\frac{\partial}{\partial t}\iiint Q\,dV + \iint\left(E_{i+1/2} - E_{i-1/2}\right)d\eta\,d\zeta \\
+\iint\left(F_{j+1/2} - F_{j-1/2}\right)d\xi\,d\zeta + \iint\left(G_{k+1/2} - G_{k-1/2}\right)d\xi\,d\eta \\
= \frac{1}{\mathrm{Re}}\iint\left(R_{i+1/2} - R_{i-1/2}\right)d\eta\,d\zeta + \frac{1}{\mathrm{Re}}\iint\left(S_{j+1/2} - S_{j-1/2}\right)d\xi\,d\zeta \\
+ \frac{1}{\mathrm{Re}}\iint\left(T_{k+1/2} - T_{k-1/2}\right)d\xi\,d\eta + \iiint D\,dV
\end{aligned}
$$

(3.1.1a)

5 1

Here, the nomenclature used is the same as that of the previous section with Q being the vector of dependent variables, while E, F, and G are the flux vectors in the ξ, ζ, and η directions, respectively. These vectors are given as

$$
Q = \begin{bmatrix} \rho_m \\ \rho_m u \\ \rho_m v \\ \rho_m w \\ e_m \\ \rho_i \phi_g \\ \vdots \\ \rho_{n-1} \phi_g \end{bmatrix}; \quad
E = \begin{bmatrix} \rho_m U \\ (\rho_m Uu + \ell_x P) \\ (\rho_m Uv + \ell_y P) \\ (\rho_m Uw + \ell_z P) \\ (e_m + P)U \\ \rho_i U \phi_g \\ \vdots \\ \rho_{n-1} U \phi_g \end{bmatrix}; \quad
F = \begin{bmatrix} \rho_m V \\ (\rho_m Vu + m_x P) \\ (\rho_m Vv + m_y P) \\ (\rho_m Vw + m_z P) \\ (e_m + P)V \\ \rho_i V \phi_g \\ \vdots \\ \rho_{n-1} V \phi_g \end{bmatrix}; \quad
G = \begin{bmatrix} \rho_m W \\ (\rho_m Wu + n_x P) \\ (\rho_m Wv + n_y P) \\ (\rho_m Ww + n_z P) \\ (e_m + P)W \\ \rho_i W \phi_g \\ \vdots \\ \rho_{n-1} W \phi_g \end{bmatrix}
\qquad \textbf{(3.1.1b)}
$$

The metrics (ℓ_x, ℓ_y, ℓ_z), the volumetric fluxes U, V, and W, and the mixture total internal energy, e_m, have the same definitions as in Section 2. As before, we formulate the equations for n general species. However, unlike the pure gas-phase formulation, we now have two phases present and we designate the nth species to be the bulk liquid phase. The remainder of the (n-1) species are the various gaseous chemical species which are individually modelled. The first five equations are the conservation equations for the gas/liquid mixture where ρ_m is the mixture density and is defined as follows:

$$
\rho_m = \phi_g \rho_g + \left(1 - \phi_g\right)\rho_L
\qquad \textbf{(3.1.2)}
$$

In Eq. (3.1.1b), ϕ_g is the volumetric fraction of the gas, while ρ_g and ρ_L are the gas and liquid densities. Since the gas phase is composed of (n-1) different species, we define ρ_g as

$$
\rho_g = \sum_{i=1}^{n-1} \rho_i
\qquad \textbf{(3.1.3)}
$$

We define a relative gas mass fraction, y_i, as follows:

$$
y_i = \frac{\rho_i}{\rho_g} \quad \{i = i, n-1\}
\qquad \textbf{(3.1.4)}
$$

Note that the relative gas mass fractions, y_i, are distinct from the species mass fractions $c_i \left[= \dfrac{\rho_i \phi_g}{\rho_m} \right]$. The mixture enthalpy is given by

$$\rho_m h_m = \rho_g \phi_g h_g + \rho_L \left(1 - \phi_g \right) h_L$$
$$h_g = \sum_{i=1}^{n-1} y_i \left[h_i^{of} + h_i(T) \right]$$

(3.1.5)

The conservation equations in Eq. (3.1.2) are supplemented by the equations of state for the gas and liquid to complete the system. The pressure of the gas is the sum of the individual gas species and is given as

$$P_g = \sum_{i=1}^{n-1} P_{gi}$$

(3.1.6)

The pressure of each individual gas species is specified using the non-ideal (thermally imperfect) virial equation of state as follows:

$$P_{gi} = \frac{\rho_i \overline{R} T}{M_i} \left[1 + B_v \rho_g + C_v \rho_g^2 \right]$$

(3.1.7)

The coefficients B_v and C_v are the second and third virial coefficients for the gaseous mixture. Typically, the second and third virial coefficients are available for individual species. However, the methodology to deduce the virial coefficients for a gaseous mixture from these individual values is not well defined. Analytical expressions have been derived for binary mixtures of two species; however, such expressions involve defining additional cross-coefficients which are difficult to obtain. In view of these uncertainties, the virial coefficients for a generalized mixture of n species have been approximated by a simplified mass weighted averaging of individual species coefficients [69] as given below

$$B_v = \sum y_i b_v^i$$
$$C_v = \sum y_i c_v^i$$

(3.1.8)

The liquid equation of state is specified either in tabular form or as an analytical function, if available. In the studies to be described, we have used the following analytical expression employed by Coffee [68]:

$$P_L = \frac{k_1}{k_2}\left[\left(\frac{\rho_L}{\rho_0}\right)^{k_2} - 1\right]$$

(3.1.9)

where ρ_0 is the liquid density at a reference state, k_1, is the bulk modulus at zero pressure, and the index k_2 is a measure of the liquid's compressibility.

To complete the thermochemical specification, we have to obtain the gas volumetric fraction, ϕ_g, and the temperature of the mixture from the conserved variables, Q. As in the pure gas phase case, the decoding procedure is an iterative process. However, the gas/liquid problem is more complicated since we have to simultaneously iterate for two variables (T and ϕ_g) rather than just the temperature. The two conditions iterated on are as follows:

$$h_m - \frac{P}{\rho_m} = \varepsilon_m = \frac{e_m}{\rho_m} - \frac{1}{2}\left(u^2 + v^2 + w^2\right)$$

(3.1.10)

$$P_g = P_L$$

The Newton-Raphson iterative procedure for Eq. (3.1.10) is written symbolically as

$$\begin{bmatrix} \dfrac{\partial \varepsilon_m}{\partial T} & \dfrac{\partial \varepsilon_m}{\partial \phi_g} \\[2ex] \dfrac{\partial\left(P_g - P_L\right)}{\partial T} & \dfrac{\partial\left(P_g - P_L\right)}{\partial \phi_g} \end{bmatrix}^P \begin{bmatrix} dT \\[2ex] d\phi_g \end{bmatrix} = -\begin{bmatrix} \left(\varepsilon^P - \varepsilon_m\right) \\[2ex] \left(P_g - P_L\right)^P \end{bmatrix}$$

(3.1.11)

$$T^{P+1} = T^P + (dT)^P$$

$$\phi_g^{P+1} = \phi_g^P + \left(d\phi_g\right)^P$$

Eq. (3.1.11) is iterated on until the error on the right hand side is reduced to machine accuracy, thereby yielding the mixture temperature and gas volumetric fraction.

3.2 MATRIX MODIFICATIONS

The inclusion of the gas-liquid thermochemistry described above into the upwind/implicit methodology is complex and requires the re-evaluation of the flux Jacobians, as well as the eigenvalues and eigenvectors. As we had previously discussed in Section 2.4, the Jacobian of the flux vectors requires the evaluation of the derivatives such as $\frac{\partial P}{\partial \rho_m}, \frac{\partial P}{\partial e_m}$, etc. To evaluate the derivatives of pressure we begin by looking at the functional dependence of pressure

$$P_g = f\left(\rho_g, T, \phi_g\right), \quad dP_g = f\left(d\rho_g, dT, d\phi_g\right)$$
$$P_L = f\left(\rho_L, T, \left(1 - \phi_g\right)\right), \quad dP_L = f\left(d\rho_L, dT, -d\phi_g\right)$$

(3.2.1)

Inspection of Eq. (3.2.1) reveals that while the pressure differential depends on $(d\phi_g)$, ϕ_g itself is not a variable in the vector Q. Therefore the primary obstacle in determining the pressure derivative is in eliminating the dependence of the pressure differential on $(d\phi_g)$. This is done by enforcing the differential form of Amagat's law,

$$dP_g = dP_L$$
$$\therefore d\phi_g = G\left(d\rho_L, d\rho_g, dT\right)$$

(3.2.2a)

Eq. (3.2.2), is substituted back into Eq. (3.2.1) to obtain the pressure differential in terms of the variables solved in the vector Q as follows:

$$dP = dP_g = dP_L = H\left(d\rho_L, d\rho_g, dT\right)$$

(3.2.2b)

The details of the Jacobian A are given in Appendix A.

The acoustic speed of the two-phase system is determined from the eigenvalues of the Jacobian (see Appendix B for details) and is given by

$$\frac{1}{\rho_m c_m^2} = \frac{1}{\tilde{\gamma}}\left[\frac{\phi_g}{\sum\limits_{n-1}\rho_i c_i^2} + \frac{\phi_L}{\rho_L c_L^2}\right]$$

(3.2.3)

In the above expression

$$c_i = \sqrt{\left(\frac{\partial P_g}{\partial \rho_i}\right)_T} = \text{isothermal speed of sound of i}^{\text{th}} \text{ gas species}$$

(3.2.4)

$$c_L = \sqrt{\left(\frac{\partial P_L}{\partial \rho_L}\right)_T} = \text{isothermal speed of sound of liquid}$$

and

$$\tilde{\gamma} = \frac{\left(\sum_{n-1} \rho_i \phi_g C_{P_i} + \rho_L \phi_L C_{P_L}\right)}{\left(\sum_{n-1} \rho_i \phi_g C_{P_i} + \rho_L \phi_L C_{P_L}\right) - \beta_m}$$

(3.2.5)

$$\beta_m = \left(\frac{\phi_g C_L^2 \rho_L}{\phi_L \sum_{n-1} \rho_i C_i^2 + \phi_g \rho_L C_L^2}\right)\frac{\partial P_g}{\partial T} + \left(\frac{\phi_L \sum_{n-1} \rho_i C_i^2}{\phi_L \sum_{n-1} \rho_i C_i^2 + \phi_g \rho_L C_L^2}\right)\frac{\partial P_L}{\partial T}$$

As Eq. (3.2.3) indicates, the acoustic speed in a two-phase gas/liquid mixture behaves differently than in either a pure gas or a pure liquid. For two-phase mixtures, the acoustic speeds of the individual phases do not combine in a linear fashion, but instead exhibit a harmonic relationship. The variation of the acoustic speed with the volumetric fraction of the gas (for a given pressure and temperature) has a "bath-tub" shape; while the values at the two limits are the respective single phase values, the acoustic speed drops sharply away from these limits. The strong dependence of the acoustic speed on the volumetric fraction puts more stringent requirements on the numerical algorithm since it is now required to propagate waves with the correct speed in mixtures where the two-phase composition is varying rapidly (e.g. across the plasma/liquid propellant mixing layer. The upwind methodology in CRAFT enables us to compute these waves accurately, as we shall demonstrate for two-phase shock tube unit problems later in this section.

3.3 PLASMA COUPLING PROCEDURE

To simulate ETC gun systems, we have to model the injection of plasma into the chamber. The plasma, which initiates and sustains the combustion of the propellant, is a critical component of the ETC gun system.

The mass flux and properties of the plasma being injected depend upon the instantaneous pressure field within the gun chamber since the plasma is subsonic for a substantial part of the injection cycle. Hence, to compute accurate injection properties for the plasma, the plasma generation code must be coupled to the CRAFT code. The plasma generation code used in our ETC simulations has been developed by Powell at ARL (see Ref. 70 for details). The code for plasma generation is one-dimensional, quasi-steady, and isothermal, and has been found to provide adequate results for ETC simulation for varied conditions.

It responds "instantaneously" to the chamber conditions at the injector interface and cannot deal with very high pressures that would induce "backflow" (flow from chamber into plasma generator). Under such conditions, injector "door" is shut temporarily. The coupling procedure between CRAFT and Powell's code is illustrated in Table X. This coupling procedure has been verified by comparing the Mach number at the injection plane for the coupled solution with that computed by the plasma code given measured back pressures from an experimental firing. Such a Mach number comparison is shown in Fig. 3.3.1. These results indicate that the coupling procedure is functioning adequately.

Table X. Plasma Coupling Procedure

POWELL'S QUASI-STEADY 1D PLASMA CODE FOR CAPILLARY

CRAFT MULTI-DIMENSIONAL SIMULATION FOR GUN CHAMBER

COUPLING BOUNDARY

I(t)

CURRENT SPECIFIED AS INPUT FROM EXPERIMENTAL DATA

PLASMA CODE

P(t)

VELOCITY, TEMPERATURE AND PRESSURE (IF CHOKED) COMPUTED BY PLASMA CODE/SPECIFIED AS INJECTION CONDITION TO CRAFT

U_{PL}, T_{PL}, P_{PL}

CRAFT CODE

PRESSURE AT COUPLING PLANE COMPUTED BY CRAFT SPECIFIED AS BOUNDARY CONDITION TO PLASMA CODE

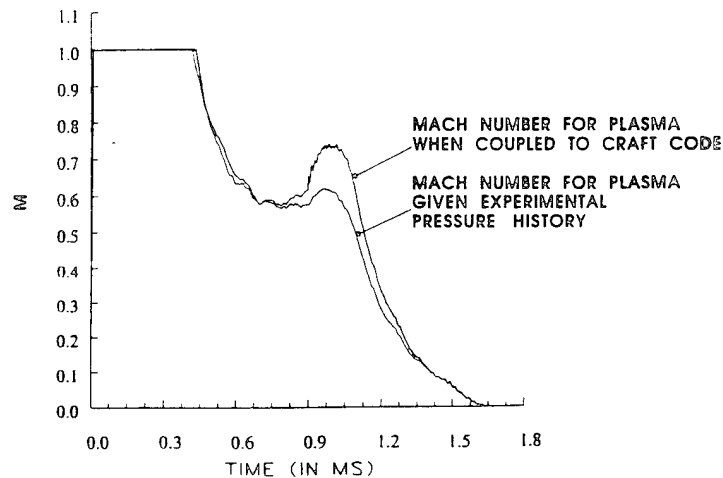Fig. 3.3.1. Inflow Mach number history for plasma compared for computed chamber pressure and experimental chamber pressure.

3.4 PROPELLANT COMBUSTION/DECOMPOSITION MODEL

The combustion/decomposition of bulk liquid propellant in CRAFT is modelled via a two-step process. In the first step, the bulk liquid is converted to an intermediate gaseous form which subsequently burns in the gaseous phase to generate the final products. The rate for both steps is specified in finite-rate Arrhenius form. The numerical values for the rate coefficients were obtained after performing one-dimensional numerical experiments to determine an appropriate rate of pressure rise. This temperature dependent combustion formulation has two implications from a physical viewpoint. The first observation we make is that the mixing between the hot plasma and the colder liquid controls the mixture temperature and consequently the overall rate for the first step of the decomposition process (e.g. this process is essentially diffusion-controlled). The second is that the temperature dependent decomposition rate allows us to prevent the existence of liquids at very high temperatures. The liquid is modeled to decompose at a finite rate when its temperature goes above the boiling point. As we discussed earlier, the actual process by which the bulk liquid combusts is extremely complex and involves both temperature dependent decomposition, as well as burning of droplets which are generated at the phases interface. The complex physics at this interface is not well understood, and quantitative data to model it from a more fundamental basis is not currently available. The approach we have followed is a credible approxima-

58

tion that attempts to incorporate the dominant effects of mixing between the hot plasma and the bulk liquid.

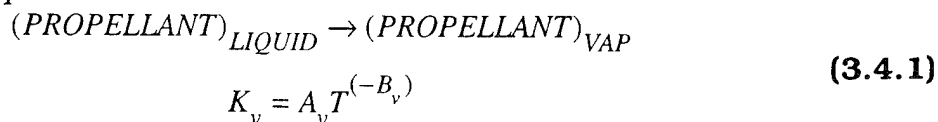For the ETC simulations to be discussed later in this section, a global four-component (n=4) formulation has been utilized comprised of:

1. Gaseous Plasma (ρ_1)
2. Gaseous Reactants (ρ_2)
3. Gaseous Products (ρ_3)
4. Bulk Liquid Propellant (ρ_4)

The plasma is inert and transfers energy to the working fluid via convective and conduction processes only. Radiative transfer has been neglected (for simplicity) although its contributions are felt to be significant by several investigators (see, e.g. the comments of Gillian, Ref. 71).

The finite-rate description of the decomposition and gas-phase combustion processes are as follows:

Decomposition:
$$(PROPELLANT)_{LIQUID} \rightarrow (PROPELLANT)_{VAP}$$
$$K_v = A_v T^{(-B_v)}$$
(3.4.1)

Combustion:
$$30\ (PROP)_{VAP} \rightarrow 10\ CO_2 + 14\ N_2 + 51\ H_2O$$
$$K_c = A_c T^{(-B_c)}$$
(3.4.2)
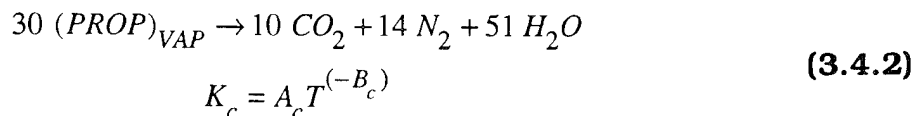
The specific rate constants utilized for our ETC gun predictions will be given in a later subsection.

3.5 FUNDAMENTAL STUDIES

In this section, we describe some fundamental studies to demonstrate the accuracy and range of application of the gas-liquid formulation in CRAFT. We begin by looking at shock propagation in high pressure (non-ideal) gases by computing shock tubes where the pressure ratio is constant but the mean pressure level increases. This is followed by a validation exercise for the gas-liquid formulation in which we compute a series of two-phase shock tube cases. The results of CRAFT are compared with the calculations performed by Coffee [68] using a different numerical methodology. Finally, to highlight the versatility of the gas-liquid formulation, we simulate the de-

formation and aerodynamic breakup of a cylindrical slug of bulk liquid by mixing with the surrounding air.

3.5.1 High-Pressure Gas Shock Tube Study

To illustrate the effect of high pressure compressibility in non-ideal gases [as represented by the virial equation of state, Eq. (3.1.9)], numerical shock tube studies were performed at varied pressures. Figure 3.5.1.1 exhibits a 10:1 pressure shock tube solution for three different pressure levels (10:1 atm, 100:10 atm, 1000:100 atm). The shock tube was taken to be of unit length and is plotted along the x-axis in Fig. 3.5.1.1, while the y-axis is the time scale. The pressure plots in Fig. 3.5.1.1 show the temporal evolution of the shock and expansion waves as they reflect off the ends of the shock tube. We note that at the lowest pressure levels (10:1 atm), non-ideal gas effects are negligible and the wave propagation is similar to that of an ideal gas. As the mean pressure increases, the non-ideal effects start becoming important and the acoustic speeds as well as shock propagation speeds go up. The increase in the propagation speeds is evidenced by the greater number of shock reflections for the highest pressure level case. Without the inclusion of the virial EOS, all these predictions would be the same, resulting in very significant errors for high pressures.

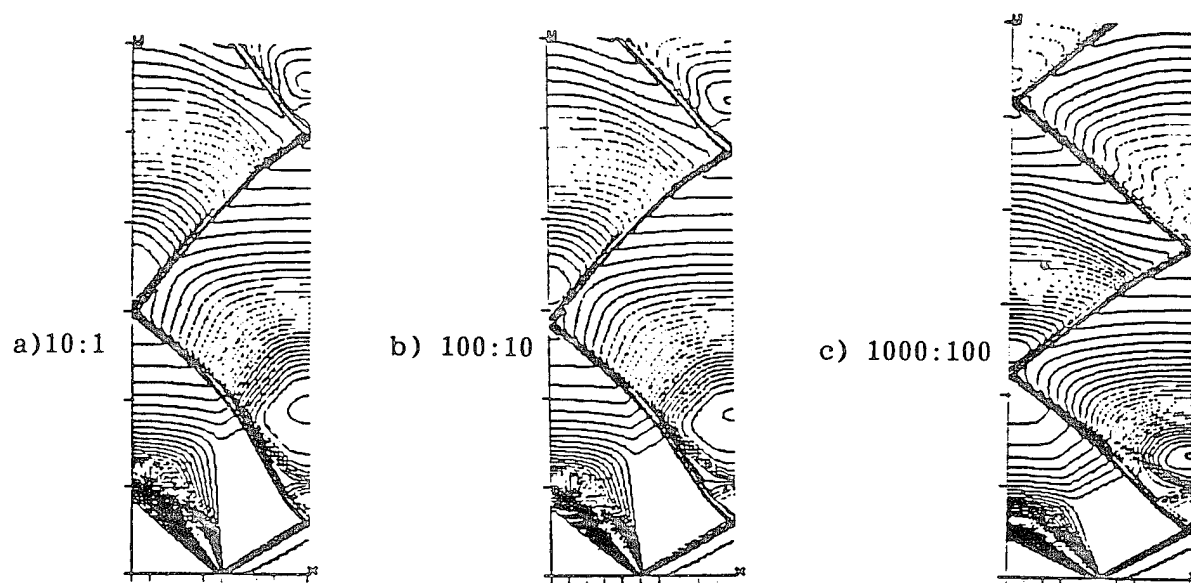

a)10:1   b) 100:10   c) 1000:100

Fig. 3.5.1.1. Shock tube studies with virial EOS: Pressure ratio across interface = 10.

3.5.2 Validation Studies for Two-Phase Shock Tubes

To validate the gas/liquid equilibrium formulation in CRAFT, a two-phase shock tube problem was chosen as a test case. The solutions computed by CRAFT were compared with those obtained by Coffee using a MacCormack algorithm based code [68]. Four cases were computed, all having pressure ratios of 2:1, with a high pressure of 100 MPa and a low pressure of 50 MPa. Table XI gives the details of each case.

Table XI. Gas/Liquid Test Cases
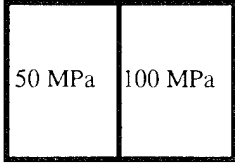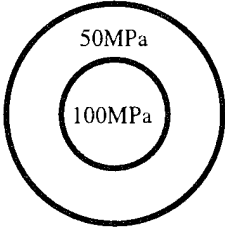
SOLUTIONS FOR TWO-PHASE 1-D SHOCK TUBES WERE
COMPARED WITH TERRY COFFEE'S COMPUTATIONS

CASE I: Liquid: high pressure side
Gas: low pressure side

CASE II: Liquid: low pressure side
Gas: high pressure side

CASE III: Uniform mixture of gas
and liquid on both sides

CASE IV: Radial shock tube –
uniform mixture with high
pressure at core

| 50 MPa | 100 MPa |

50MPa
100MPa

Figure 3.5.2.1 compares instantaneous snap-shots of the pressure profiles at 0.02 ms and 0.04 ms for Case 1. In this calculation, the high pressure side contains liquid and the low pressure side contains gas. Both the CRAFT upwind solution and the MacCormack central difference solution (with no added artificial dissipation) compute the correct shock amplitude and propagate both the shock and the rarefaction at similar speeds. The MacCormack solution, as expected, shows numerical oscillations around the shock front, while the upwind formulation, formulated to capture discontinuities, provides a smooth solution. The corresponding Case 2 solution with the gas on the high pressure side and the liquid on the low pressure side is shown in Fig. 3.5.2.2. The pressure profiles again compare quite well and provide confidence that the new upwind formulation is computing the correct solution for these two-phase flowfields.

6 1
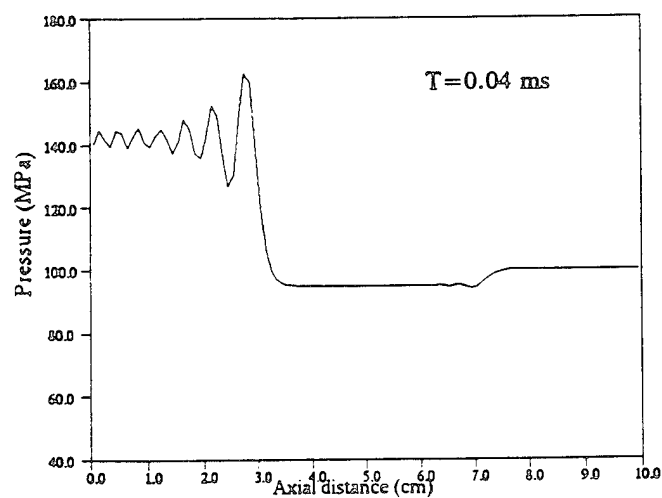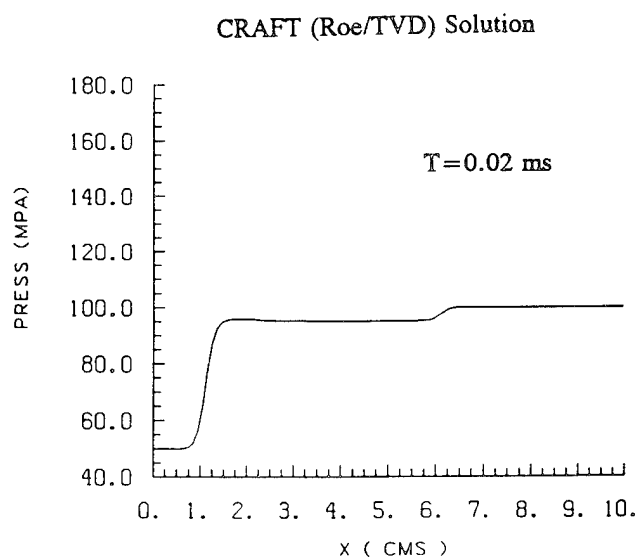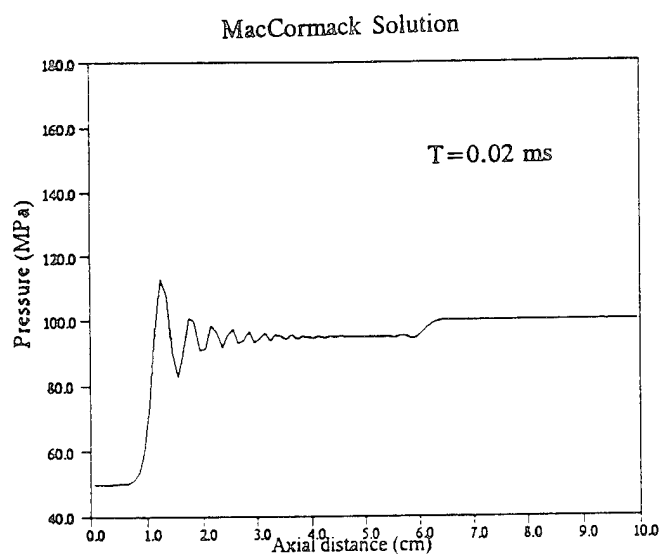
Fig. 3.5.2.1. Pressure profiles for a two-phase shock tube: gas = low pressure side and liquid = high pressure side.

MacCormack Solution   **CRAFT (Roe/TVD) Solution**

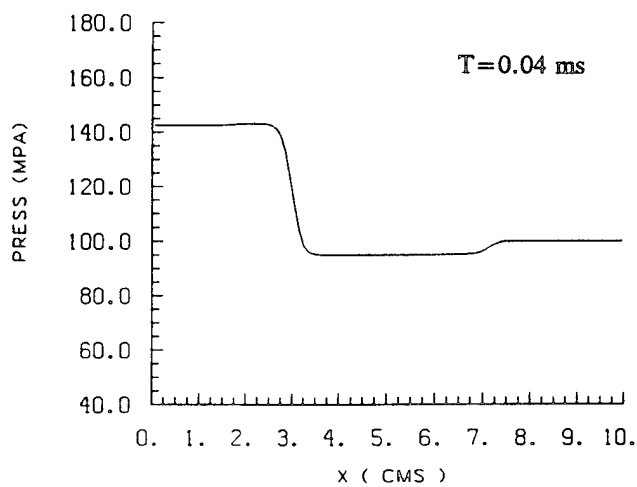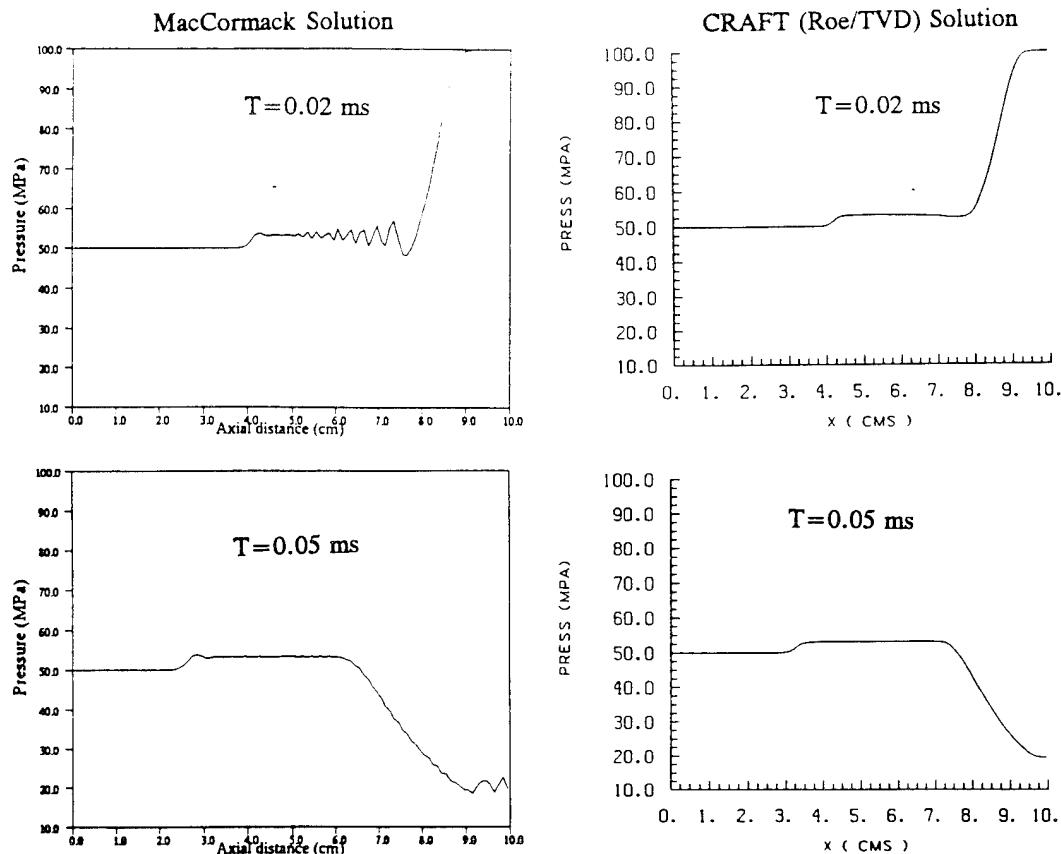**Fig. 3.5.2.2. Pressure profiles for a two-phase shock tube: gas = high pressure side and liquid = low pressure side.**

The next series of calculations (Cases 3 and 4) were performed for a uniform gas/liquid mixture where the volume fraction of the gas is 0.501. An axial shock tube case is simulated in Case 3, and the corresponding radial case for Case 4.   Figure 3.5.2.3 compares pressure profiles at 0.05 and 0.15 ms for the axial shock tube problem of Case 3.   The shock amplitudes agree very well. The wave propagation speeds which determine the location of the shock show minor differences at the larger time of 0.15 ms. This difference was found to be attributable to use of a virial equation of state (EOS) in the CRAFT upwind formulation, and a Noble-Abel EOS with a co-volume term in the Coffee/MacCormack procedure. The two EOS's give very similar results at lower pressures. However, at larger pressures, higher order virial terms have to be considered for the virial EOS to match the Noble-Abel EOS. For these test cases, only the first virial coefficients were specified and hence the acoustic wave speeds are somewhat different for the two formulations. The pressure histories at the two ends are shown in Fig. 3.5.2.4. The amplitude and the frequencies compare well taking into account the small differences in the acoustic speeds.
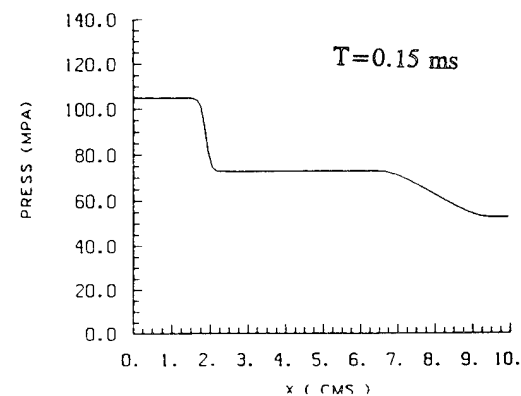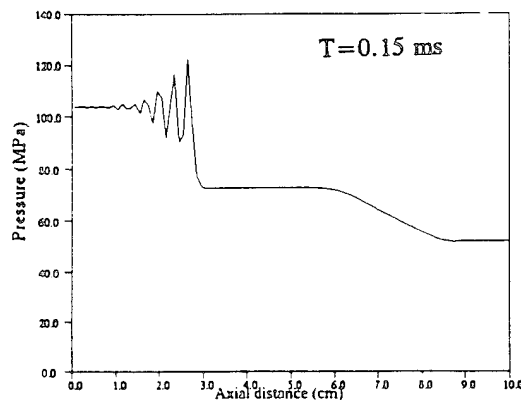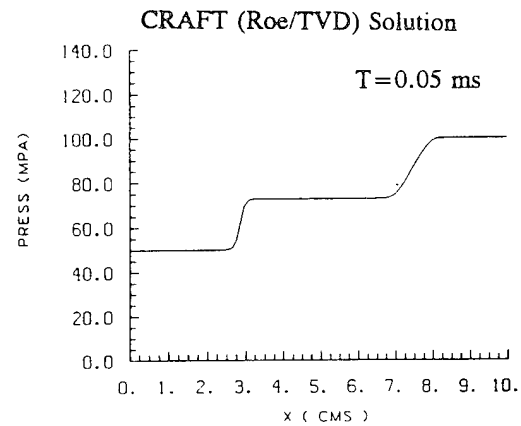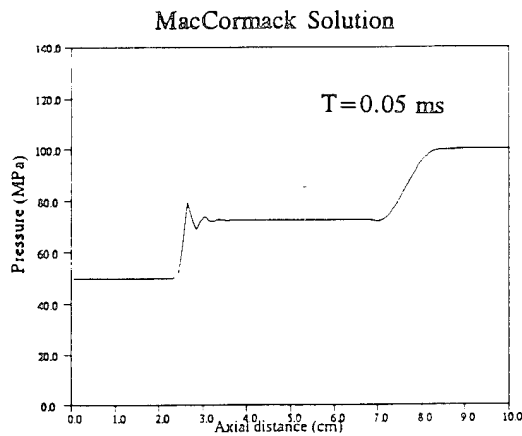
Fig. 3.5.2.3. Pressure profiles for a two-phase shock tube: Uniform gas/liquid mixture.

——————— Left Wall

- - - - - - - - Right Wall
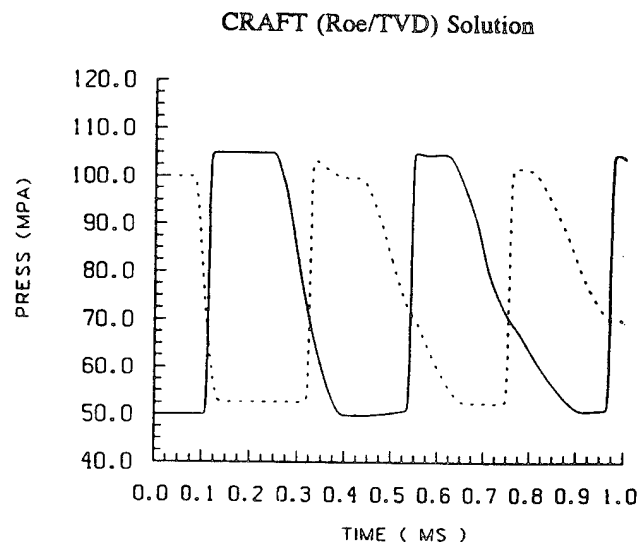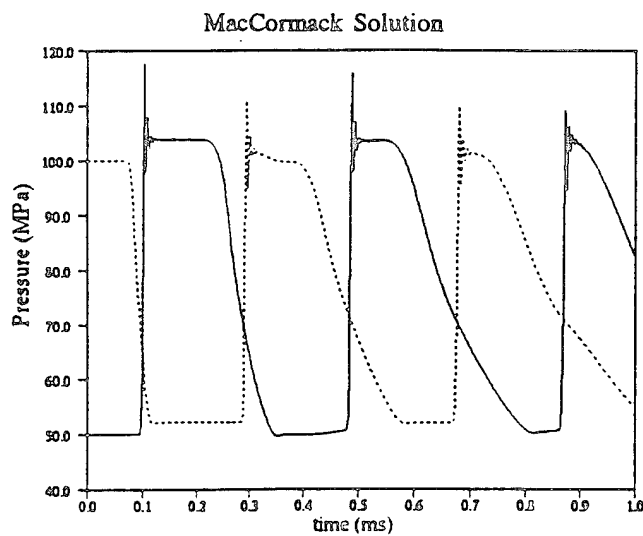
Fig. 3.5.2.4. Pressure history on wall of a two-phase shock tube: Uniform gas/liquid mixture.

64

The pressure oscillation comparisons in the Case 4 radial shock tube are shown in Fig. 3.5.2.5. As in Case 3, the fluid on both the high and low pressure sides is a uniform gas/liquid mixture. Unlike the axial case, the pressure waves in the radial shock tube problem have a strong amplification due to axisymmetric effects near the centerline. The pressure oscillations on both the centerline as well as the upper wall are exhibited. The oscillations do not attenuate significantly in the duration of the calcultion. A periodic limit-cycle with a pressure amplitude of 30-40 MPa is generated at larger times.
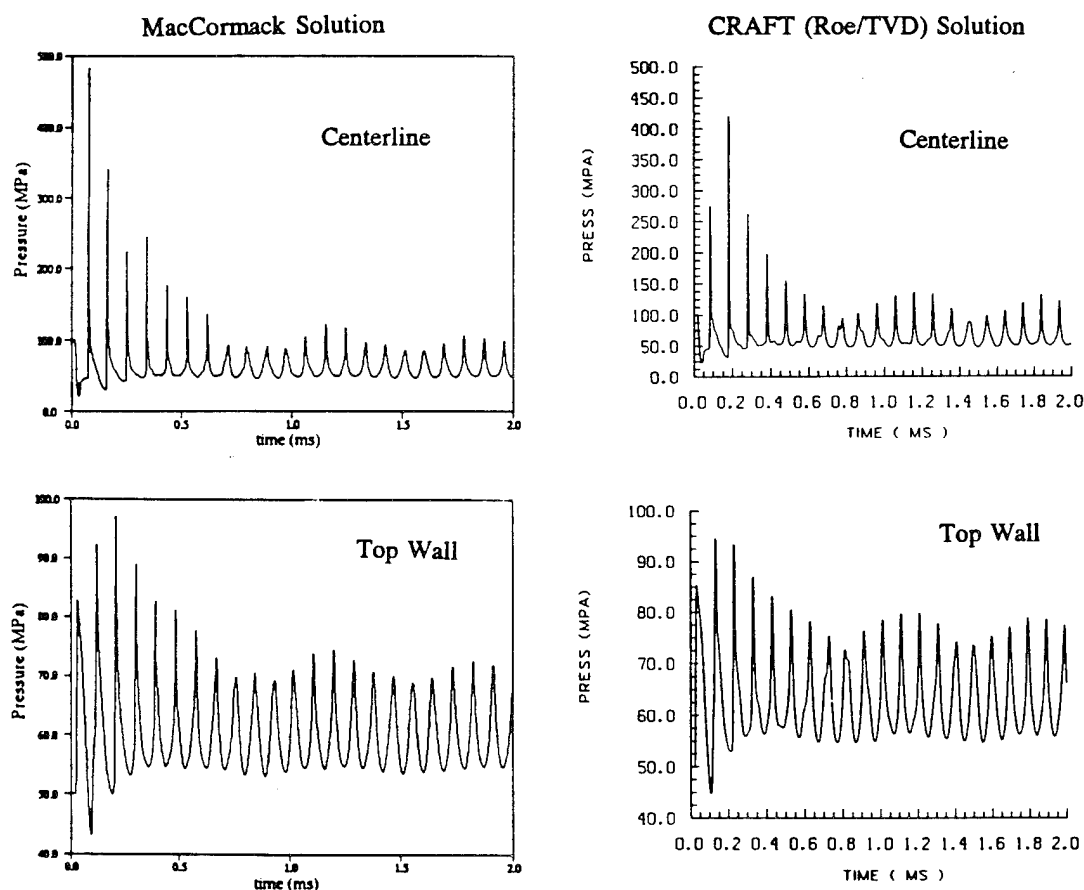
Fig. 3.5.2.5. Pressure history for a radial two-phase shock tube: Uniform gas/liquid mixture.

Figure 3.5.2.6 shows the spectral analysis of the limit-cycle at both the centerline and the upper wall. Both the MacCormack scheme and the CRAFT upwind procedure predict a fundamental frequency of approximately 10.5 Hz. However, differences exist within the details of the two spectra. At both the centerline and the upper wall, the upwind solution shows a higher percentage of energy to be in the fundamental tone, while the

MacCormack solution shows more energy in the higher overtones. Furthermore, the drop-off in the magnitude from the centerline to the upper wall is much larger in the upwind solution when compared to the drop-off in the spectra of the MacCormack solution. Comparisons of Roe/TVD and MacCormack numerics for acoustic boundary layers in a solid propellant rocket motor also show comparable differences (see Ref. 72).
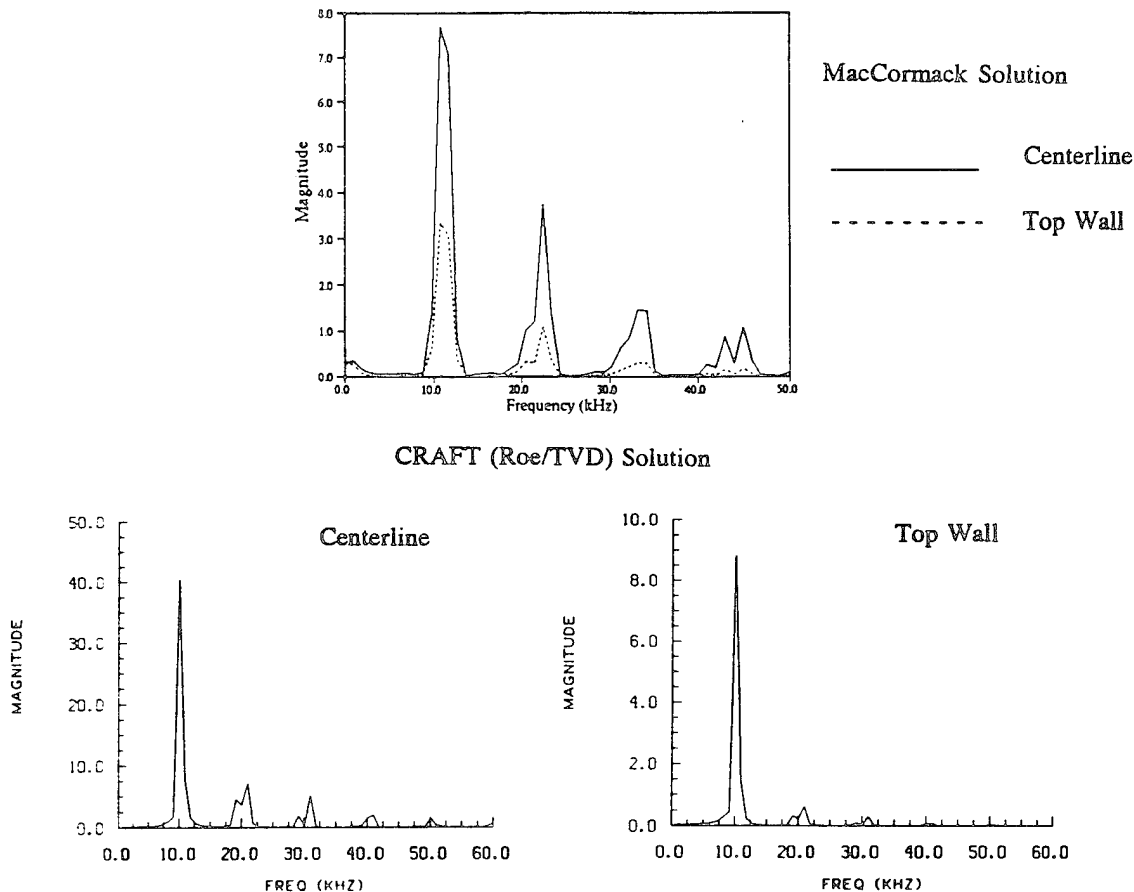
Fig. 3.5.2.6. Frequency spectra for a radial two-phase shock tube: Uniform gas/liquid mixture.

3.5.3 Bulk Liquid Breakup

Another problem of fundamental interest which can be studied with the gas-liquid equilibrium formulation is the deformation and aerodynamic breakup of bulk liquid. Experimental studies have recently been performed [73] with fly-out of bulk liquid to provide an understanding of aerodynamic mechanisms. The liquid fly-out problem is of present interest in the scenario of a threat missile carrying noxious bulk liquid releasing it after being "hit.". Here the droplet formation mechanism and the dispersion of the

66

droplet cloud is of critical interest to the defense community. In the experimental studies, a cylindrical pellet of liquid flying at high speeds is impulsively introduced into stagnant air. The problem of interest is how the bulk liquid pellet interacts with the air surrounding it, deforming and eventually having droplets being stripped-off from the interface between the air and the liquid. This problem directly relates to instabilities at the gas/liquid interface in ETC/LP and LPG problems where bulk liquid interacts with gas and generates droplets.

The schematic of the problem being studied is shown in Fig. 3.5.3.1. A cylindrical pellet of liquid having a diameter of 50 cm and a length of 50 cm is impulsively given a velocity of 700 m/s. The flow around this liquid cylinder is computed using a dynamic grid which translates at the instantaneous velocity of the grid point initially located at the liquid center-of-mass. The location and shape of the liquid mass is displayed in time by plotting the liquid mass fraction contours, while the flowfield around and within the liquid mass is displayed by plotting the pressure contours in the flowfield.
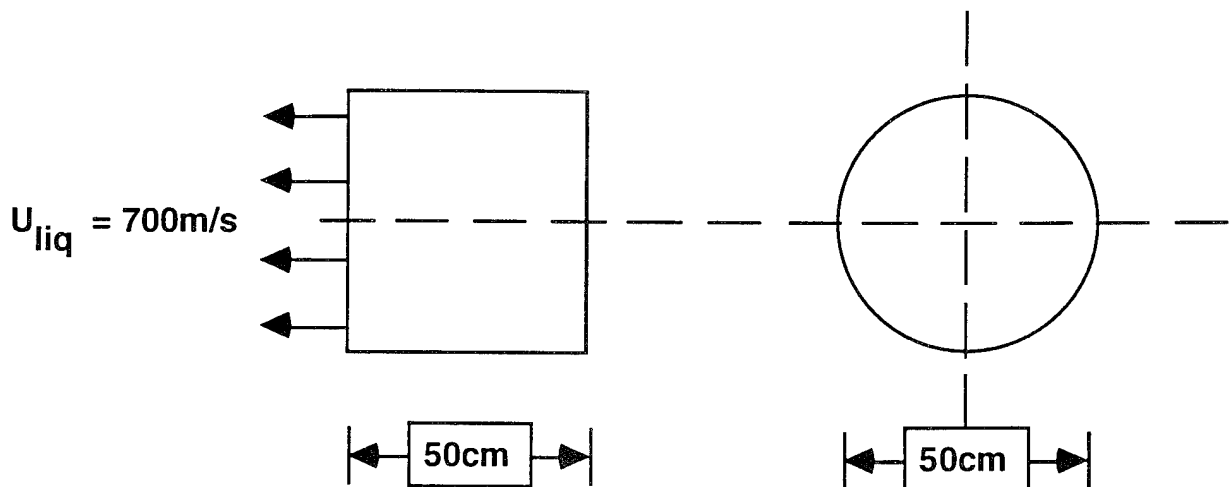
Fig. 3.5.3.1. Flowfield initialization: Flyout problem.

In Figures 3.5.3.2a-3.5.3.2d we plot the liquid mass fraction and pressure contours at the following four times: 1, 2, 3, and 4 ms. Figure 3.5.3.2a shows the flowfield at 1 ms. At 1 ms the original cylindrical shape (shown as black box) begins to show deformation at both the leading edge and the trailing edge. At the leading edge, the liquid gets compressed while in the rear the liquid at the corners gets stretched out in the form of fingers. The

a) 1ms
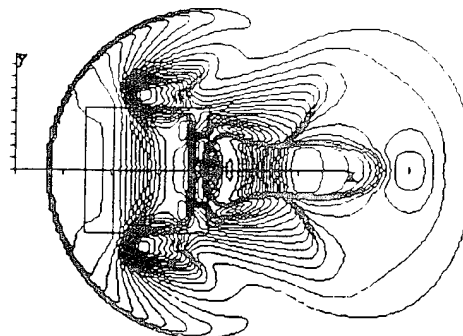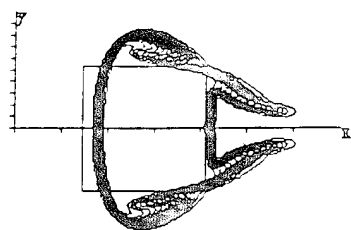
b) 2ms
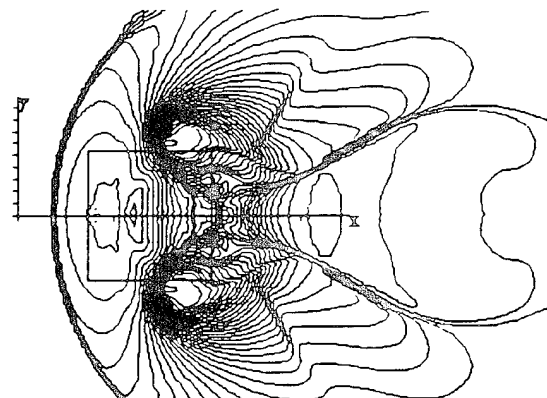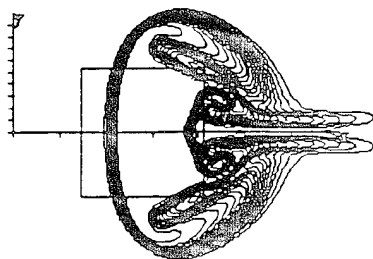
c) 3ms
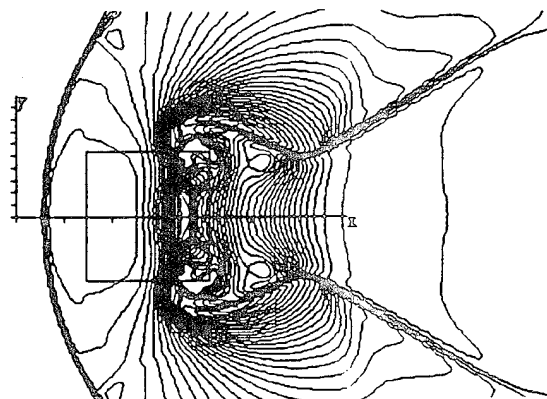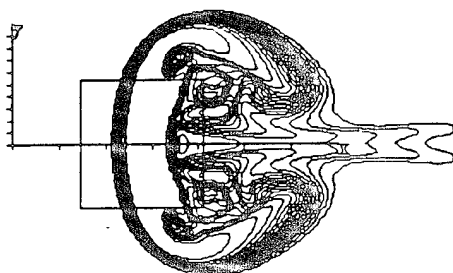
d) 4ms
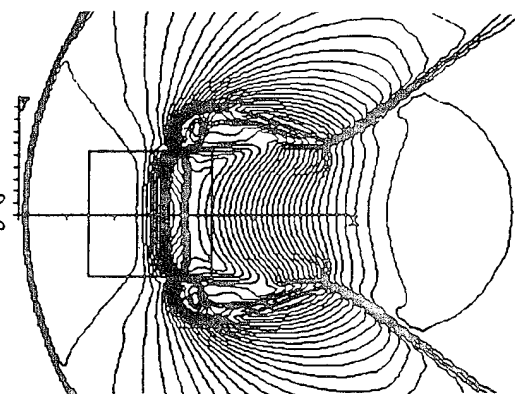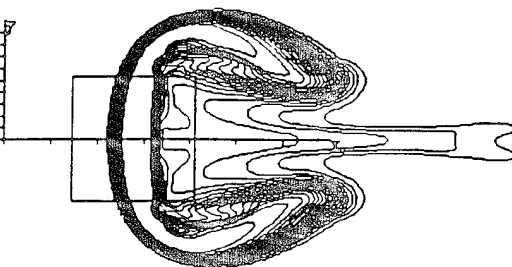
Liquid Mass Fraction   Log Pressure

Fig. 3.5.3.2. Liquid flyout problem: Contours of liquid mass fraction and
pressure plotted at 4 different times: a) 1ms; b) 2ms;
c)3ms; and d) 4ms.

68

pressure contours at 1 ms show the classic features of a blunt body flow, except that the blunt body here is a compressible liquid which absorbs part of the shock. A classical bow shock is formed in front of the liquid, and a wake with a neck shock is formed behind the liquid. At 2 ms (Fig. 3.5.3.2b), the front end of the liquid continues to get compressed and pushed out. The rear portion of the liquid shows vortical liquid roll up with the gas. The pressure field shows that the bow shock continues to move out, while the plume expands out further behind the liquid. By 4ms, the liquid compression results in two large fingers of liquid being pulled out at the top and bottom surface with a central column of liquid being compressed further. The overall deceleration of the bulk liquid is determined in the course of the calculation as exhibited in Figure 3.5.3.3. The liquid slows down from 700 m/s to 250 m/s in the 4ms of this prediction.
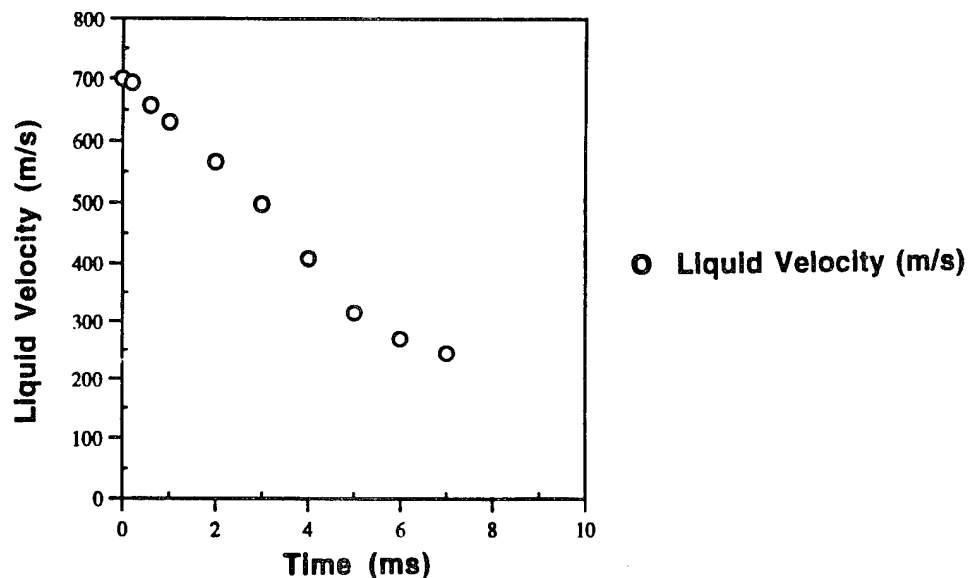
Fig. 3.5.3.3. Velocity history of bulk liquid.

The above calculations highlight the ability of the CRAFT code to capture vortical roll-ups and large-scale turbulent structures which produce mixing between phases in transient multi-phase flows. To take the problem of gas-liquid mixing to completion, the code would either have to resolve very fine scales (micron level), or, would have to be coupled to a droplet generation model. When droplets are generated, the flowfield would consist of a gas-bulk liquid continuum fluid with a dispersed phase consisting of droplets. As we will describe in Section 6, our work in solid propellant ETC

(to discretely track the solid propellant particles) has yielded methodology to handle such liquid flows using a Lagrangian solution procedure to track the droplets. The missing link in developing a unified code to solve for liquid breakup is the inclusion of a dynamic droplet generation correlation. Such correlation work is presently under development in the threat missile defense community and should have significant relevance to liquid propellant gun simulation.

4.0 SIMULATIONS OF ETC/LP FIRING

In this section, we describe simulations for 30 mm liquid propellant ETC guns using the gas-liquid equilibrium formulation described in the earlier section. We begin with a description of the problem set-up, then discuss the simulation of Shot 17 fired by FMC. In the final section, we address unsteady turbulence issues in transient flows that we have encountered and dealt with in our ETC/LP simulations.

4.1 PROBLEM SETUP

The gun geometry chosen for study is a 30 mm ullage tube configuration which was fired at FMC and is denoted as "Shot 17." Figure 4.1.1 shows a schematic of the gun chamber which has a total volume of 167 cc (length is approximately 20.9 cm, and radius is approximately 1.59 cm). Initially, the plasma occupies the center-core ullage tube which has a volume of 19 cc and extends the entire length of the chamber. The center-core is assumed to burst uniformly along its entire length when the plasma contained within attains a critical value of pressure and temperature. The burst pressure and temperature of the plasma are specified to be 112 MPa and 15067 K, respectively. These conditions were obtained from calculations performed by Powell using his one-dimensional model [70].
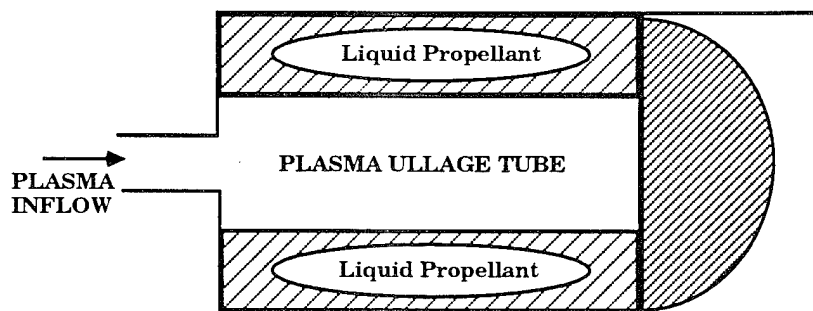
Propellant		Plasma	
Initial Volume:	148 cc	Initial Volume:	19cc
Mass:	201 gm	Burst Pressure	112 MPa
		Burst Temperature:	15067 K
	Mass of Projectile:	339 gm	

Fig. 4.1.1. FMC Shot 17 ullage tube geometry and specifications.

7 1

The propellant employed for the Shot 17 firing is a 13.4 Molar gelled solution of HAN/Hydrocarbon. The total mass of the propellant is 201 gm and it occupies a volume of 148 cc. As we described in Section .3.4, a two-step combustion model is utilized in CRAFT. The liquid propellant decomposes to a gaseous state and then combusts to form the final products. The details of this two-step combustion process and the respective rates for the finite-rate Arrhenius form are given in Eqs. (3.4.1) and (3.4.2). The numerical values for the rate coefficients were obtained after performing one-dimensional numerical experiments to determine an appropriate rate of pressure rise. The values utilized in these equations are:

Decomposition:
$$A_v = 6.25 \times 10^5 \qquad B_v = -4000.0$$

Combustion:
$$A_c = 1.25 \times 10^6 \qquad B_c = -4000.0$$

The units of A and B are chosen such that K_v and K_c have units of cc/(mole-sec).

4.2 DISCUSSION OF SIMULATION

The results from our simulation of the 30 mm shot are compared with the experimental measurements obtained by FMC. As we shall discuss in greater detail in the following section, the transient nature of the flow and the mixing generated by the injection of high pressure plasma are expected to generate large vortical, turbulent structures. These large scale structures are captured by the numerics of the CRAFT code. Hence, we utilize the LES methodology in representing the turbulence which was outlined in Section 2, wherein only the small scale dissipative turbulence is modelled. For the calculation described in this section, an algebraic eddy-viscosity SGS model with constant length scale was first employed to model the effects of the small scale turbulence. The constant length scale was taken to be 1 percent of the radius of the chamber. Additional sensitivity studies with sub-grid turbulence levels and other related issues are described in the next section. In the following paragraphs, we discuss and compare our baseline computation with the experimental results.

The measured and computed pressure-time history on the chamber wall at position A (3.25 cm from breech) is shown in Fig. 4.2.1. On comparing the experimental data with the numerical pressure curve, we observe that the initial pressure history and the peak pressure value is reproduced closely by the computations. The experimental and numerical peak pressure value is approximately 290 MPa. However, the experimental peak is attained at a time of 1.5 ms while the simulation predicts the peak to be at 2.0 ms. The qualitative nature of the peak is represented well by the computations. The data shows a flat pressure peak; the peak value is maintained for about 0.5 ms. The computed peak also has a flat top for approximately the same time period.
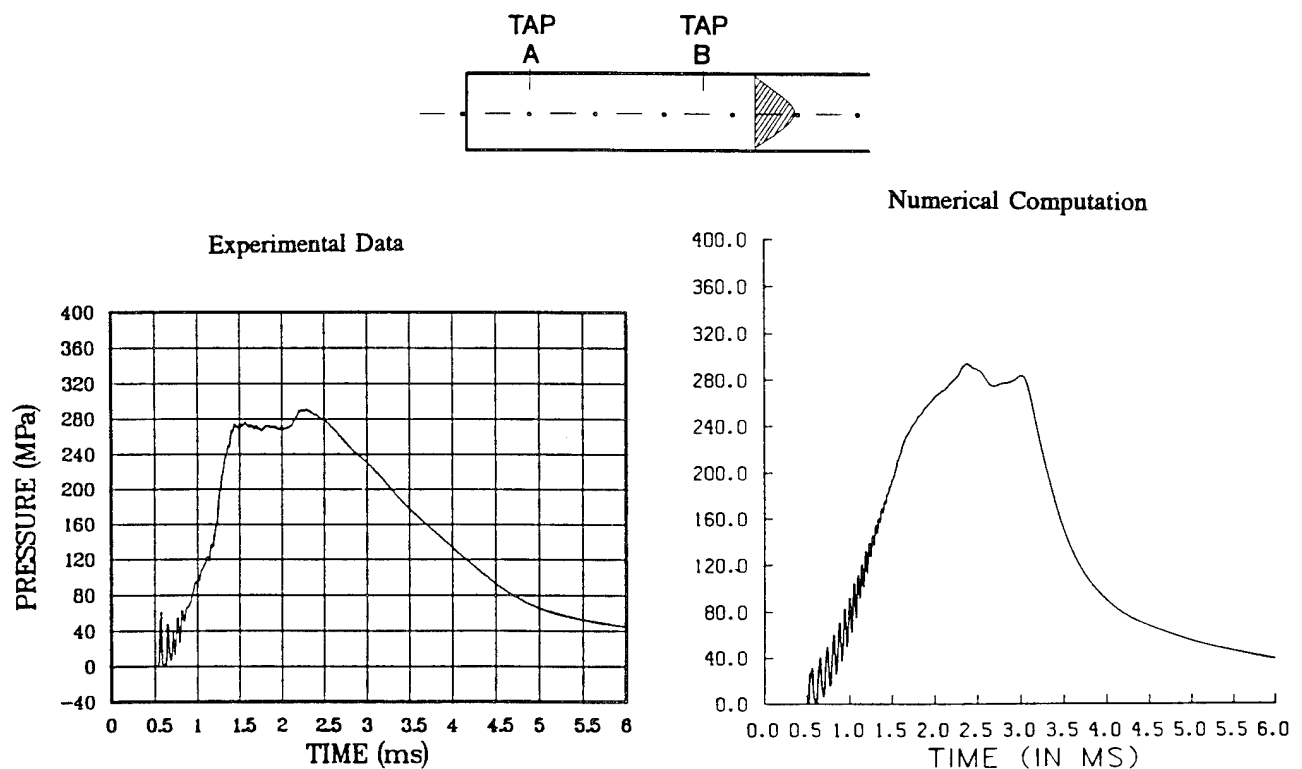
Fig. 4.2.1. Pressure history at Tap A: Experimental data vs numerical computation for FMC Shot 17.

After the pressure peaks, the velocity of the projectile continues to increase until it equilibrates. Correspondingly, the pressure drops to its equilibrium value. The numerically computed equilibrium pressure level is around 40 MPa which compares well with the experimental equilibrium pressure level. However, the rate of drop in the pressure is more rapid in the computations than that observed experimentally. The reason for the

faster drop in computed pressure is not fully understood. One possibility is that the virial coefficients of the gaseous combustion product mixture has to be better represented at these high pressure and temperature levels.

The pressure history computed at Location B (17.5 cm from breech) is shown in Figure 4.2.2 along with the experimental data. The general observations made earlier for Location A hold here as well; the pressure peak values as well as the time scales match well with the data. The experimental peak shown here was obtained at an azimuthal angle of 90 degrees. This curve differs from that obtained at an azimuthal angle of 0 degrees which has multiple peaks. The experimental data reveals significant 3-D effects which may be attributed to the possibility that the plasma tube did not rupture uniformly.
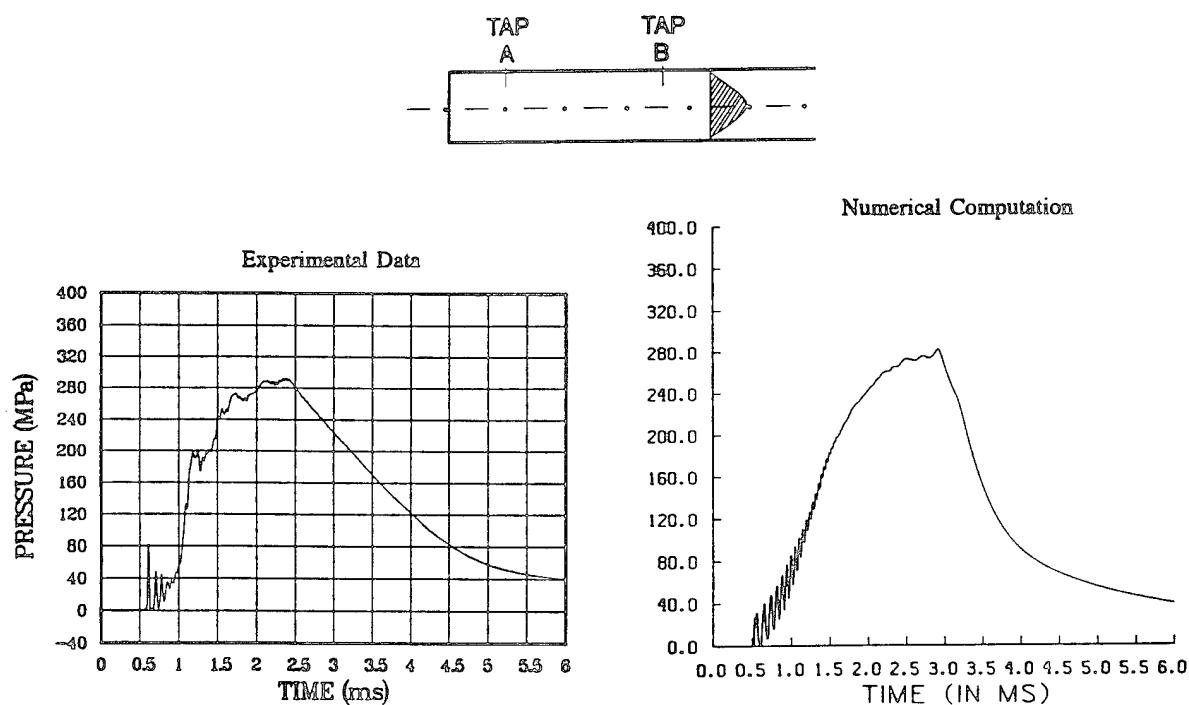
Fig. 4.2.2. Pressure history at Tap B: Experimental data vs numerical computation for FMC Shot 17.

The velocity and displacement of the projectile are shown in Fig. 4.2.3. A shot-start pressure of 20 MPa was specified which prevents the projectile from moving until 0.55 ms. Once the projectile overcomes the shot-start, the velocity becomes proportional to the integral of the pressure curve. Hence, the velocity rises exponentially as the pressure peaks and then even-

74

tually equilibrates to a value of approximately 1400 m/s. Over the time interval of the computation, the projectile travels a distance of approximately 450 cm.

(a) VELOCITY OF PROJECTILE

(b) DISPLACEMENT OF PROJECTILE
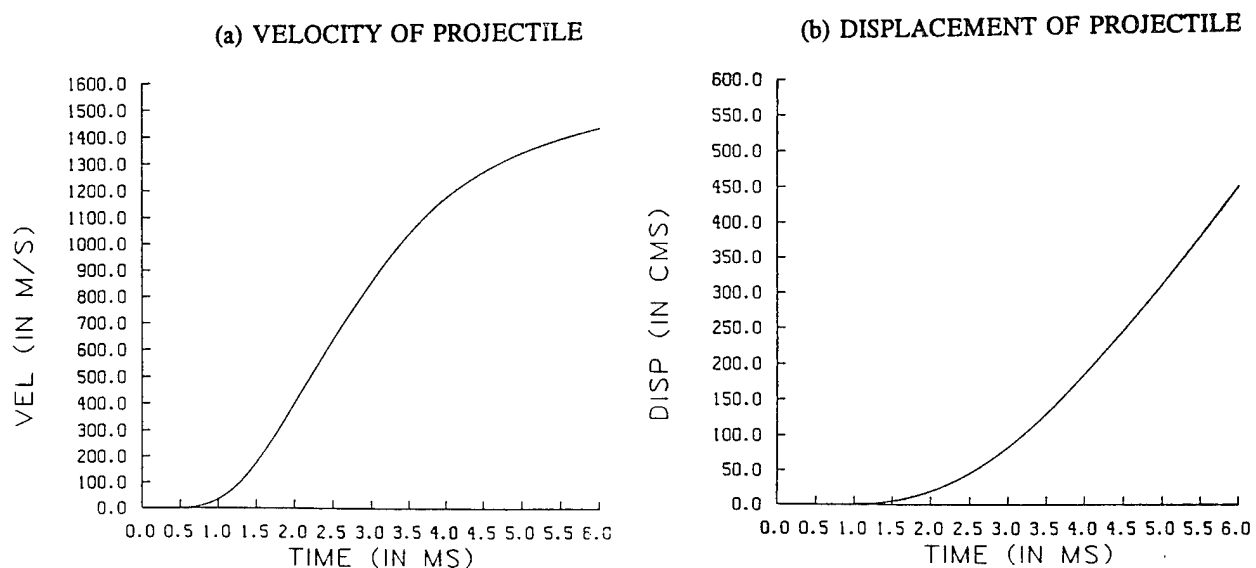
Fig. 4.2.3. Numerical predictions for projectile velocity (a) and displacement (b).

4.3   UNSTEADY TURBULENCE ISSUES

As referred to earlier, the flowfield within the ETC flowfield is expected to exhibit large scale vortical structures. In the center ullage problem, vorticity will be produced by the projectile and enhanced combustion should occur in the projectile wake region. Consider product mass fraction contours in the chamber (Fig. 4.3.1) at three different times, which are good markers for mixing effects because product generation increases in regions where the hot plasma mixes effectively with the liquid propellant. In Fig. 4.3.1, the blue colors at the top and bottom of the chamber denote very low product concentrations in the liquid propellant. As we proceed towards the core, the product concentration increases sharply across the interface layer where the plasma/products are mixing with the liquid.   Notice the enhanced mixing in the projectile wake region. To highlight the enhanced generation of products in vortical regions, we plot instantaneous contours of mass fraction in the interval 1.395-1.495 (Fig. 4.3.2) at intervals of 20 μs. As Fig. 4.3.2 indicates, the product generation appears to predominantly occur in the vortical roll-ups where the plasma and product are mixing the fastest.
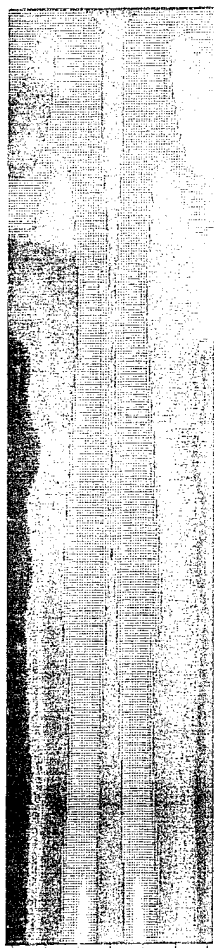
75
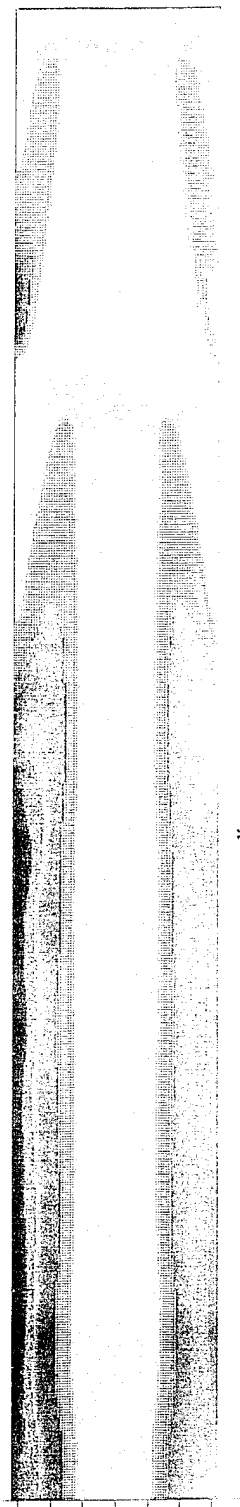
Fig. 4.3.1. Product mass fraction contours at three different times for FMC Shot 17 Simulation: 1.75, 2.00, and 2.25ms.
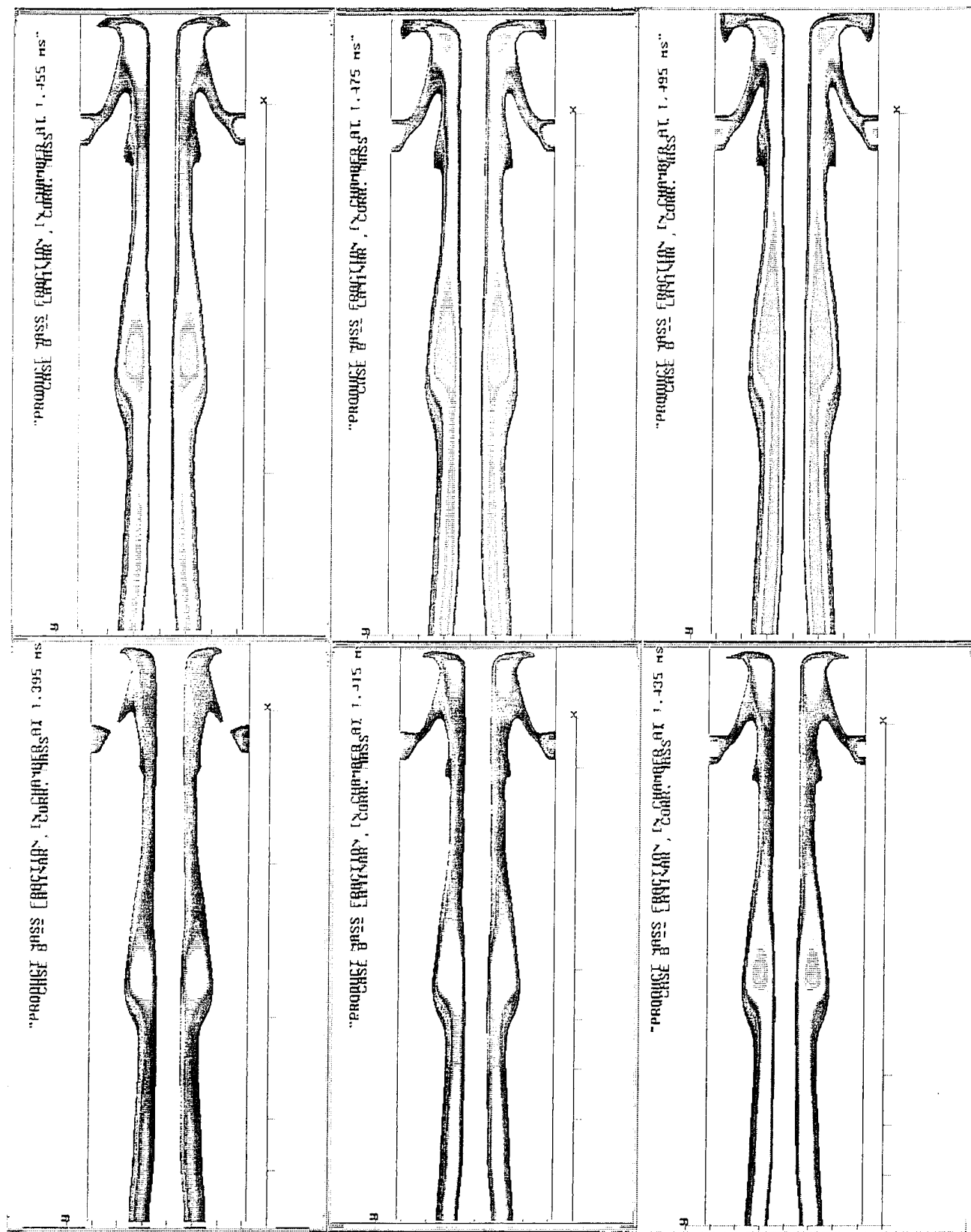
Fig. 4.3.2. Contours of combustion product mass fraction plotted at intervals of 20μs beginning at 1.395ms.

The large vortical structures evidenced in Fig. 4.3.2 contain the large-scale component of the flow turbulence. To illustrate this, we process instantaneous velocity data in projectile fixed coordinates for the time period 0.95-1.4 ms. From the instantaneous velocity values, we compute the rms value of the fluctuating velocity component at various axial locations. In Figs. 4.3.3 and 4.3.4 we plot the radial variation of the rms Reynolds and Favre averaged fluctuations at positions 4 cm and 17.5 cm upstream of the
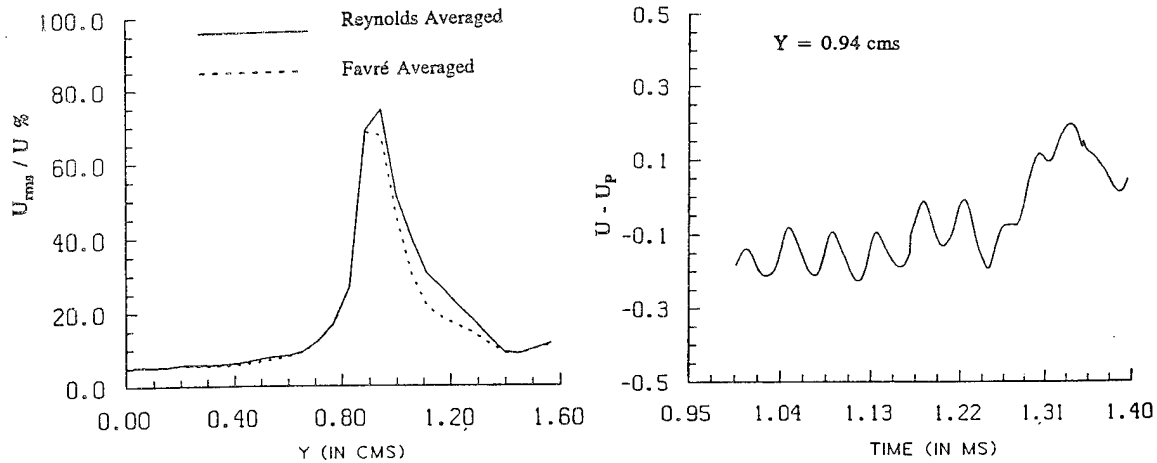
(a) Radial Variation of U_{rms}

(b) Instantaneous Axial Velocity at y = 0.94 cms

Fig. 4.3.3. Turbulence characteristics in ullage tube 4.0cm from projectile base: a) radial variation of U_{rms}; b) instantaneous axial velocity at y=0.94cm.
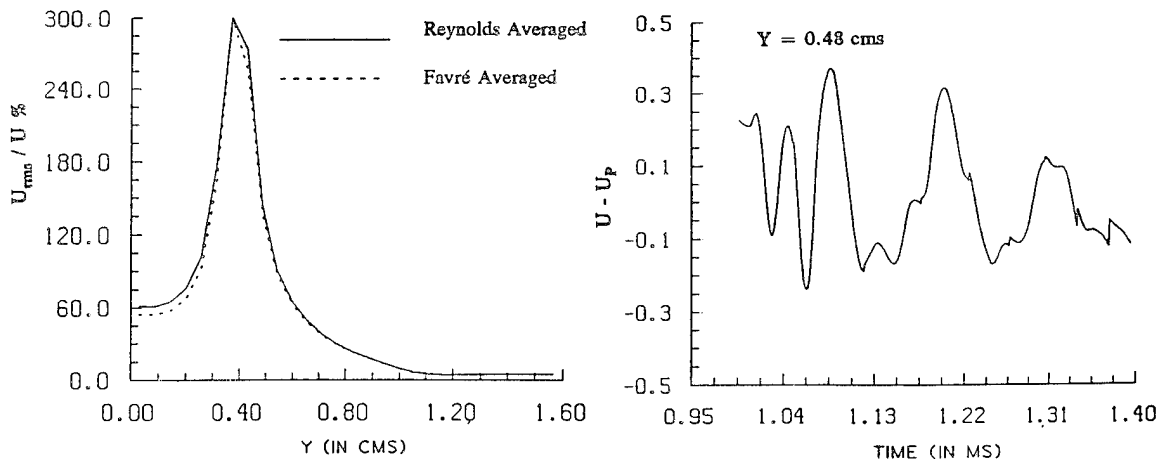
(a) Radial Variation of U_{rms}

(b) Instantaneous Axial Velocity at y = 0.48 cms

Fig. 4.3.4. Turbulence characteristics in ullage tube 17.5cm from projectile base: a) radial variation of U_{rms}; b) instantaneous axial velocity at y=0.48cm.

projectile. The U_{rms} peak at the position closer to the projectile (x_p – x=4cm) is closer to the top of the chamber (y=0.9), while it is closer to the core (y=0.4) as we go further away from the projectile (x_p ÷ x = 17.5 cm). These observations are consistent with the vortex structures evidenced in Fig. 4.3.2. Closer to the projectile, we see a vortex roll-up extending to the top of the chamber, while at the breech end the vortex structures are limited to the interface shear layer.

Having identified that large scale turbulent structures play a dominant role in the combustion process, we now perform numerical experiments to determine the sensitivity of the pressure curve to the subgrid turbulence levels as well as to kinetic rates. We repeated this calculation with rates which are twenty percent larger than the baseline rates using two different subgrid models. Faster rates were used because the pressure rise in the baseline case was slower than observed in the data. The first subgrid turbulence model used was the same as the baseline case: the length scale is one percent of the radius of the chamber. The second subgrid turbulence model employed is the Smagorinsky formulation with C_s = .1. We designate the baseline case as Case 1 and the case with increased rates and the same fixed length scale, as Case 2. Variants of Case 2 include the Smagorinsky SGS model (where the length scale expands with the grid) and a second variant with no SGS model.

The pressure history for Case 2 is plotted in Figures 4.3.5a (x=3.25cm) and 4.3.5b (x=17.5cm). The solid line corresponds to the fixed length scale as in the baseline case, while the dashed line corresponds to the Smagorinsky subgrid model with a variable grid/size linked length scale. The first observation we make is that because the burning rate is faster, the pressure rises faster than the baseline case and reaches a value of 290 MPa by 1.5 ms as in the experimental data. However, having reached this value, the pressure does not flatten out but instead rises to a higher level. The second observation is that the results with the two different subgrid turbulence models are very similar. The pressure history for the variable length scale (dashed line) flattens out a little more than the fixed length scale (solid line) but does not flatten out enough to prevent the pressure from overshooting the peak value of 290 MPa. The shape of the pressure curve using no subgrid scale model is compared to that with a subgrid model in Figure 4.3.6 (both cases have the same burn rates). Without the subgrid

79

model, the observed "flattening" does not occur. These results are a preliminary effort to assess the sensitivity of the pressure curve to various parameters. Further studies on grid sensitivity are planned and we intend to implement more advanced LES models in future work.
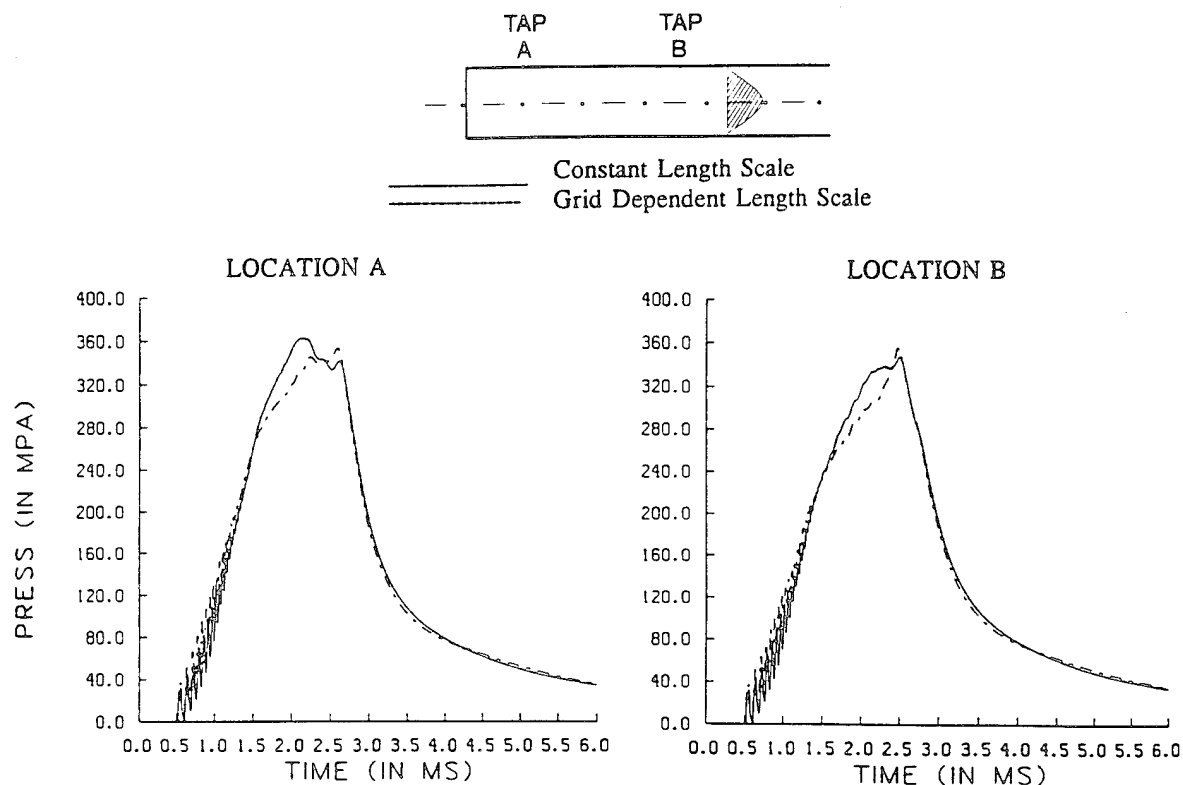
Fig. 4.3.5. Sensitivity of pressure history to burn rates and subgrid turbulence.
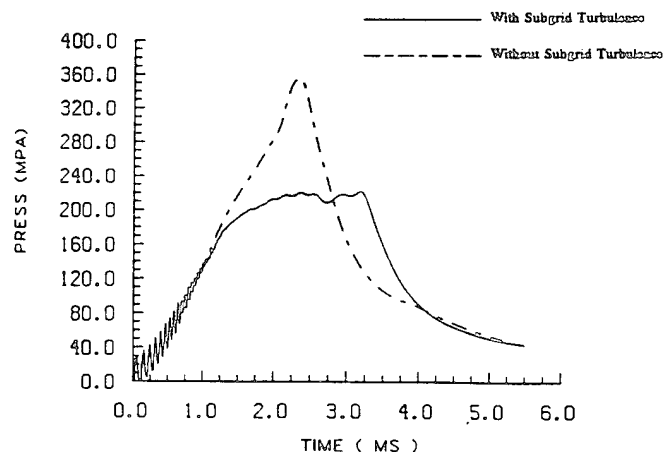
Fig. 4.3.6. Comparison of pressure history with and without subgrid turbulence.

5.0 CRAFT CODE EXTENSIONS FOR PRELIMINARY ETC/SP SIMULATIONS

In this section, we describe simulations of solid-propellant ETC configurations which were modelled using a preliminary fixed-bed formulation. We begin by describing the features of the ETC/SP designfollowed by a discussion of the fixed bed formulation. Simulations for two shots fired by GDLS are discussed and compared with experimental measurements.

5.1 FEATURES OF THE PROBLEM

The solid propellant ETC gun considered in our study had a center-core ullage tube configuration similar to the ETC/LP design. A schematic of the 30 mm ETC/SP gun analyzed is shown in Fig. 5.1.1. As in the ETC/LP case, the gun chamber has an ullage tube containing plasma which bursts.
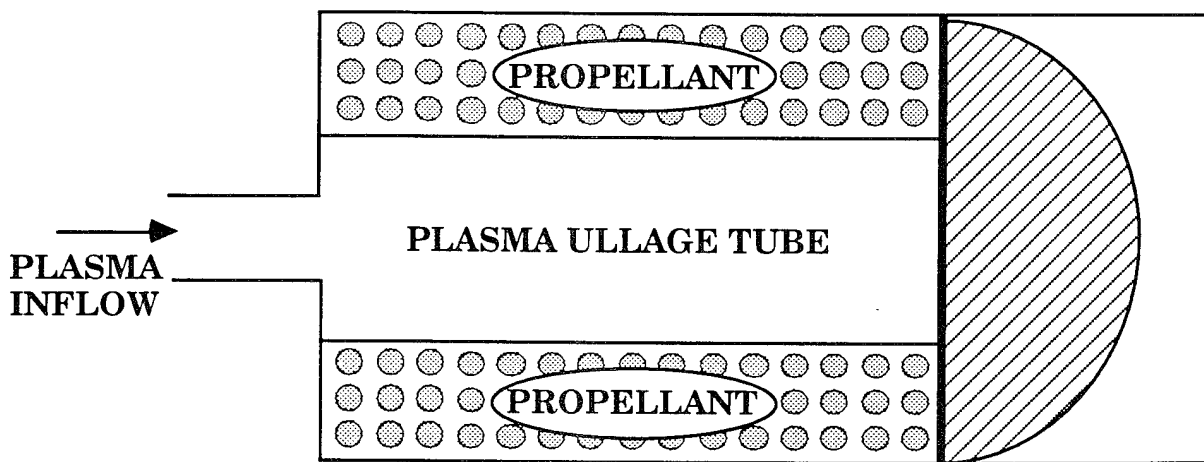
Fig. 5.1.1. Schematic of solid propellant ETC gun system.

For the ETC/SP case, the propellant is formed of spherical balls whose initial diameter is approximately 1,000μm. Loading densities are high and the gas porosity is of the order of 0.4. To operate with these high loading densities, the propellant balls are deterred chemically. This involves diffusing a chemical deterrent into the balls such that burn rate increases with increasing depth from the surface until the undeterred, energetic propellant is reached. A typical radial variation of the deterrent profile, which is shown in Fig. 5.1.2, indicates that the properties of the propellant are a strong function of the ball diameter. Simulation of the solid propellant ETC configuration requires the detailed modelling of each propellant ball as well as the inter-phase, non-equilibrium processes within the propellant bed.
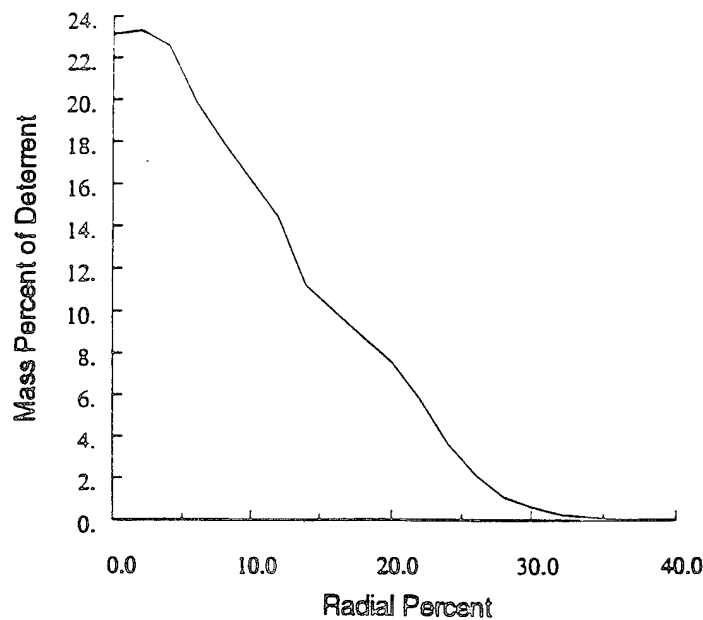
Fig. 5.1.2. Representative variation of deterrent concentration as a function of depth from the surface of the ball propellant.

5.2 FIXED-BED FORMULATION

As a first step in the implementation of the two-phase, nonequilibrium formulation, preliminary computations were performed assuming the propellant bed remains fixed. The fixed bed assumption eliminates uncertainty associated with propellant bed deconsolidation and subsequent fluidization. The propellant bed boundary is instead treated as a regressing internal boundary through which combustion products enter into the gas core (akin to traditional treatment of ablative surfaces). The initial volume of the propellant bed corresponds to the solid volume of the propellant, while the ullage volume of the propellant is added to the gas core. This is done so that the plasma being pumped in has additional volume for pressure relief, and it crudely approximates the expansion of plasma within the propellant bed.

The numerical methodology of the fixed bed formulation is illustrated in Tables XII and XIII. The propellant bed is divided into a number of axial cells and the diameter of propellant balls in each cell is tracked in time as the balls combust with a burn rate responding to the pressure in the gas core at the propellant bed interface. As the balls burn the bed regresses and the combustion products are injected into the gas core. The regression of the bed is assumed to be only in the radial direction i.e. the axial dimension of the propellant cell remains unchanged with the net volume change being obtained by the radial movement of the propellant boundary.

82

Table XII. Coupling of Solid Propellant Burn Model Into CRAFT
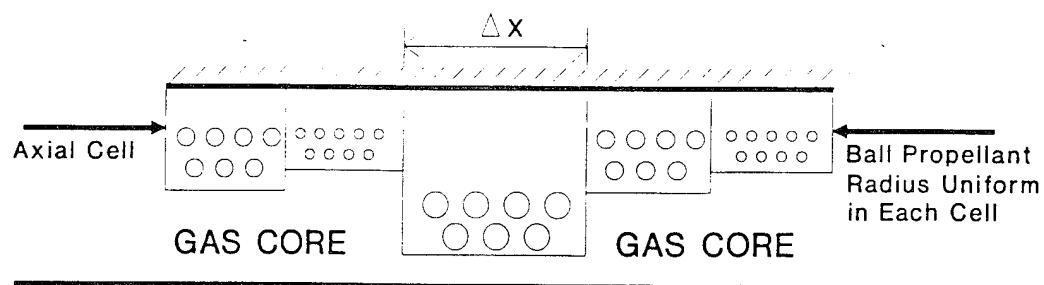
- BURNING RATE FUNCTION OF LOCAL SURFACE PRESSURE

- GASEOUS PRODUCTS MASS AND ENERGY FLUXES FROM SOLID PROPELLANT SERVE AS BOUNDARY CONDITIONS

- DYNAMIC MOTION OF RECESSING SOLID PROPELLANT ACCOUNTED FOR

Table XIII. Preliminary Solid Propellant Burn Model
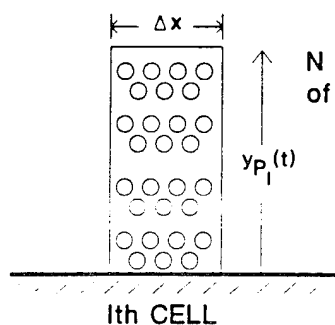
- FIXED-BED ASSUMPTION

- ALL BALLS IN EACH CELL BURN AT SAME RATE

- $r_P(t)$ TRACKED IN EACH CELL

- PRESSURE DEPENDENT BURN RATE — EXTERNAL SURFACE PRESSURE UTILIZED WHICH VARIES AXIALLY

MASS OF PROPELLANT IN CELL $= M_P = \dfrac{4}{3}\pi r_p^3 \times \rho_p \times N$

RADIUS CHANGE: $\quad r_p \rightarrow r_p - (\dot{r})\,\Delta t \;\{\dot{r} \text{ function of pressure}\}$

MASS CHANGE: $\quad \dot{m} = (4\,\pi\,r_p^2)\,\dot{r}\,\rho_p \times N$

REGRESSION VELOCITY: $\quad V_S = \dfrac{\dot{m}}{\rho L}\;\{\rho L \text{ is loading density}\}$

COMBUSTION PRODUCT FLUX: $\quad \rho_g\,V_g = \rho_L\,V_S$

The primary drawback of the fixed bed formulation is its inability to integrate through the propellant bed. Consequently, the physics of bed de-consolidation and particle entrainment into the gas core cannot be modelled. To model the deconsolidation, and movement of the propellant balls due to interphase drag, a more general equation system for a gas-particle mixture is required where the particle phase can occupy significant volume. Details for such a dense two-phase system will be described in Section 6.

5.3   SIMULATION OF GDLS FIRINGS

The fixed bed formulation was used to simulate GDLS firings of the 30 mm ETC/SP gun. The propellant employed for these firings was WC885. In the numerical results presented here, we modeled the propellant as spherical balls whose diameter is specified as the Sautered mean diameter of the propellant balls used in the experimental firings. Thermodynamic information for the propellant such as number of deterrent layers, chemical energy release, and burn rates was taken from closed bomb/equilibrium code data provided by the GDLS/OLIN corporation. We note that the deterrent profile plays a crucial role in determining the pressure history since it alters both the burn rate as well as the energy release. Figure 5.3.1 shows a representative ETC calculation performed for two different deterrent layer models (4-layer vs 15-layer), but otherwise identical conditions. The peak pressure values as well as the qualitative nature of the two curves show significant differences emphasizing the impact of the deterrent profile.
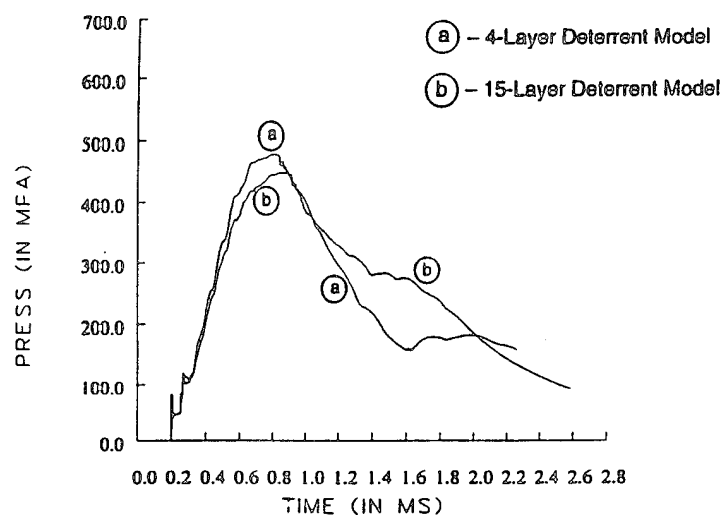
Fig. 5.3.1. Sensitivity of pressure history to deterrent model.

84

The plasma inflow conditions were obtained by supplying the experimentally measured input current to the plasma capillary code of Powell [70]. One of the issues not fully understood was the plasma burst conditions for the moderator tube. The burst conditions obtained from the capillary calculation appeared too high for the material of the moderator tube. It was decided to initialize the plasma at a low pressure of 10 MPa and a temperature of 15000 K. The reasoning for the low pressure initialization was that the plasma might burn through the thin moderator tube rather than burst through. We note that both the experimental and numerical results show sensitivity to the plasma initiation processes and this is clearly an area for further study.

Numerical Simulations were carried out for two 30 mm shot firings by GDLS — Shot 45 and Shot 122. The length and volume of the gun chamber are approximately 20 cm and 161 cc, respectively, and the mass of the projectile is 328 gm. The mass of the propellant in Shot 45 is 151 gm, while Shot 122 had a lower propellant mass of 116 gm. The current inputs to the plasma capillary tube for the two shots are shown in Figs. 5.3.2 and 5.3.3 and indicate that Shot 45 has significantly more plasma energy pumped into

COMPUT VS PC1 COMPARISON
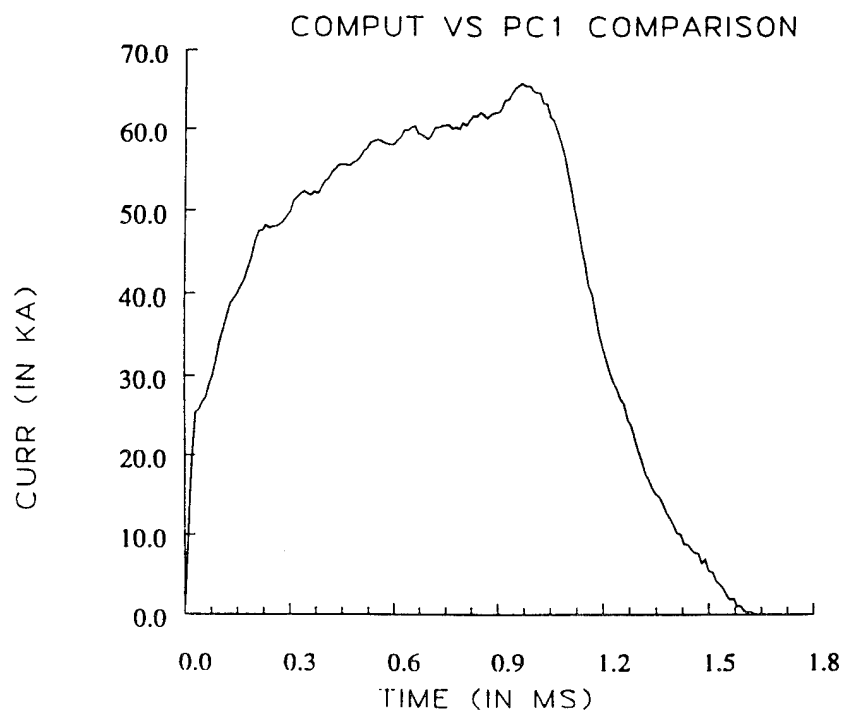
Fig. 5.3.2. GDLS Shot 45 input data: Current history.
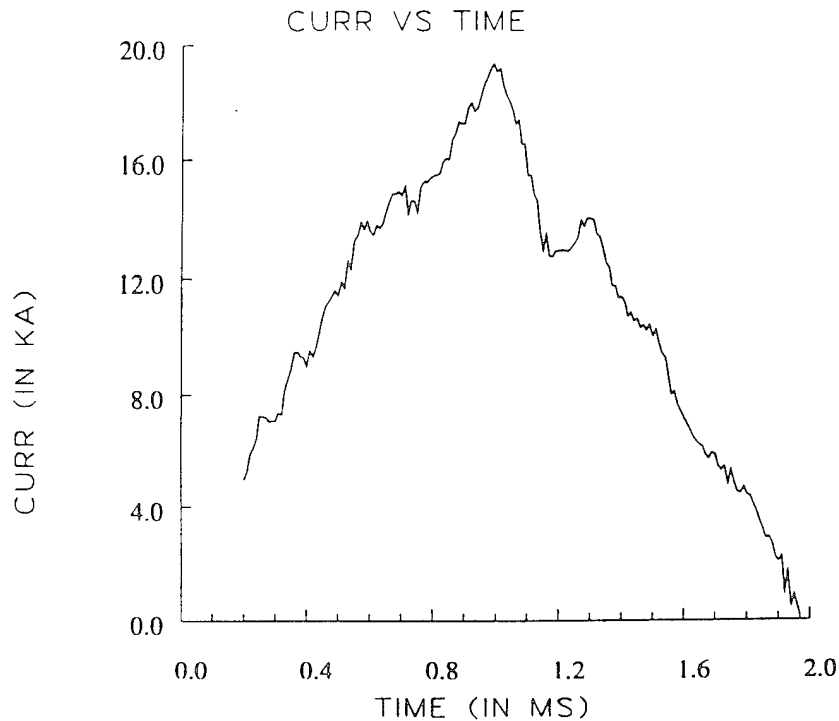
Fig. 5.3.3. GDLS Shot 122 input data: Current history.

the gun chamber. This, combined with the higher propellant mass in Shot
45 would lead us to expect higher performance from Shot 45 as we shall
discuss in the following paragraph.

The numerically computed pressure history and the experimental data
for Shot 45 and Shot 122 are plotted in Fig. 5.3.4 and Fig. 5.3.5, respec-

EXPERIMENTAL PRESSURE   **COMPUTED PRESSURE**
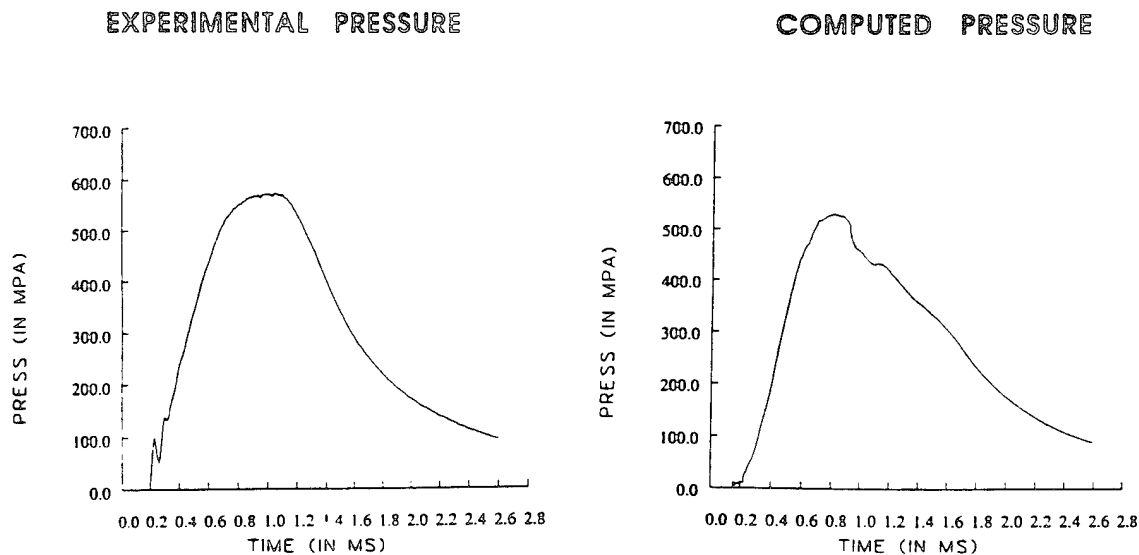
**Fig. 5.3.4. GDLS Shot 45: Comparison of computed pressure history
with experimental data at Port 1.**

86

EXPERIMENTAL PRESSURE   **COMPUTED PRESSURE**
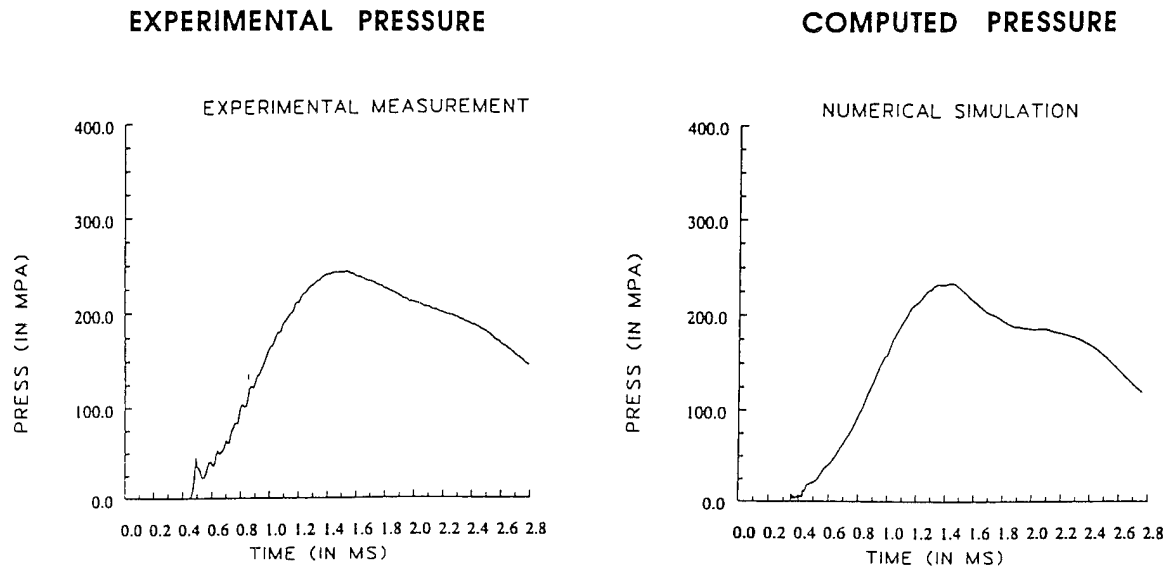
**Fig. 5.3.5. GDLS Shot 122 : Comparison of computed pressure history
with experimental data at Port 1.**

tively. The first observation we make is that the peak pressures and the
risetimes predicted by our calculations compare well with the experimental
values. After the pressure peaks the pressure drop in the latter half of the
ballistic cycle is not predicted as well by the computations. This is probably
because the projectile is moving rapidly at this point and the fixed bed as-
sumption breaks down. The good agreement between the computed and
experimental data also extends to the projectile velocity values. The exper-
imental muzzle velocity at the muzzle exit (130 cm) for Shot 122 is 857
cm/s. The computed muzzle velocity at the same location is 837 m/s — an
error of 2.4 percent.

To illustrate the complex two-dimensional flow structure within the
gun chamber, we show temperature contours at three different times in Fig.
5.3.6. The plasma is being pumped in from the left end and the projectile is
moving to the right. At the earliest time level, very little combustion has oc-
curred and the hot plasma fills most of the chamber. As time increases, the
mass of the products increase and the projectile accelerates. The heavier
products push the lighter plasma out and a complex two-dimensional struc-
ture develops. In the last snapshot, the projectile velocity is considerable
and in the wake behind the projectile, periodic vortex structures are
evident.

87

"LOG TEMPERATURE LEVELS ETC SHOT 45 AT 0.665 MS "

"LOG TEMPERATURE LEVELS ETC SHOT 45 AT 1.065 MS "

"LOG TEMPERATURE LEVELS SP ETC SHOT 45 AT 1.465 MS "
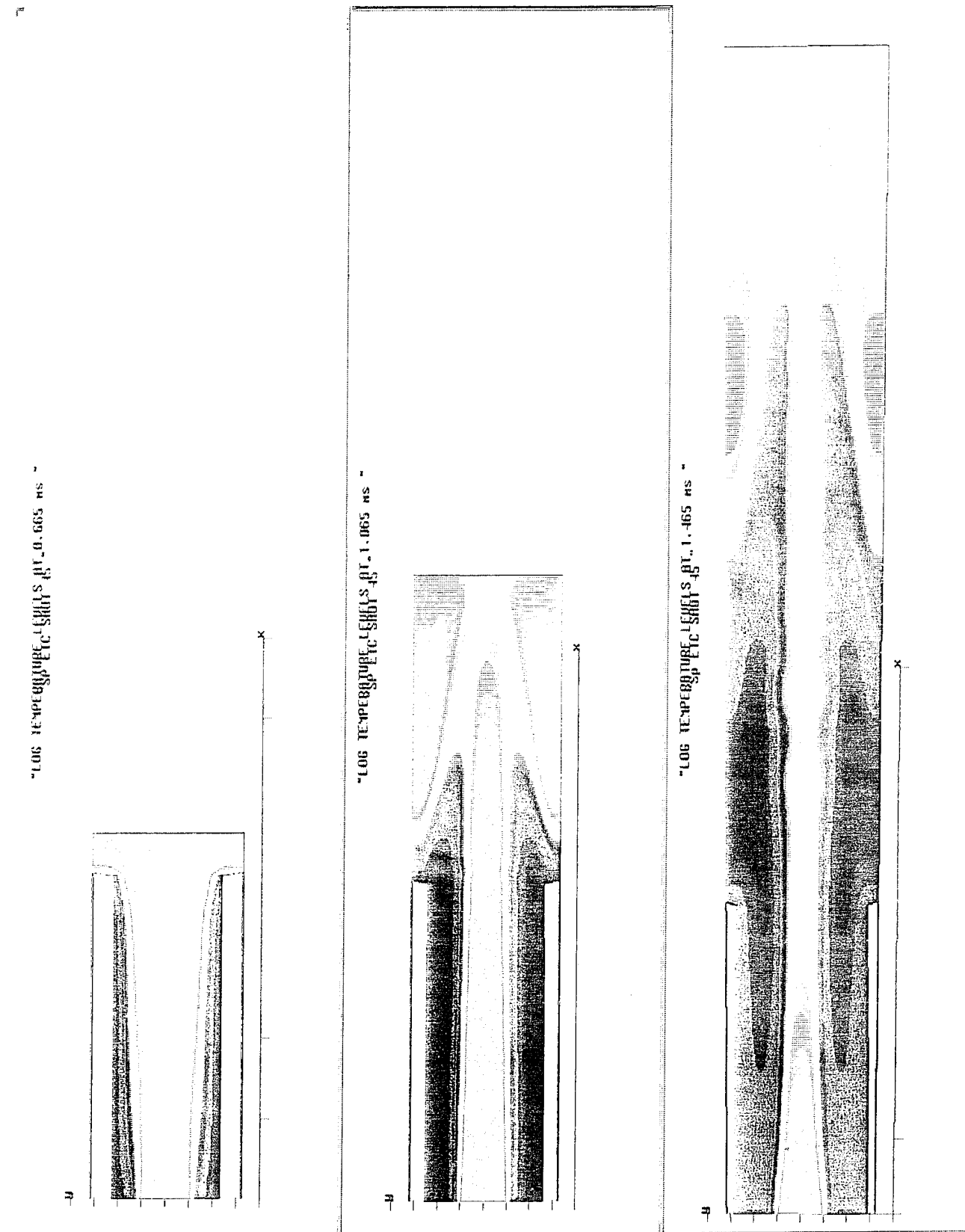
Fig. 5.3.6. Computed log temperature contours in the ETC/SP gun chamber for GDLS Shot 45 at three times: 0.65, 1.065, and 1.465ms.

88

6.0 MULTI-PHASE FORMULATION IN CRAFT FOR GAS/PARTICLE SYSTEMS IN NON-EQUILIBRIUM

In this section, we describe a generalized formulation for a mixture of continuum fluid and an aggregate of incompressible particles with the two phases being out of equilibrium with each other. The continuum fluid, in the general case, can itself be a mixture of various gas species and bulk liquid as was discussed in Section 3. The dispersed phase can be composed of either incompressible solid particulates (as in solid propellant applications), or liquid droplets (as in RLPG applications). The generality of the approach employed for dispersed phase physics permits utilizing the same non-equilibrium framework for both solid and liquid propellant problems. For the sake of clarity, we will restrict our discussions here to gas/solid particle systems. The gas-phase equations in CRAFT are solved with an Eulerian procedure using the upwind numerical framework discussed earlier. Particle motion can be solved using either an Eulerian or a Lagrangian procedure with each procedure entailing its own set of advantages and drawbacks. Eulerian methodology has been implemented in CRAFT for solid propellant and rocket plume/propulsive flowfields [10,11]. As we shall discuss in detail later in this section, the Lagrangian procedure is more appropriate for the ETC/SP configuration. We present numerous validation exercises performed with the new Lagrangian formulation which encompass a wide range of particle volumetric loadings and demonstrate its versatility. The low volumetric loading cases have applicability to rocket nozzles, missile plumes, and gun muzzle blasts, while the high volumetric loadings have applicability to gun interior ballistics, fluidized beds, and spray applications.

6.1 CONTINUUM-PHASE EQUATIONS

The gas phase equations for dense two-phase flows have been derived by various authors for applications to interior ballistics, sprays, fluidized bed flows, etc. The equations presented here are analogous to those originally developed by Gough [74]. In his derivation, Gough has averaged the equations representing the interaction between the two phases over a region representing a cell volume. It is implicitly assumed that cell volumes are larger than particle volumes in this formulation. The gas phase equations, cast in generalized coordinates are given below:

$$\frac{\partial Q}{\partial t} + \frac{\partial E}{\partial \xi} + \frac{\partial F}{\partial \eta} + \frac{\partial G}{\partial \zeta} = S + F_d + F_p + \textit{Viscous Terms} \qquad \textbf{(6.1.1)}$$

where

$$Q = \begin{bmatrix} \rho_g \alpha_g \\ \rho_g u_g \alpha_g \\ \rho_g v_g \alpha_g \\ \rho_g w_g \alpha_g \\ e_g \alpha_g \\ \rho_i \alpha_g \\ \vdots \\ \rho_{n-1} \alpha_g \end{bmatrix}; \qquad E = \begin{bmatrix} \rho_g U_g \alpha_g \\ \left(\rho_g U_g u_g + \ell_x P \right) \alpha_g \\ \left(\rho_g U_g v_g + \ell_y P \right) \alpha_g \\ \left(\rho_g U_g w_g + \ell_z P \right) \alpha_g \\ \left(e_g + P \right) U_g \alpha_g \\ \rho_i U_g \alpha_g \\ \vdots \\ \rho_{n-1} U_g \alpha_g \end{bmatrix} \qquad \textbf{(6.1.2)}$$

In Eq. (6.1.2), ρ_g is the density of the continuum phase which is taken to be a pure gas to simplify our notation. We note that this is merely a subset of the more generalized formulation for the gas-bulk liquid mixture described earlier. If the continuum phase were a gas-liquid mixture, ρ_g would be replaced by ρ_m where ρ_m is defined as $\rho_m = \rho_g \phi_g + \rho_L \phi_L$. The term α_g in Eq. (6.1.2), denotes the volumetric fraction of the continuum phase and is defined as $\alpha_g = 1.0 - V_p / V_{cell}$ where V_p is the total volume occupied by the incompressible particle phase in a cell. The metric quantities, ℓ_x, ℓ_y, ℓ_z, are components of the cell face normal, L, pointing in the positive ξ direction and the magnitude of the metric L is equal to the cell face area. For multi-dimensional flows, the vectors F and G have forms analogous to E and we similarly define metrics M and N corresponding to the cell faces of η and ζ directions, respectively. The quantity U denotes the volume flux through the cell face in the ξ direction and is defined as follows:

$$U = \ell_x u + \ell_y v + \ell_z w \qquad \textbf{(6.1.3)}$$

The source term, S, in Eq. (6.1.1) contains the mass transfer terms due to combustion of the solid propellant particles (or to vaporization/combustion of liquid propellant droplets) and is given as:

90

$$S = \frac{1}{V_{cell}} \Sigma \begin{bmatrix} \dot{m}_g \\ \dot{m}_g u_p \\ \dot{m}_g v_p \\ \dot{m}_g w_p \\ \dot{m}_g \left(h_p + 1/2 \, u_p{}^2 \right) \\ \dot{m}_i \\ \vdots \\ \dot{m}_{n-1} \end{bmatrix}$$

(6.1.4)

Here, $\dot{m}_g$, is gas generation rate from particle combustion whose functional form will be defined in the next section. The vector, F_d, contains the nonequilibrium drag terms and is given as:

$$F_d = \frac{1}{V_{cell}} \Sigma \begin{bmatrix} 0 \\ -A_p \left(u_g - u_p \right) \\ -A_p \left(v_g - v_p \right) \\ -A_p \left(w_g - w_p \right) \\ -A_p \overline{Q}_p \left(\overline{Q}_g - \overline{Q}_p \right) \\ -B_p \left(T_g - T_p \right) \end{bmatrix}$$

(6.1.5)

the details of the drag coefficients A_p and B_p Eq. (6.1.5) have been taken from correlations for packed beds (Gough, Ref. 74).

The vector, F_p, contains additional source terms due to volumetric effects and is given as:

91

$$F_p = \begin{bmatrix} 0 \\[4pt] +P\left[\dfrac{\partial}{\partial\xi}\left(\ell_x\alpha_g\right)+\dfrac{\partial}{\partial\eta}\left(m_x\alpha_g\right)+\dfrac{\partial}{\partial\zeta}\left(n_x\alpha_g\right)\right] \\[4pt] +P\left[\dfrac{\partial}{\partial\xi}\left(\ell_y\alpha_g\right)+\dfrac{\partial}{\partial\eta}\left(m_y\alpha_g\right)+\dfrac{\partial}{\partial\zeta}\left(n_y\alpha_g\right)\right] \\[4pt] +P\left[\dfrac{\partial}{\partial\xi}\left(\ell_z\alpha_g\right)+\dfrac{\partial}{\partial\eta}\left(m_z\alpha_g\right)+\dfrac{\partial}{\partial\zeta}\left(n_z\alpha_g\right)\right] \\[4pt] -P\dfrac{\partial\alpha_g}{\partial t} \\[4pt] 0 \\ \vdots \\ 0 \end{bmatrix} \qquad (6.1.6)$$

In Eq. (6.1.6) we note a small point of difference in our methodology with the formulation of Gough (Ref. 21). Gough represents the pressure flux term in the momentum equation as $\alpha_g \nabla P$. For numerical convenience in retaining the upwind framework, we have rearranged this term as follows:

$$\alpha_g \nabla P = \nabla\left(\alpha_g P\right) - P\nabla\alpha_g \qquad (6.1.7)$$

In Eq. (6.1.7), we have a strongly conservative form of the pressure flux term $\nabla(\alpha_g P)$ which facilitates the implementation of an upwind numerical procedure, and, we discussed earlier, is critical to capture discontinuities within the flowfield. We note that the equations described for the continuum phase are independent of the formulation utilized for the particle-phase. In interacting with the particle-phase, the gas equations require only the interphase interaction terms, namely: particle porosity α_p, drag/heat transfer terms (F_d), and, combustion source terms (S). Hence, either an Eulerian or a Lagrangian solution procedure for the particle phase can be coupled as a module to the continuum phase equations with no loss of generality or physics.

6.2 PARTICLE-PHASE EQUATIONS

In formulating the numerical procedure to be implemented for the particulate phase in ETC/SP simulations, we began by evaluating the relative merits of Eulerian and Lagrangian formulations for the particle phase. Our experiences with the fixed-bed formulation (described in Section 5) indicated that it was very important to model discrete particulate combustion

since the deterred burn properties of the particle are a strong function of the particle diameter. The diameter of individual particles can be accurately tracked only in a Lagrangian scheme. In an Eulerian procedure, scalar convection equations are solved for the surface area of particles in each particle group. The mean diameter in each group would then have to be coupled with an assumed PDF to get the particle diameter distribution. Hence, an Eulerian scheme would most likely not provide the required accuracy in particle combustion problems with rates sensitive to size variation.

Another consideration in deciding upon the numerical scheme is the modeling of the particle-particle collisions. For dense systems, the time between collisions decreases, with frequent collisions altering the local volume fraction occupied by particles. This directly affects the gas-phase equations since it alters the volume available for the gas to occupy. In a Eulerian scheme, while the interactions between different particle groups can be modeled, the particles within the same group can only have a single mean property at a point in space. This condition is very restrictive when there are intersecting streams of particles because the Eulerian scheme will yield a single "averaged" stream in the mean direction of the two incident streams. In a Lagrangian scheme, the grazing collisions can be estimated with stochastic methods although the methodology is quite involved. Based on the above discussion, a Lagrangian solution procedure was chosen as the more appropriate methodology for ETC/SP problems of interest since it better represents the discrete physics, and can be extended to treat collisions in an exact manner.

The Lagrangian equations for each individual particle are given as follows:

$$\frac{dr}{dt} = bP^n \qquad (mass) \tag{6.2.1a}$$

$$m_p \frac{d\bar{Q}_p}{dt} = +A_p\left(\bar{Q}_g - \bar{Q}_p\right) - v_p \nabla P + \frac{-V_{cell}}{N_{cell}} \rho_p a^2\left(\alpha_g\right)\nabla\alpha_g \qquad (momentum) \tag{6.2.1b}$$

$$m_p \frac{dh_p}{dt} = B_p\left(T_g - T_P\right) \qquad (energy) \tag{6.2.1c}$$

We note that the coefficients for the pressure based burn rates and the product enthalpy are provided from experimental data at various points

along the deterrent profile. Since we track the diameter of each particle, the coefficients at any given diameter are then interpolated from the deterrent data curve. A second observation we make is that the Lagrangian equations described above do not contain any stochastic modeling for collision effects. This is an area for future study. However, we have included an intergranular stress term for densely packed beds. From an Eulerian viewpoint, the intergranular stress term may be interpreted as a macroscopic model for collisions. The form of this intergranular stress has been adapted to the Lagrangian formulation from the term given by Gough [74] for his Eulerian formulation.

We again note that an Eulerian particle module is operational in CRAFT for gas-particle flows where the particle mass loading is substantial, but volumetric effects are negligible [10,11]. Heavy particles such as Al_2O_3, encountered in rocket propulsive flows, can have significant mass loadings (approximately 40%) but occupy small volumes. The particle conservation equations are solved in an upwind fashion to mimic the gas-phase numerics and the formulation allows for non-equilibrium between phases as well as phase-change for the particles as they heat-up or cool down. The Eulerian package has been used extensively to study transient and steady flowfields in rocket nozzles, exhaust plumes, and other aerodynamic applications where the dilute particle formulation is appropriate.
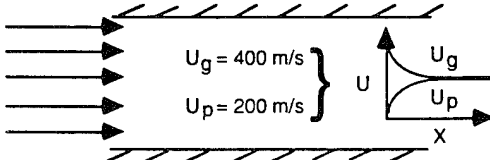
6.3 VALIDATION OF TWO-PHASE FORMULATION FOR LOW VOLUMETRIC LOADINGS

The two-phase formulation with the Lagrangian solution procedure for the particles has been validated by computing a number of steady and transient unit test problems for low volumetric loading and comparing these with the previously developed Eulerian formulation in CRAFT. The steady state problems were chosen primarily to verify that particle velocity and temperature equilibration, as well as non-equilibrium interaction with the gas were implemented properly. The transient problems were computed to verify that the non-equilibrium terms alter the acoustic propagation in the expected fashion, yielding the value predicted analytically by the equilibrium two-phase formulation in the limit when non-equilibrium effects become negligible. These validation cases are described in the following paragraphs.

6.3.1 Steady Flow Test Cases

The steady-state test case chosen was a tube with 1-D gas-particle flow within it (see Case I in Table XIV). The gas and particle flowfields are out of equilibrium at the inflow, and we compare the velocity and temperature equilibration lengths as they travel down the tube. The first calculation was performed with one-way coupling, i.e., only the particles experience the interphase drag while the gas solution remains unaffected. The gas velocity at the inlet is 100 m/s and its temperature is 300 K. The particle velocity and temperature are half that of the gas at the inlet. The particle diameter is 10μm which yields a particle lag Reynolds number of 10. The particle volumetric loading is negligibly small and the mass loading density at the inlet is 0.5. Since the volumetric loading is small the Eulerian particle package for dilute two-phase flows is used to generate the Eulerian solution. The solution obtained using the new Lagrangian package is compared with the Eulerian formulation which has been validated extensively in our previous work (Ref. 10).

**Table XIV. Validation Studies of Lagrangian Formulation
for Dense Two-Phase Flows**

**CASE I: STEADY 1-D FLOW
(LOW VOLUMETRIC LOADING)**

OBJECTIVE: Verify particulate velocity and temperature equilibrium with gas flowfield by comparison with Eulerian solution

$U_g = 400$ m/s
$U_p = 200$ m/s

**CASE II: TRANSIENT SHOCK TUBE
(LOW VOLUMETRIC LOADING)**

OBJECTIVE: Verify transient interaction of particle motion and gas flowfield by comparison with Eulerian solution

$P_g = 1$ atm	$P_g = 1.1$ atm
$T_g = 300$K	$T_g = 330$K
$\phi_p = 5 \times 10^{-4}$	$\phi_p = 5 \times 10^{-4}$

**CASE III: TRANSIENT SHOCK TUBE
(HIGH VOLUMETRIC LOADING
GUN PRESSURE CONDITION)**

OBJECTIVE: Verify transient interaction of particle motion and gas flowfield by comparison with Eulerian solution

$P_g = 117$MPa	$P_g = 128$MPa
$\phi_p = 0.3$	$\phi_p = 0.3$
$D_p = 10\mu$m	$D_p = 10\mu$m

95

In Fig. 6.3.1.1, we plot the velocity, temperature and loading density of the particles as they travel downstream. In Figs. 6.3.1.1a and 6.3.1.1b (particle velocity and temperature), the solid line is the Lagrangian solution while the dotted line is the Eulerian solution. The two solutions compare very well in terms of the equilibration lengths and shape of the curve. The Lagrangian solutions for the velocity and temperature are smoother than the Eulerian solution because these quantities are integrated continuously in the Lagrangian case, while their accuracy is limited by the grid size in the Eulerian case.
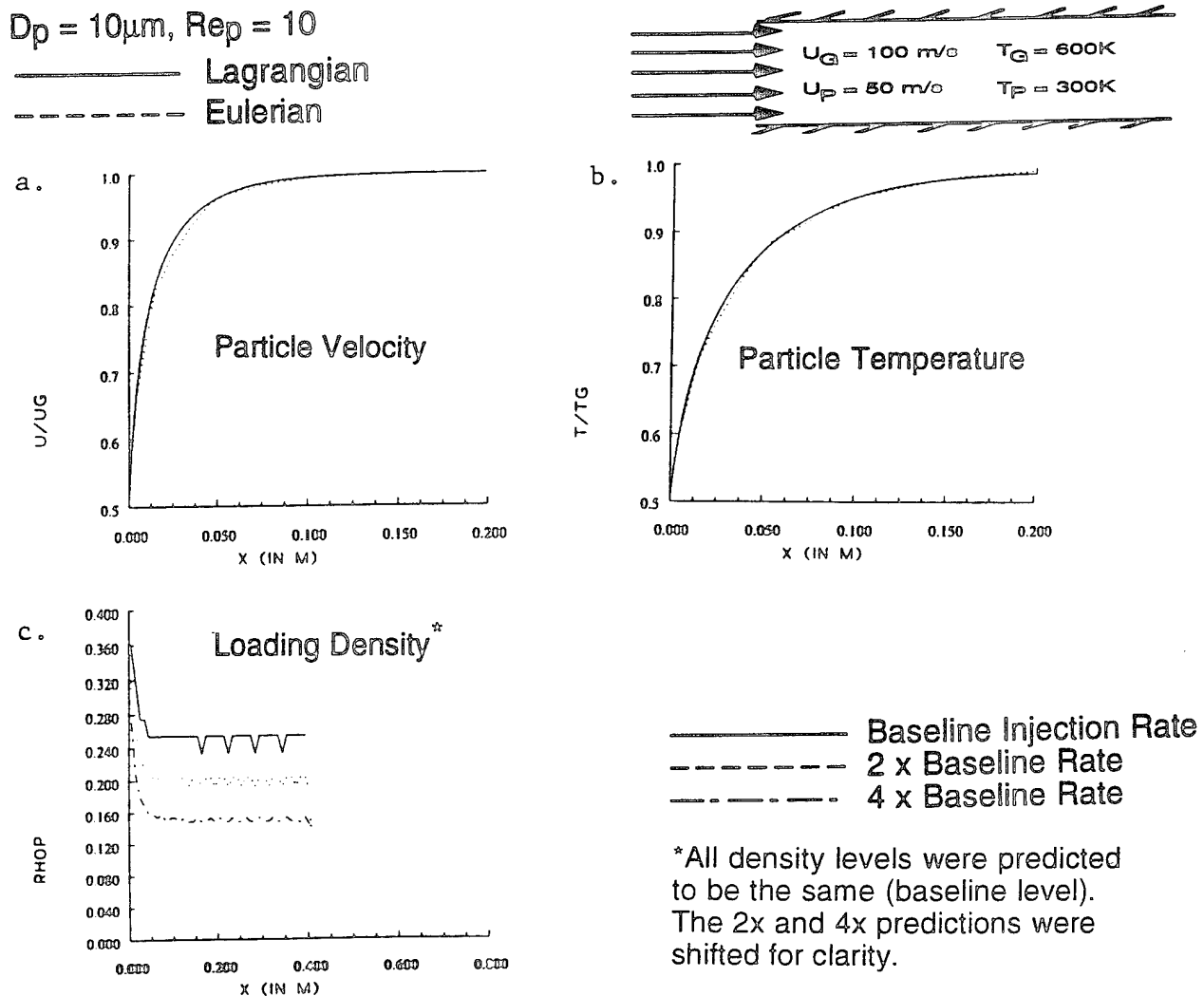
Figure 6.3.1.1. Steady-state equilibration of particles (one-way coupling).

In contrast to the particle velocity and temperature profile, the particle loading density in a Lagrangian formulation shows oscillations (Fig. 6.3.1.1c). This is because the loading density in the Lagrangian case is ob-

tained after the time-step integration by processing the positions of discrete particles which are tracked computationally. Hence, in a statistical sense, we are approximating a continuous solution by a finite sample size. Therefore, as the sample size becomes larger, we expect the oscillations to get smaller. This effect is illustrated in Fig. 6.3.1.1c which shows the loading density computed from the Lagrangian calculation for three different particle injection rates at the inflow. As the number of particles being tracked increases, the oscillations which were observed for the baseline rate clearly dampen and the solution becomes smoother.

The 1-D gas-particle flow in the tube is now computed with two way coupling between the gas and particle phase, i.e., the gas flowfield is affected by the interphase drag as well. The gas at the inflow has a pressure of 1 atm and the particle mass loading is 0.5. The volumetric loading remains negligibly small. The initial gas velocity is 400 m/s while the particle velocity is half that at 200 m/s. The particle lag Reynolds number at these conditions is 65. The gas and particle temperatures are identical at the inflow. However, this changes downstream since the gas heats up due to viscous dissipation and subsequently this results in interphase heat transfer.

The particle and gas solutions with the two-way coupling are plotted in Figs. 6.3.1.2 and 6.3.1.3 respectively. These solutions are plotted 2 ms after particle injection began at the inflow. Prior to discussing the results, we note that at 2 ms, the gas solution still shows transient effects because the non-equilibrium interactions produce waves that persist after equilibration. Figure 6.3.1.2 shows the particle solution for the Lagrangian and Eulerian calculations. The particle velocity and temperatures compare exactly for the two cases. The particle velocity is monotonically equilibrating with the gas velocity. The particle temperature rises slightly because, as mentioned earlier, the gas temperature increases due to viscous dissipation. The particle loading densities at 2 ms are plotted in Fig. 6.3.1.2c. The particle front has propagated to a distance of 0.8 m. The Lagrangian particle front preserves the discontinuity across the front, while the Eulerian solution smears the discontinuity. The Lagrangian and Eulerian loading density profiles are different, as expected, because the Eulerian procedure treats the particle loading density as a continuous function while, as discussed before, the Lagrangian solver solves for the individual particles.

97

Dp = 10μm, Rep = 65
Mass Loading $= 0.5$
Volumetric Loading $\cong 10^{-4}$

$U_g = 400$ m/s
$U_P = 200$ m/s
$T_G = T_P = 300K$

a.

Particle Velocity

UP/UINF

X (IN M)

b.

Particle Temperature

TP/TINF

X (IN M)

c.

Loading Density

RHOP

X (IN M)

—————— Eulerian
– – – – – – Lagrangian
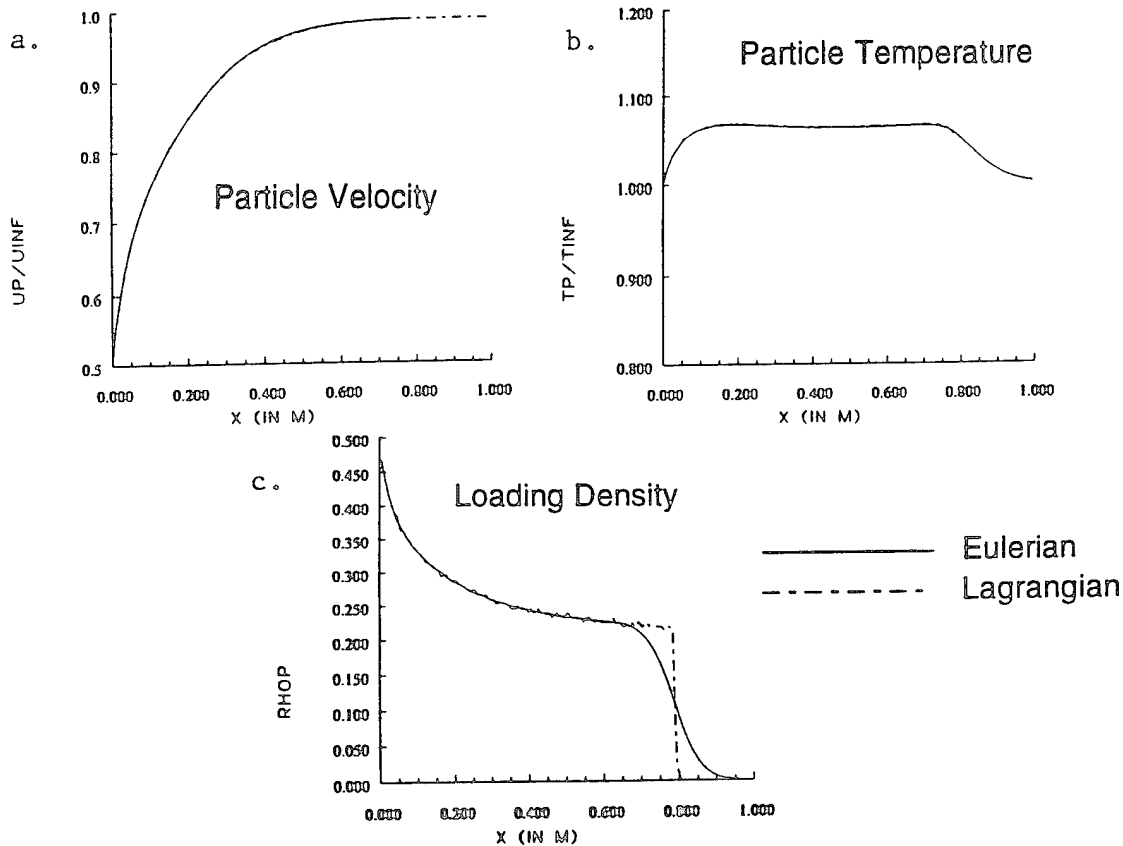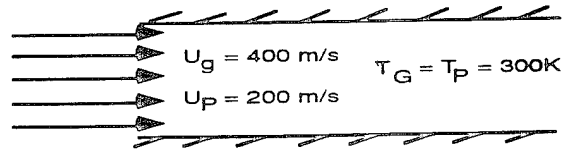
Figure 6.3.1.2. Particle solution 2ms into injection with two-way coupling.

The gas-phase solution at 2 ms is plotted in Fig. 6.3.1.3. We observe that although the particle front has propagated to 0.8 m by 2 ms, the non-equilibrium effects on the gas are evident only to a distance of 0.4 m. Beyond 0.4 m, the gas velocity and pressure are the original initialized values. In the region where the gas experiences significant drag, the gas velocity drops and the gas pressure rises. In fact, the gas pressure at the inlet has gone up to 1.6 and the velocity in the first axial cell has dropped to 0.73 from the initialized value of 1.0.

$D_p = 10\mu m$, $Re_p = 65$
Mass Loading $= 0.5$
Volumetric Loading $\cong 10^{-4}$

$U_g = 400$ m/s

$T_G = T_P = 300K$

$U_p = 200$ m/s

GAS PRESSURE

a.

GAS VELOCITY

b.
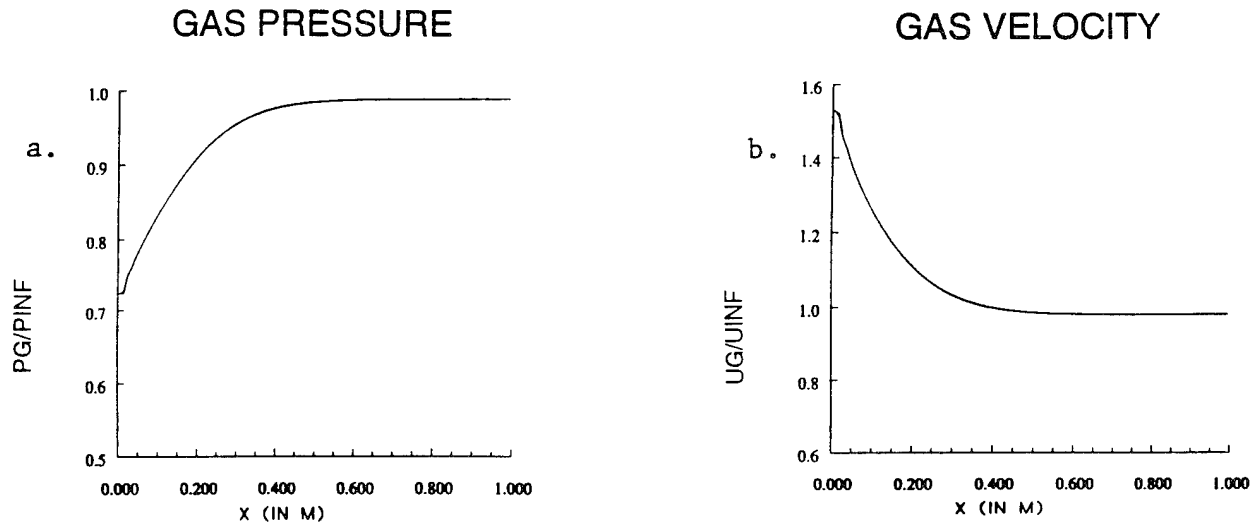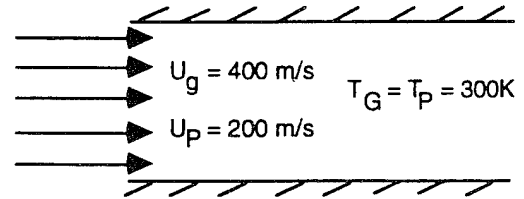
Figure 6.3.1.3. Gas solution 2ms into injection with two-way coupling.

6.3.2 Transient Test Cases

To validate the Lagrangian two-phase code for transient flowfields, we set up a two-phase shock tube problem (Case II and III in Table XIV). The pressure ratio across the diaphragm is 1.1. A low pressure ratio is chosen so that we can estimate the acoustic speed rather than the speed associated with a strong shock. The temperature is 300°K in both chambers. The mass loading of particles is 0.5, with the particle diameter being 10 mm. Two sets of calculations were performed with different pressure levels. The first case is for a low mean pressure of 1 atm. At this pressure, the volumetric loading of particles for the given mass loading is 5×10^{-4}. The second case is for a high pressure of 117 MPa which is in the regime of gun flowfields. Since the gas is very dense at this high pressure, the mass loading of 0.5 results in a volumetric loading of 0.3.

99

Figures 6.3.2.1 and 6.3.2.2 show the gas and particle solutions for the low pressure shock tube at the following times: 0.4, 0.8, 1.2 ms. The gas pressure profiles are plotted in Fig. 6.3.2.1a and the gas velocity in Fig. 6.3.2.1b. The solid line shows the profiles for a pure gas case with no particles present. The two-phase solutions are obtained using both the Eulerian and the Lagrangian procedures and are plotted using two different types of dashed lines. However, the Lagrangian and Eulerian solutions fall on top of each other and appear as a single plot. The pressure profiles plotted in Fig. 6.3.2.1a indicate that at these low volumetric loadings, the acoustic speed of the gas slows down relative to the pure gas phase solution. In particular, the pressure profile at 1.2 ms indicates that in addition to slowing down, the acoustic wave is dispersing. The dispersive nature of the acoustic waves in non-equilibrium flows has been extensively studied in the literature by various authors [75] for linear wave equations which afford analytical solutions, and is a well known phenomena. The decrease in the acoustic speed at these flow conditions can also be verified by looking at the equilibrium speed of sound from the equilibrium two-phase formulation. The equilibrium acoustic speed when the second medium is incompressible is as follows:

$$\left(\frac{C_m}{C_g}\right)^2 = \frac{\gamma_m}{\gamma_g}\frac{1}{\left(1+\sigma_g\right)\phi_g^2} \qquad \left\{\sigma_g = \frac{\rho_p\phi_p}{\rho_g\phi_g}\right\} \qquad (6.3.2.1)$$

where C_m is the acoustic speed for the mixture, C_g is the acoustic speed for a pure gas phase and σ_g is the mass loading of particles. From Eq. (6.3.2.1) it is clear that at low volumetric loading, ϕ_g is close to 1.0 and the mixture acoustic speed drops in proportion to $(1 + \sigma_g)^{-1}$.

The particle loading density and velocities are plotted in Fig. 6.3.2.2 for the same three times. The particle velocity is lower than the gas velocity (Fig. 6.3.2.1b) which shows that the particles have not yet attained equilibrium. Furthermore, the slope of the particle velocity profile on either side of the diaphragm is of opposite sign. The change in the slope of the particle velocity around the original diaphragm location is reflected in the particle loading density profiles which show a discontinuity at the diaphragm location. On the right side, the particle loading density is dropping since the gas is expanding, while on the left side, it is increasing since the gas is be-

ing compressed. The Lagrangian and the Eulerian loading density profiles compare well in magnitude and shape. However, as discussed above, the Lagrangian solution shows oscillations while the Eulerian solution is smooth but smeared. We note that since the particle volumetric loading is low, the oscillations in the particle loading density are not reflected in the gas pressure or velocity profiles. However, as the volumetric loading goes up, the oscillations in the volumetric loading also affect the gas phase solution as we shall describe in the following paragraphs for the high-pressure shock tube.

$D_p = 10\mu m$

Mass Loading of Particles = 0.5

Mean Gas Pressure = 1 atm

$P_g = 1\text{atm}$	$P_g = 1.1\text{atm}$
$T_g = 300K$	$T_g = 330K$
$\phi_p = 5 \times 10^{-4}$	$\phi_p = 5 \times 10^{-4}$

————————— Pure Gas (Single Phase)
— — — — — — — Lagrangian
— · — — · — — · Eulerian

LAGRANGIAN AND EULERIAN RESULTS ESSENTIALLY IDENTICAL
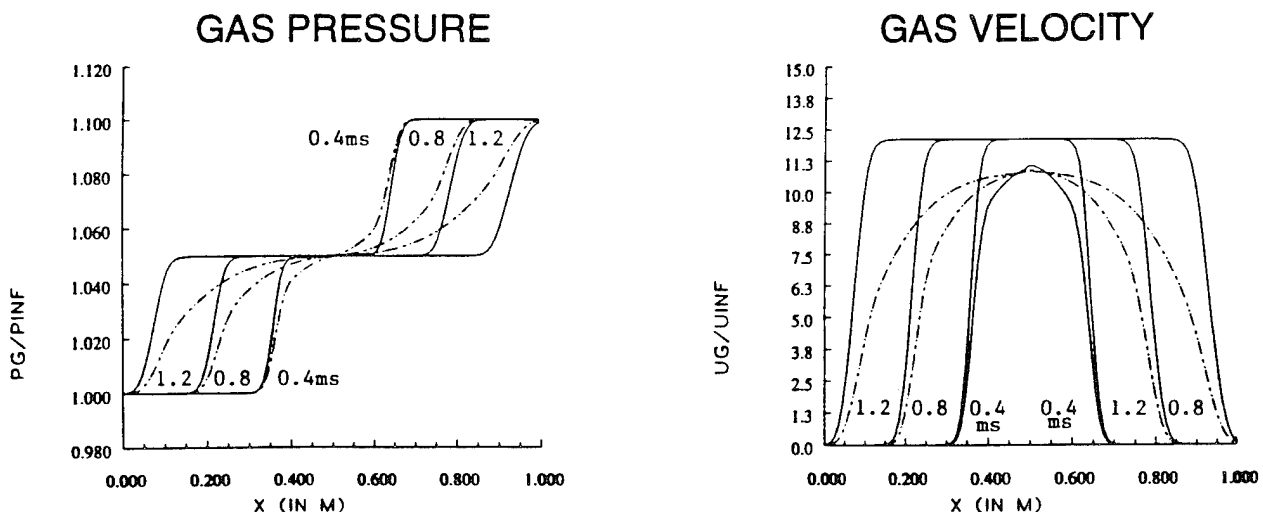
Figure 6.3.2.1. Shock tube with low volumetric loading: Gas-phase results.

Dp = 10μm

Mass Loading of Particles = 0.5

Mean Gas Pressure   = 1 atm

P_g = 1atm	P_g = 1.1atm
T_g = 300K	T_g = 330K
ϕ_p = 5 x 10^{-4}	ϕ_p = 5 x 10^{-4}

LOADING DENSITY - Lagrangian

LOADING DENSITY - Eulerian

PARTICLE VELOCITY

LAGRANGIAN AND EULERIAN RESULTS ESSENTIALLY IDENTICAL
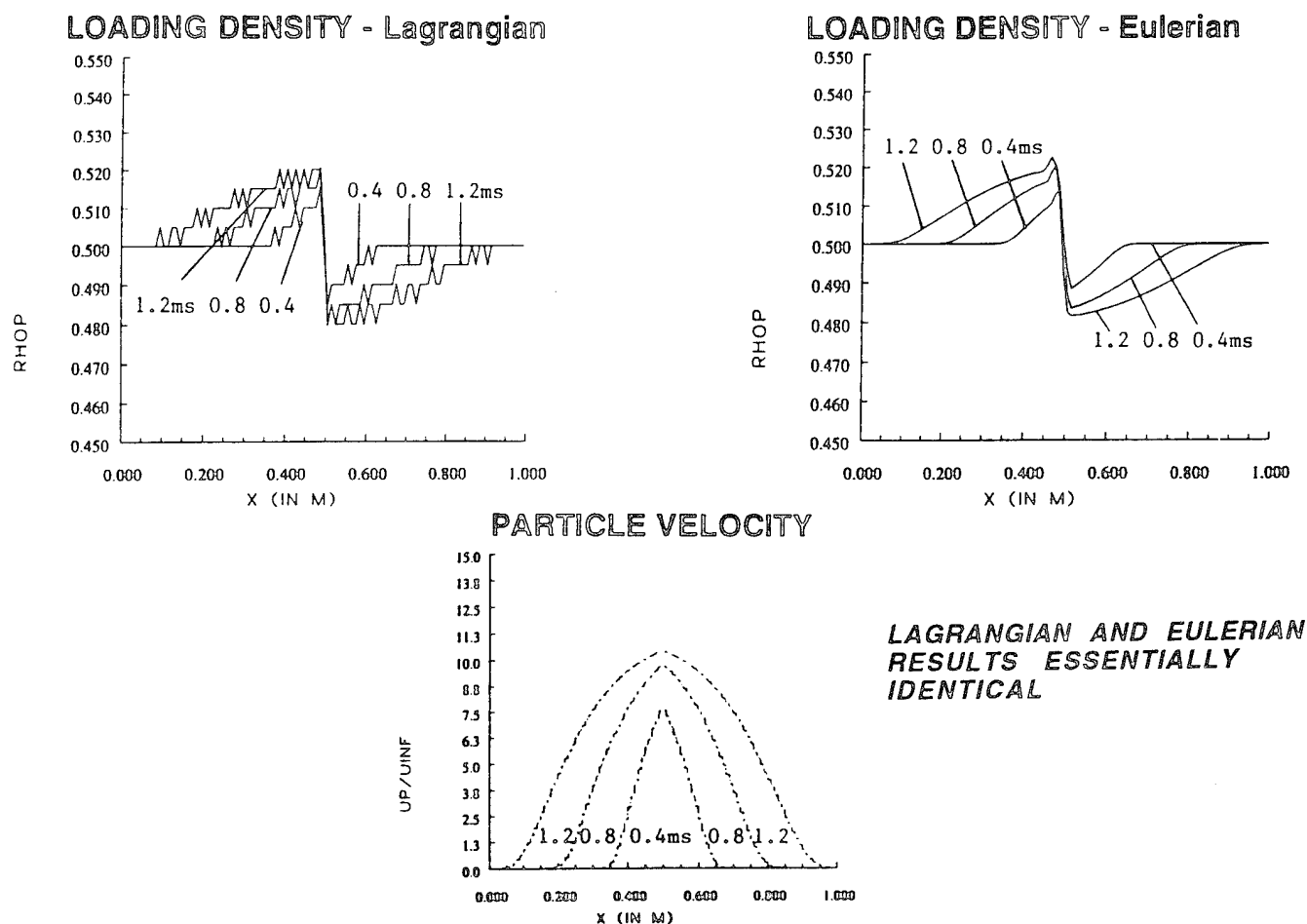
Figure 6.3.2.2. Shock tube with low volumetric loading: Particle-phase results.

The solutions for the high-pressure shock tube (117 MPa) are shown in Fig. 6.3.2.3 at the same three time levels as in the earlier case. Figure 6.3.2.3a shows the pressure profiles, while Fig. 6.3.2.3b shows the corresponding particle loading density profiles. The first observation made is that the acoustic speed goes up considerably at these flow conditions and is larger than the pure-gas phase solution. For instance, at 1.2 ms the pressure wave has reached the end walls and reflected off, while the pure gas solution in Fig. 6.3.2.1a has still not yet reached the end walls. The increase in acoustic speed can also be deduced from the equilibrium sound speed expression in Eq. (6.3.2.1). Since ϕ_g drops to 0.7, the volumetric effect of ϕ_g^2

overrides the effect of the mass loading and increases the acoustic speed. The second observation made is in regard to the effect of particle loading densities on the pressure. Since the volumetric loading is substantial, the oscillations in the Lagrangian loading density profiles now generate ripples in the gas pressure profiles.

$D_p = 10\mu m$
Mass Loading of Particles $= 0.5$
Volumetric Loading of Particles $= 0.3$
Mean Gas Pressure $= 117$ MPa

$P_g = 117MPa$	$P_g = 128MPa$
$T_g = 300K$	$T_g = 330K$
$\Phi_p = 0.3$	$\Phi_p = 0.3$

GAS PRESSURE PROFILES

PARTICLE LOADING DENSITY PROFILES
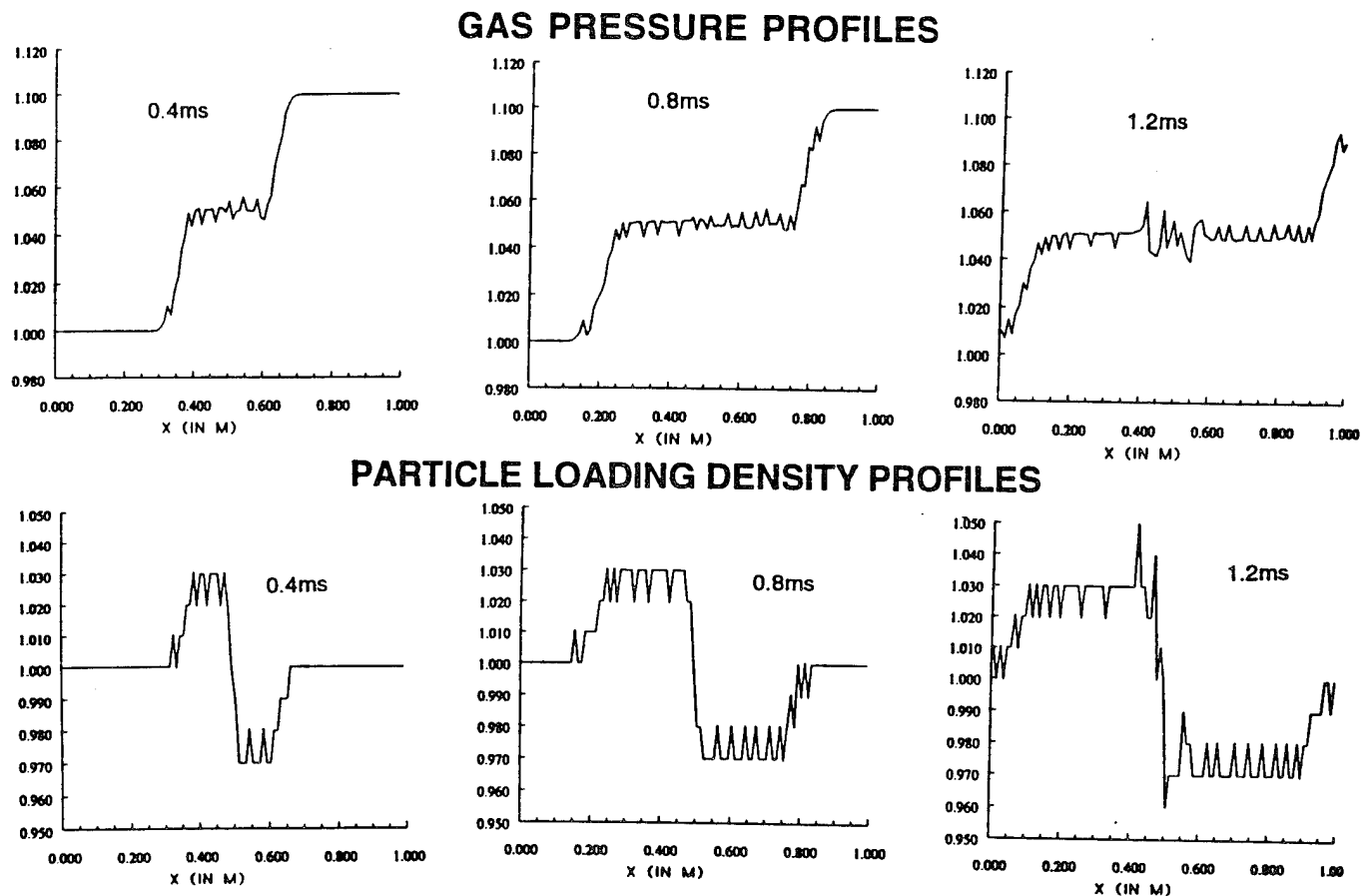
Figure 6.3.2.3. Shock tube with high volumetric loading: Gas pressure and particle loading at various times.

103

6.4 CRAFT VALIDATION STUDIES FOR SOLID PROPELLANT INTERIOR BALLISTIC APPLICATIONS

In this section, we report a series of validation exercises which were performed to evaluate the ability of CRAFT to model solid-propellant IB applications. We begin by computing the Love and Pidduck Lagrange problem to ensure that the gas-phase thermodynamics and projectile movement is modelled accurately. Subsequently, we compute a series of cases for a representative 30 mm solid propellant gun. These calculations are done in sequence of increasing complexity beginning with a closed bomb case, 1-D calculations for different propellant loadings, and finally culminating with a multi-dimensional calculation, with plasma injection, which is representative of a ETC gun. For the closed bomb and 1-D cases, the results from CRAFT are compared with results obtained using the XKTC code [76] which has been validated extensively.

6.4.1 Lagrange Problem (Love and Pidduck)

In Figure 6.4.1.1 we plot the pressure distribution at various times (0.4772ms–10.23ms) for the problem posed by Love and Pidduck [77]. The pressure profiles compare very well with the results quoted by Love and Pidduck. The differences in the projectile travel and base pressure for each curve is shown in Table XV. The maximum difference in base pressure is 0.43 percent at 10.23 ms, while the maximum difference for projectile travel is -0.53 percent at 5.154ms. These results allow us conclude that the boundary condition at the accelerating projectile base accurately computes the expansion waves emanating from the projectile without introducing significant conservation errors. We note that Love and Pidduck obtained their results using a method of characteristic (MOC) integration procedure wherein the Riemann variables are tracked along each characteristic. When there are waves of different families (expansion and compression) crossing each other, the accuracy of the solution would depend on the number of characteristics tracked. Love and Pidduck tracked 11 characteristics in their calculation. It is interesting to observe that for curve 4 (2.117 ms) and curve 8 (7.137 ms) the pressure error flips sign. We observe that at these two times, the reflection from the breech reaches the projectile and reflects back. Using a larger number of characteristics may have an impact at these times when a MOC procedure is employed.

104
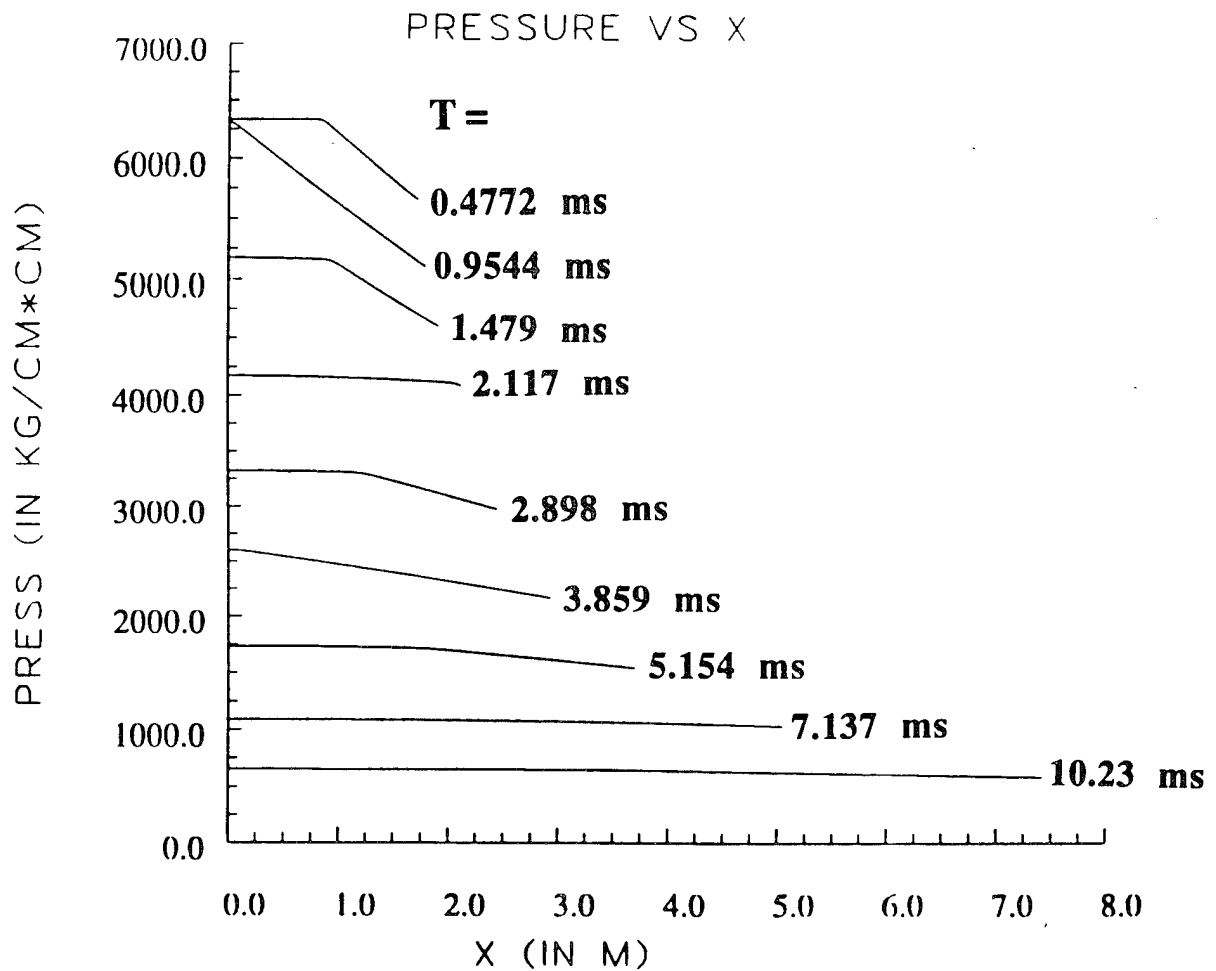
Fig. 6.4.1.1. Pressure profiles at various times computed by CRAFT for Love & Pidduck Lagrange problem.

Table XV. Love & Pidduck Problem

Time (in ms)	Projectile Travel (in cm)			Pressure on Projectile (kg/cm²)		
	Love & Pidduck	CRAFT	Difference %	Love & Pidduck	CRAFT	Difference %
0.4772	2.4	2.404	−0.16%	5651.3	5652.6	+0.023%
0.9544	9.28	9.2777	−0.02%	5097.2	5099.02	+0.035%
1.479	21.4	21.468	+0.317%	4598.7	4599.22	+0.01%
2.117	42.191	42.174	−0.04%	4102.5	4086.08	−0.40%
2.898	75.4	75.083	−0.42%	2970.3	2975.30	+0.16%
3.859	124.3	124.14	−0.12%	2161.6	2165.32	+0.17%
5.154	202.1	201.023	−0.53%	1535.2	1541.06	+0.38%
7.137	335.6	335.545	−0.016%	1030.2	1028.21	−0.19%
10.23	571.9	571.84	−0.0104%	581.6	584.104	+0.43%

105

6.4.2 Solid-Propellant Interior Ballistic Calculations

The ability of CRAFT to accurately model conventional solid-propellant guns was evaluated by simulating a 30 mm gun for various propellant loadings. The geometry of the gun chamber is taken to be cylindrical with a volume of 141 cc. The propellant employed is M-30 and is specified to be in the form of spherical balls with a diameter of 1 mm. The mass of the projectile is specified as 150 gm. To simplify the problem, details which are secondary for the purpose of code validation (i.e. such as shot start, barrel resistance, barrel heat loss, etc.) have been dropped from this exercise.

6.4.2.1 Closed Bomb Case

The pressure and temperature history for the closed bomb case (propellant loading 0.25 g/cc) are shown in Fig. 6.4.2.1.1. The CRAFT and XKTC solutions match exactly on the scale of the plot (Figs. 6.4.2.1.1a and b). However, when the scale of the plot is blown up around the equilibrium value minor differences can be observed (as seen in Figs. 6.4.2.1.1c and d). The analytical equilibrium pressure value is 373.411 MPa while the corresponding temperature value is 2952.72 K. The CRAFT solution reaches equilibrium at approximately 4.6 ms with a pressure of 373.374 MPa and a temperature of 2952.43 K which are in excellent agreement with the analytical values. Furthermore, these values subsequently remain unchanged indicating that the code is conserving energy and mass exactly. The solution computed by XKTC attains a equilibrium value of 373.374 MPa and 2952.43 K by 4.6 ms. However, after attaining equilibrium a minor amount of pressure and temperature drop is observed.

6.4.2.2 1-D Gun Calculations

A series of 1-D gun tube calculations are performed for propellant loadings varying from 0.1 g/cc to 0.75 g/cc. Here, we present results for two cases: the 0.1 and 0.75 g/cc cases. Fig. 6.4.2.2.1 (a-d) shows the breech pressure, projectile pressure, projectile velocity and displacement respectively for the CRAFT (solid line) and XKTC (dashed line) solutions. The two solutions compare very well with the peak breach pressure being approximately 10.5 MPa. Furthermore, the projectile velocity and displacement match exactly on the scale of the plot. The corresponding comparisons for the 0.75 loading case are shown in Fig. 6.4.2.2.2. The two solutions compare

PRESSURE HISTORY
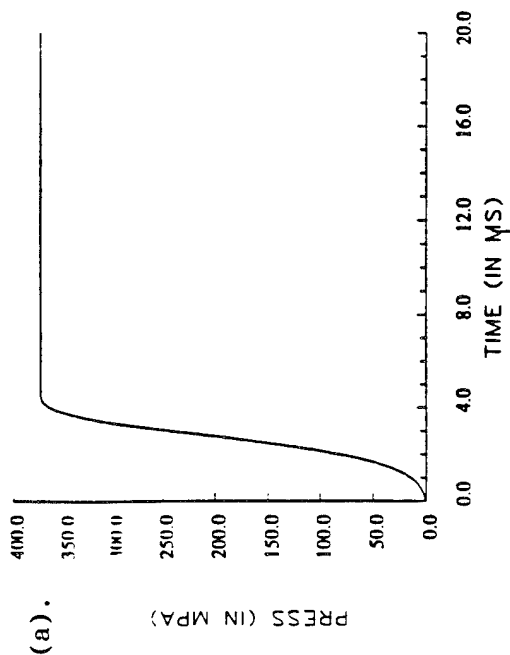
PRESSURE HISTORY (Enlarged Scale)

(a).
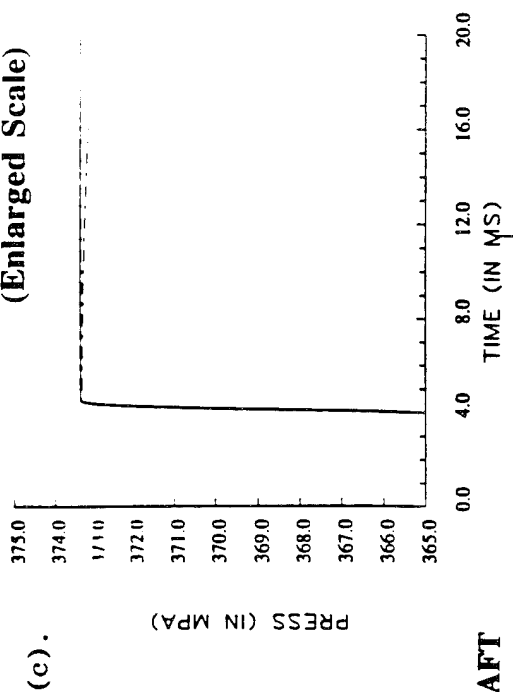
(c).

TEMPERATURE HISTORY
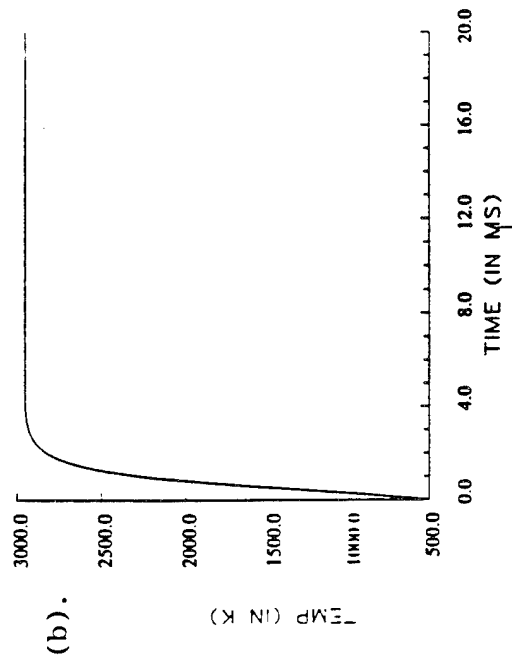
TEMPERATURE HISTORY (Enlarged Scale)

(b).

(d).
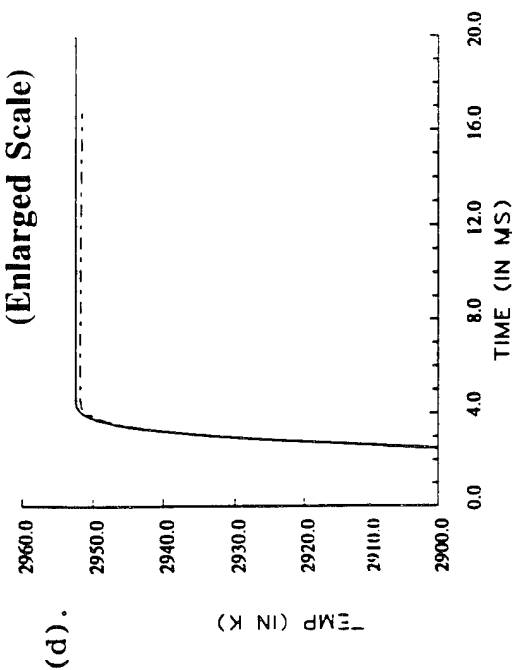
—— CRAFT

- - - - XKTC

Fig. 6.4.2.1.1.   Closed bomb calculation for 0.25 g/cc loading case: Pressure and Temperature History compared for CRAFT and XKTC solutions.

(a). BREECH PRESSURE — PRESS (IN MPA), TIME (IN MS)

(b). PROJECTILE VELOCITY — VEL (IN M/S), TIME (IN MS)

(c). PROJECTILE PRESSURE — PRESS (IN MPA), TIME (IN MS)

(d). PROJECTILE DISPLACEMENT — DISP (IN CM), TIME (IN MS)
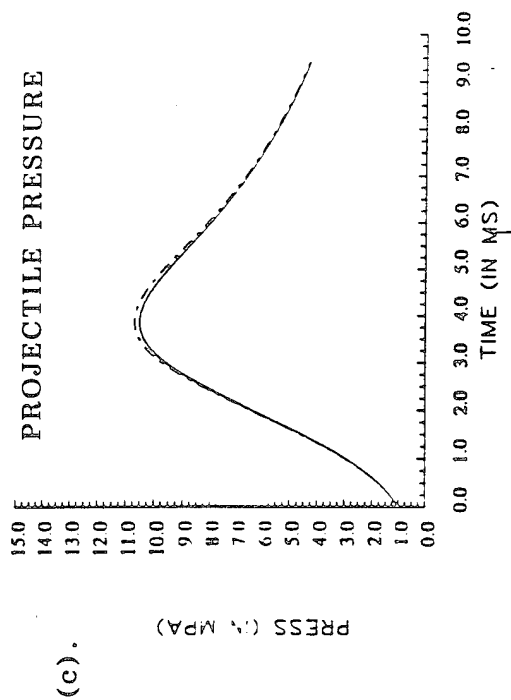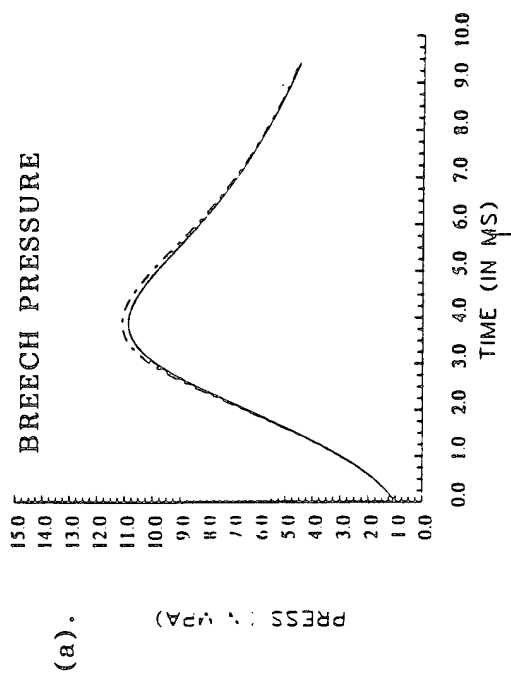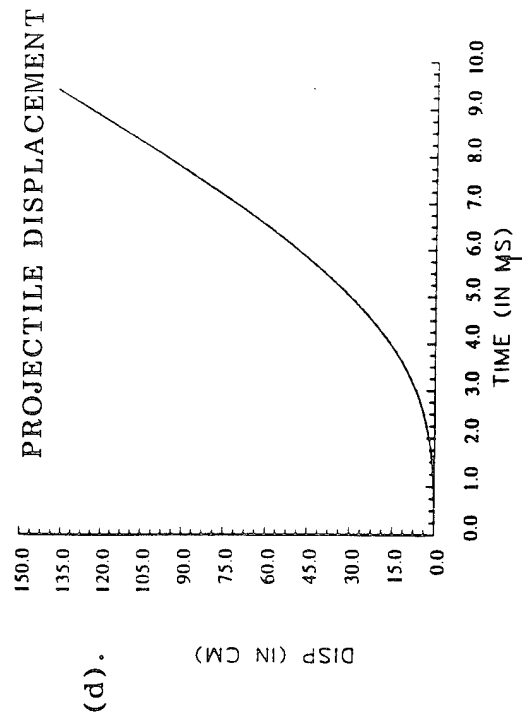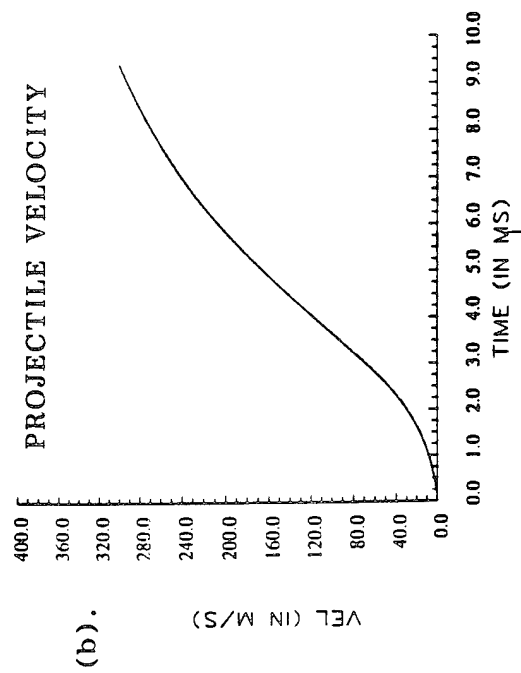
CRAFT
XKTC

Fig. 6.4.2.2.1. 1-D gun tube calculation for 0.1 g/cc loading case: Pressure History and gun performance compared for CRAFT and XKTC solutions.

108
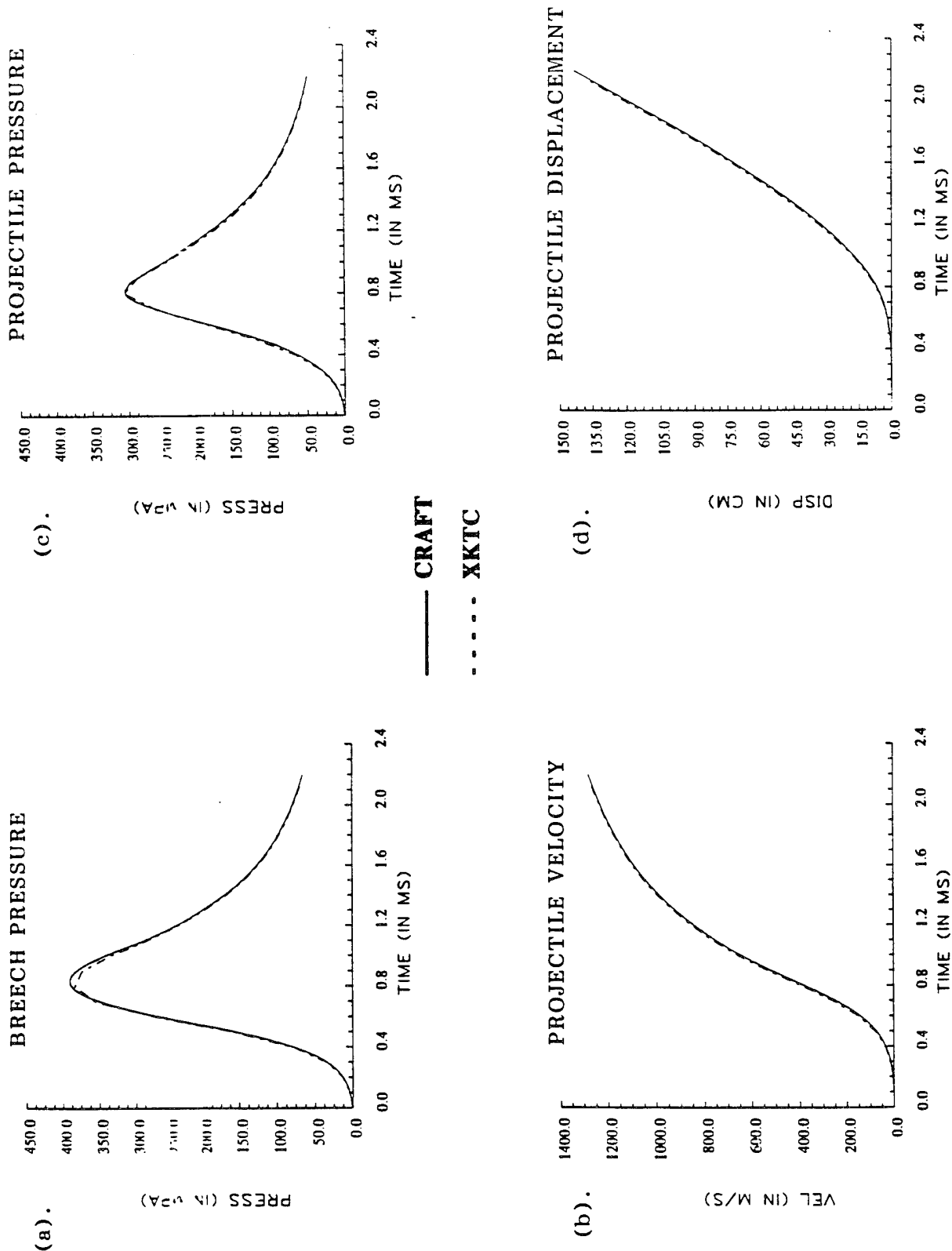
Fig. 6.4.2.2.2. 1-D gun tube calculation for 0.75 g/cc loading case: Pressure history and gun performance compared for CRAFT and XKTC Solutions.

109

remarkably well even for this high loading case. The peak breech pressure is around 370 MPa. The pressure profile for the XKTC solution shows minor kinks around the peak, but this can probably be eliminated by increased grid resolution. The projectile velocity and displacement compare very well with the projectile exit velocity being approximately 1225 m/s.

6.4.2.3 Multi-Dimensional ETC Gun Calculation With Plasma Injection

Having validated the Lagrangian formulation in CRAFT for 1-D calculations, we simulated a representative ETC/SP configuration to demonstrate the versatility of the Lagangian formulation in handling complex multi-dimensional flows with significant spatial variations. The gun chamber geometry is identical to that used in earlier validation studies with XKTC; it is cylindrical with a diameter of 30 mm and has a volume of 141 cc. The average propellant loading in the chamber is 0.75 g/cc. However, this propellant is loaded only in the top half of the chamber, and therefore the local propellant loading is above 1.0 g/cc. The central portion of the gun chamber contains an ullage tube into which plasma is pumped in eventually causing the tube to rupture and thereby allowing the plasma to mix with the propellant bed. As we shall describe in the following paragraph, the Lagrangian formulation in CRAFT allows us to study the complex process of propellant bed deconsolidation and fluidization.

Figures 6.4.2.3.1a and 1b show the porosity and log temperature contours at 0.36 ms. The temperature plot shows that the plasma, at this time, is generally limited to the central core of the chamber except at the projectile end where it reflects back in the form of a spherical wave. The reflection of the plasma from the projectile end is reflected in the porosity contours of the propellant bed which indicate that the bed deforms to accommodate the plasma. The propellant bed also shows a slight bulge at the inflow end where the high pressure plasma is trying to expand out against the propellant bed. The corresponding temperature and porosity contours at 0.61 and 0.86 ms are shown in Figs. 6.4.2.3.2 and 6.4.2.3.3 respectively. At 0.61 ms, the deconsolidation and fluidization of the propellant bed become apparent. The propellant descends towards the center of the chamber and tries to follow the projectile which is accelerating forward. The non-equilibrium between the two phases is highlighted by the fact that the propellant lags the projectile. The log temperature contours show that the

temperature in most of the chamber has dropped considerably since substantial amounts of cool (relative to plasma temperatures) products are being produced by the burning propellant. Furthermore, the two-dimensional structure of the temperature contours indicate that some high temperature plasma is still present in the core as well as the projectile end. In fact at the projectile end, the heavy products being formed in the chamber push the much lighter plasma up all the way to the top wall. These effects continue to be evident at 0.86 ms (Fig. 6.4.2.3.3), at which point the projectile has traveled further ahead with most of the propellant already burnt.
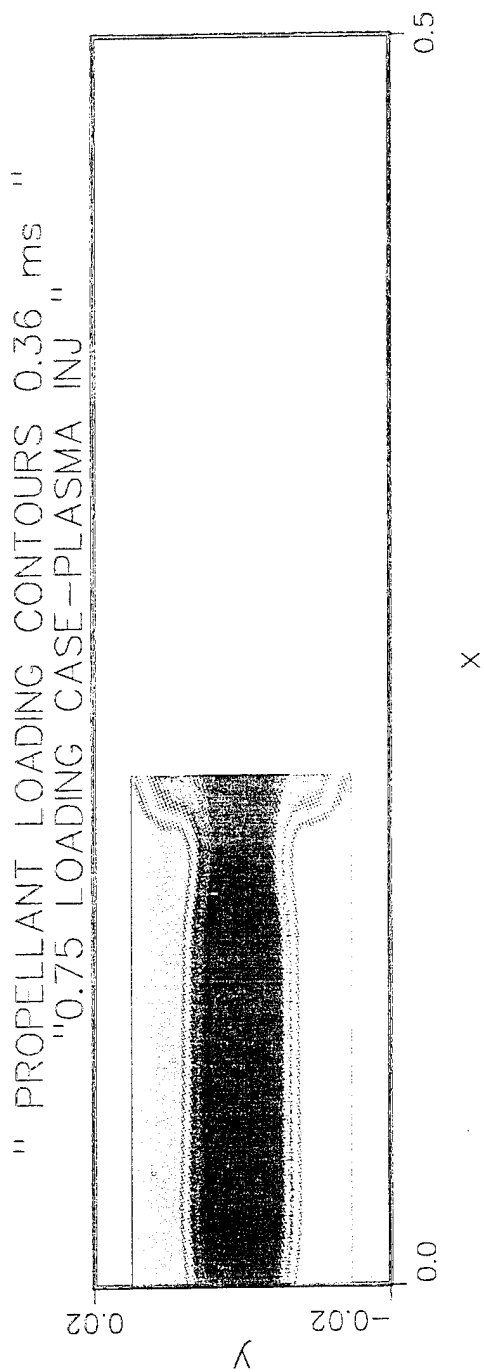
Fig. 6.4.2.3.1a. 2-D gun tube calculation with plasma injection for
0.75 loading case at 0.36ms: Loading density contours.

Fig. 6.4.2.3.1b. 2-D gun tube calculation with plasma injection for 0.75 loading case at 0.36ms: Log temperature contours.

113

" PROPELLANT LOADING CONTOURS 0.61 ms "
"0.75 LOADING CASE-PLASMA INJ "
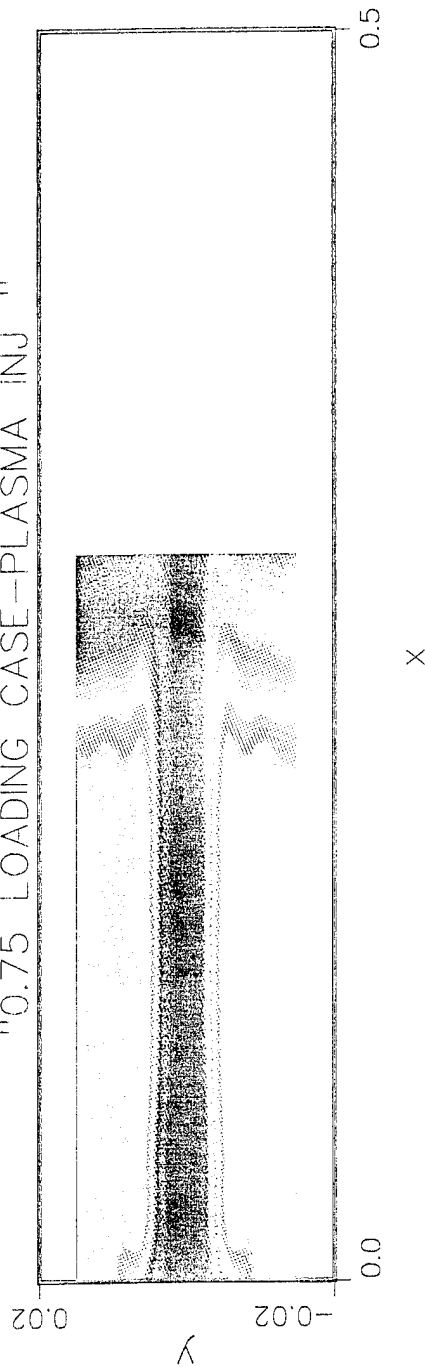
Fig. 6.4.2.3.2a.   2-D gun tube calculation with plasma injection for
0.75 loading case at 0.61ms: Loading density contours.

CONTOUR LEVELS
-0.01000
0.00000
0.01000
0.02000
0.03000
0.04000
0.05000
0.06000
0.07000
0.08000
0.09000
0.10000
0.11000
0.12000
0.17000
0.18000
0.19000
0.20000
0.21000
0.22000
0.23000
0.24000
0.25000
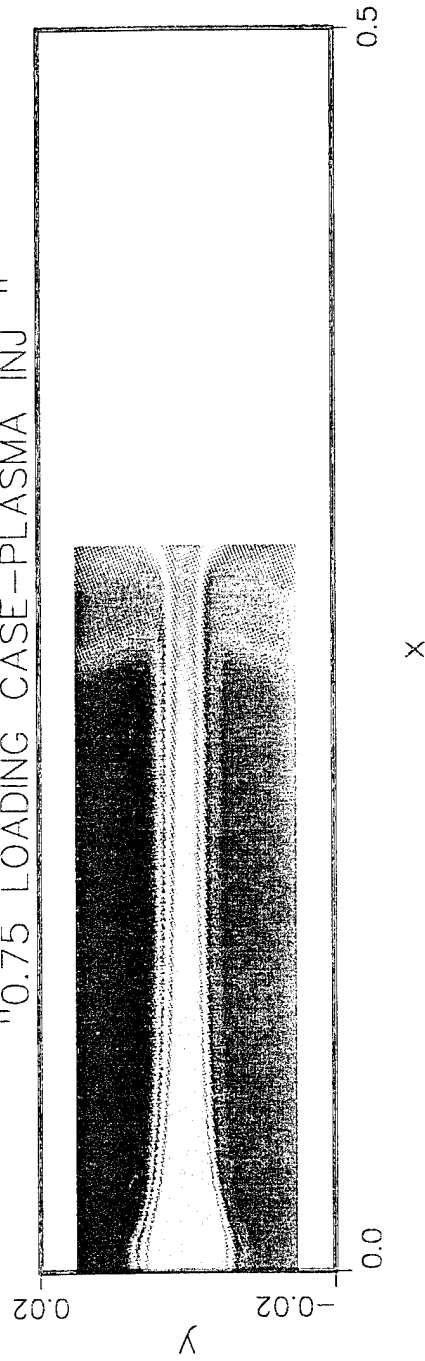
Fig. 6.4.2.3.2b. 2-D gun tube calculation with plasma injection for 0.75 loading case at 0.61ms: Log temperature contours.

115

"PROPELLANT LOADING CONTOURS 0.86 ms"
"0.75 LOADING CASE—PLASMA INJ"

CONTOUR LEVELS
-0.00250
0.00000
0.00250
0.00500
0.00750
0.01000
0.01250
0.01500
0.01750
0.02000
0.02250
0.02500
0.02750
0.03000
0.03250
0.03500
0.03750
0.04000
0.04250
0.04500
0.04750
0.05000
0.05250
0.05500
0.05750
0.06000
0.06250
0.06500
0.06750
0.07000
0.07250
0.07500
0.07750
0.08000
0.08250
0.08500
0.08750
0.09000
0.09250
0.09500
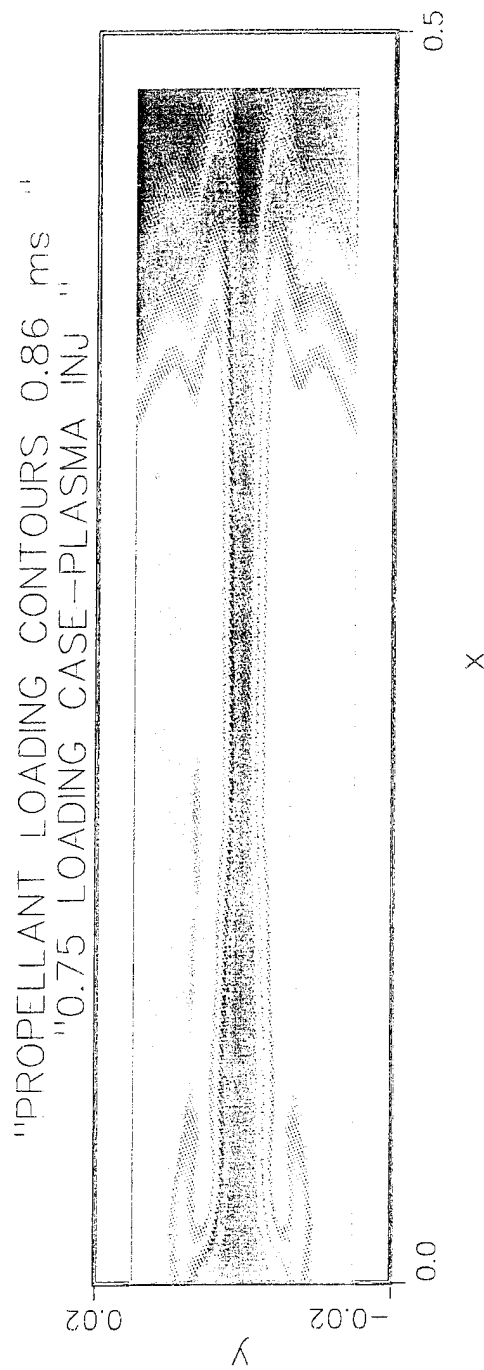
Fig. 6.4.2.3.3a. 2-D gun tube calculation with plasma injection for 0.75 loading case at 0.86ms: Loading density contours.

116

"LOG TEMPERATURE CONTOURS 0.86 ms"
"0.75 LOADING CASE – PLASMA INJ"
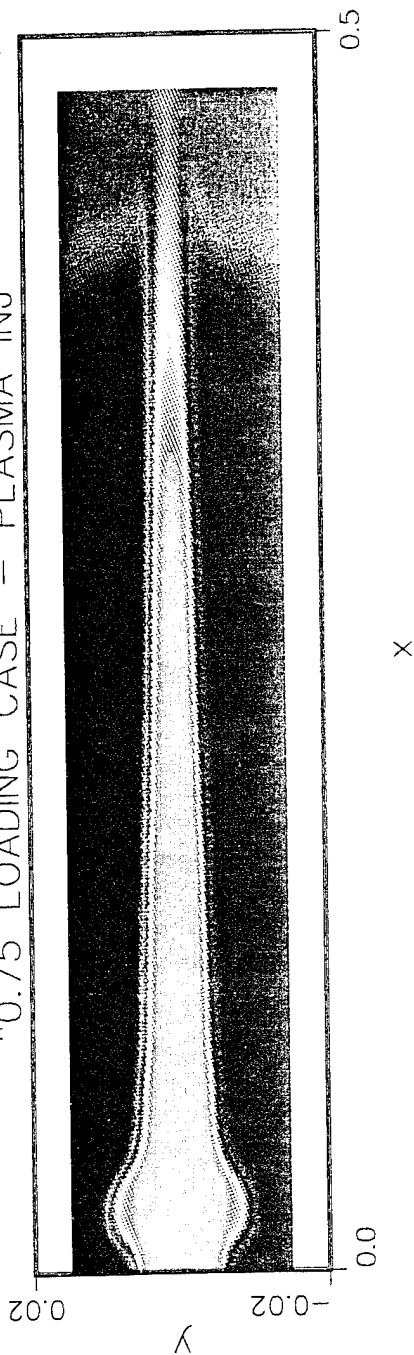
Fig. 6.4.2.3.3b. 2-D gun tube calculation with plasma injection for 0.75 loading case at 0.86ms: Log temperature contours.

CONTOUR LEVELS
-0.80000
-0.77500
-0.75000
-0.72500
-0.70000
-0.67500
-0.65000
-0.62500
-0.60000
-0.57500
-0.55000
-0.52500
-0.50000
-0.47500
-0.45000
-0.42500
-0.40000
-0.37500
-0.35000
-0.32500
-0.30000
-0.27500
-0.25000

-3.6304$3*10^{-14}$
0.02500
0.05000
0.07500
0.10000
0.12500
0.15000
0.17500
0.20000
0.22500
0.25000
0.27500
0.30000

117

7.0 FUTURE DIRECTION

The ETC gun simulation modeling described in this report has provided an enhanced level of understanding of fundamental processes in liquid and solid propellant interior ballistics. The sophisticated upwind/implicit computational framework utilized in CRAFT has provided the ability to capture strong discontinuities in a non-oscillatory manner, and, to treat acoustic disturbances with minimal numerical attenuation. The upwind/implicit framework has been systematically extended to include advanced thermochemical features (virial EOS, liquid EOS, gas/liquid equilibrated formulation) and Eulerian and Lagrangian dispersed-phase solutions applicable to both liquid droplet and solid particle analyses. The gas-phase equations have been extended to account for particle/droplet volumetric effects and the Lagrangian formulation was utilized to simulate packed-bed solid propellant interior ballistic flows with great success.

In its present form, CRAFT has all the necessary ingredients for the generalized analysis of liquid and solid propellant interior ballistic flows. In addition to the ETC problems described in this report, ram accelerator (RAMAC) [25-28] and LPG [7] problems have been analyzed. Specialized grid methodology (dynamic gridding, patching/blanking and embedding procedures) and the utilization of LES procedures for representing the transient turbulent eddy structure are common to all the interior ballistic flowfields analyzed. Current work on extending CRAFT to utilize hybrid structured/unstructured grid procedures [78], and, on the improvement of subgrid stress models for combusting flows [79] will greatly enhance its basic framework.

For interior ballistic flows, future work should focus on thermochemical details and on coupling with thermal and structural solvers to obtain accurate transient boundary conditions incorporating wall temperature variations and vibrations. The thermochemical work must focus on first-principles methodology to replace heuristic modeling. For liquid propellant problems, the details of what actually occurs at the gas/liquid interface has not been modeled. There is a need to focus on the droplet formation problem from a first-principles viewpoint since the mechanism relates directly to dynamic aspects of large eddy motion at the interface, which is being directly simulated using LES methodology. In proposed work for ERDEC re-

118

lated to bulk liquid flyout/breakup, a first-principles investigation of this problem will be initiated which is of direct relevance to liquid propellant IB flows.

For solid propellant IB flows, the Lagrangian framework provides generality but is numerically complex. Automated procedures to control the number of particles that must be tracked, and, improved numerics to deal with smoothing cell-to-cell transitions of particles and in-cell averaging procedures are required. In addition, a first-principles approach to deal with particle/particle collisions is needed to eliminate ad hoc "fluidized-bed" extensions to conventional drag/heat transfer laws.

8.0 REFERENCES

[1] Dash, S.M., Sinha, N., York, B.J. and Lee, R.A., "Progress in the Development of Advanced Computational Models for the Analysis of Generalized Supersonic Jet Flowfields," *AIAA 13th AeroAcoustics Conference*, AIAA-90-3915, Tallahassee, FL, October 1990.

[2] Dash, S.M., "Advanced Computational Models for Analyzing High-Speed Propulsive Flowfields," *1990 JANNAF Propulsion Mtg.*, CPIA Pub. 550, Vol. I, October 1990, pp. 247-284.

[3] Molvik, G.A. and Merkle, C.L., "A Set of Strongly Coupled, Upwind Algorithms for Computing Flows in Chemical Nonequilibrium," AIAA-89-0199, 27th Aerospace Sciences Mtg., Jan. 9-12, 1989.

[4] Palaniswamy, S. and Chakravarthy, S.R., "Finite-Rate Chemistry for USA Series Codes: Formulation and Applications," AIAA-89-0200, 27th Aerospace Sciences Mtg., Jan. 9-12, 1989.

[5] Walters, R.W., Slack, D.C., Cinnella, P., Applebaum, M., and Frost, C., "A User's Guide to GASP," Virginia Polytechnic Institute and State University, Dept. of Aerospace & Ocean Eng., NASA Langley Research Center, Hampton, VA, November 1990.

[6] Ridder, J.P. and Beddini, R.A., "Temporal and Acoustic Accuracy of an Implicit Upwind Method," *AIAA J.*, November 1991, pp. 1860-1867.

[7] Madabhushi, R.K., Hosangadi, A., Sinha, N., and Dash, S.M., "Large Eddy Simulation Studies of Vortex-Shedding with Application to LPG Instabilities Using the CRAFT Navier-Stokes Code," Science Applications International Corporation, SAIC/FW TR-120 (Final Report in preparation for ARL).

[8] Hosangadi, A., Sinha, N. and Dash, S.M., "Solution of the 1D/2D/3D Unsteady Particle-Cloud Equations Using Conservative Implicit/Upwind Numerics," prepared for MICOM, SAIC/FW TR-89, December 1990.

[9] Sinha, N., Hosangadi, A. and Dash, S.M., "The CRAFT NS Code and Preliminary Applications to Steady/Unsteady Reacting, Multi-Phase Jet/Plume Flowfield Problems," *19th JANNAF Exhaust Plume Technology Meeting*, CPIA Pub. 568, May 1991, pp. 203-226.

[10] Hosangadi, A., Sinha, N., Dash, S.M., "Solution of Two-Phase Dilute Gas Particle Mixtures Using Upwind Finite-Volume Methodology," AIAA-92-0344, *AIAA 30th Aerospace Sciences Meeting*, Reno, NV, January 6-9, 1992.

[11] Sinha, N., Dash, S.M., and Hosangadi, A., "Applications of an Implicit, Upwind NS Code, CRAFT, to Steady/Unsteady Reacting, Multi-Phase Jet/Plume Flowfields," AIAA Paper 92-0837, *AIAA 30th Aerospace Sciences Meeting*, Reno, NV, January 6-9, 1992.

[12] Dash, S.M., York, B.J., and Kenzakowski, D.C., "Simulation of Complete Tactical Missile Nozzle/Plume/Hardbody Flowfields for Signature Predictions," *1st JANNAF SPIRITS Users Group Meeting*, U.S. Army Missile Command, Huntsville, AL, 17-18 June, 1992.

[13] B.J. York, N. Sinha, S.M. Dash, A. Hosangadi, D.C. Kenzakowski, and R.A. Lee, "Complete Analysis of Steady and Transient Missile Aerodynamic/Propulsive/Plume Flowfield Interactions," AIAA-92-3603, *AIAA/SAE/ASME/ASEE 28th Joint Propulsion Conf.*, Nashville, TN, July 6-8, 1992.

[14] Sinha, N., Hosangadi, A., York, B.J., and Dash, S.M., "Recent Advances in the Simulation of Transient, Combusting, Multi-Phase Plume-Related Flowfields," *20th JANNAF Exhaust Plume Technology Subcommittee Meeting*, Phillips Lab., Kirtland AFB, NM, February 9-11, 1993.

[15] Dash, S.M., York, B.J., Lee, R.A., Sinha, N., and Madabhushi, R.K., "Advances in Three-Dimensional Plume Signature Simulation – Part I: Fluid Dynamic Codes and Applications," EOATMUM93, Arnold Engineering & Development Center, Arnold AFB, TN, Oct. 26-28, 1993.

[16] Dash, S.M., Kenzakowski, D.C., York, B.J., Walker, B.J., and Mikkelsen, C., "Advanced Computational Simulation of Solid Propellant Ducted Rocket Flowfields and Design-related Issues," 30th JANNAF Combustion Mtg., Monterey, CA Nov. 15-19, 1993.

[17] Sinha, N., York, B.J., Hosangadi, A., Madabhushi, R.K., and Dash, S.M., "Spatial/Temporal Incompatibilities in CRAFT Navier-Stokes Code Analysis of Turbulent, Chemically-Reacting, Multi-Phase Missile/Plume Flowfields," Final Report, Science Applications International Corp., Fort Washington, PA, SAIC/FW TR-117, January 1994.

[18] Dash, S.M., Lee, R.A., Sinha, N., and York, B.J., "Three-Dimensional End-to-End Simulation of Missile Plume/Aerodynamic Flowfields: Part 1 – Methodology & Status," JANNAF 21st Exhaust Plume Technology Subcommittee Mtg., Lockheed Missiles and Space Company, Sunnyvale, CA, Oct. 17-21, 1994.

120

[19] York, B.J., Madabhushi, R. K., Dash, S.M., Najarian, M.A., and Pergament, H.S., "Three-Dimensional End-to-End Simulation of Missile Plume/Aerodynamic Flowfields: Part 2 – Titan Studies," JANNAF 21st Exhaust Plume Technology Subcommittee Mtg., Lockheed Missiles and Space Company, Sunnyvale, CA, Oct. 17-21, 1994.

[20] Dash, S.M., Walker, B.J., Kessel, P., Moore, G., and Wilmoth, R.G.; "Plume Flowfield Architecture Program – Overview," JANNAF 21st Exhaust Plume Technology Subcommittee Mtg., Lockheed Missiles and Space Company, Sunnyvale, CA, Oct. 17-21, 1994.

[21] York, B.J., Sinha, N., Dash, S.M., Anderson, L., Gominho, L., "Navier-Stokes Simulation of Plume/Vertical Launching System Interaction Flowfields," AIAA 92-0839, *AIAA 30th Aerospace Sciences Meeting*, Reno, NV, January 6-9, 1992.

[22] York, B.J., Hosangadi, A., Kenzakowksi, D.C., Dash, S.M., Anderson, L., Gominho, L., and Koo, J., "Steady and Transient Navier-Stokes Simulation of Exhaust Plume/Launcher Interactions," *20th JANNAF Exhaust Plume Technology Subcommittee Meeting*, Phillips Lab., Kirtland AFB, NM, February 9-11, 1993.

[23] Miller, M.J, Koo, J.H., Sickler, F.M., LeCureux, F., and Dash, S.M., "Effect of Water to Ablative Performance Under Solid Rocket Exhaust Environment," AIAA-93-2475, 29th Joint Propulsion Conf., June 28-30, 1993.

[24] York, B.J., Sinha, N., Dash, S.M., Anderson, L., Gominho, L., and Koo, J., "Steady/Transient Plume-VLS Interactions and Advances in Particulate/Surface Layer Modeling," JANNAF 21st Exhaust Plume Technology Subcommittee Mtg., Lockheed Missiles and Space Company, Sunnyvale, CA, Oct. 17-21, 1994.

[25] Sinha, N., York, B.J., Dash, S.M., Drabczuk, and R., Rolader, G.E., "Progress Towards the Development of Transient Ram Accelerator Simulation As Part of U.S. Air Force Armament Directorate Research Program," AIAA-92-3248, *AIAA/SAE/ASME/ASEE 28th Joint Propulsion Conf.*, Nashville, TN, July 6-8, 1992.

[26] Sinha, N., York, B.J., Dash, S.M., Drabczuk, R., and Rolader, G.E., "Transient Simulation of Ram Accelerator Flowfields," *29th JANNAF Combustion Meeting*, 19-23 Oct. 1992.

[27] Dash, S.M., Sinha, N., and York, B.J., "Modeling Requirements and Scaling Issues for Ram Accelerator Flowfield Simulation," SAIC/FW TP-280, First Int'l. Workshop on Ram Accelerator (RAMAC), French-German Research Institute of Saint-Louis, France, Sept. 7-10, 1993.

[28] Sinha, N., York, B.J., Madabhushi, R.K., and Dash, S.M., "Sensitivity Studies to Establish Modeling Requirements and Explore Scaling Issues for Ram Accelerator Flowfield Simulation," 30th JANNAF Combustion Mtg., Monterey, CA Nov. 15-19, 1993.

[29] Sinha, N., Dash, S.M. and York, B.J., "Predictions of Jet Mean-Flow Structure in Support of HSCT Noise-Suppression Concepts," *AIAA/SAE/ASME/ASEE 27th Joint Propulsion Conference*, AIAA-91-2253, Sacramento, CA, June 24-26, 1991.

[30] Dash, S.M., Sinha, N., York, B.J., Kenzakowski, D.C., and Lee, R.A., "Computer Codes for HSCT Exhaust Flowfield Simulation and Observations on Turbulence Modeling," AIAA-91-3297, *9th AIAA Applied Aerodynamics Conference*, Baltimore, MD, September 23-26, 1991.

[31] Dash, S.M., "Flow Predictions in Supersonic Jets - Invited Survey," DGLR/AIAA 92-02-063, *DGLR/AIAA 14th AeroAcoustic Conference*, Aachen, Germany, May 11-14, 1992.

[32] Dash, S.M., "Status on Numerical Computation of Supersonic Jet Plume," invited presentation at *First NASA/Industry High-Speed Research Symposium*, November 17-19, 1992.

[33] Dash, S.M. and Sinha, N., "The Computational Simulation of Supersonic Jet Flowfields for Aerodynamic Noise Control," invited presentation at *NOISE-93: International Conference on Noise and Vibration Control*, St. Petersburg, Russia, May 31-June 3, 1993.

[34] Dash, S.M., Sinha, N., Madabhushi, R.K., Lee, R.A., York, B.J., and Hosangadi, A., "Progress in the Unsteady Simulation of Jet Flowfields," AIAA-93-1921, *29th Joint Propulsion Conf.*, June 28-30, 1993.

[35] Sinha, N., Dash, S.M., and Madabhushi, R.K., "Recent Advances in Jet Flowfield Simulation: Part II - Unsteady Flows," AIAA 93-4391, *15th AIAA Aeroacoustics Conf.*, Long Beach, CA, Oct. 25-27, 1993.

[36] Sinha, N. and Dash, S.M., "Unsteady LES Simulation of Jets/Free Shear Flows Using Structured/Unstructured Upwind Numerics," *JANNAF 21st Exhaust Plume Technology Subcommittee Mtg.*, Lockheed Missiles and Space Company, Sunnyvale, CA, Oct. 17-21, 1994.

[37] Dash, S.M. and Kenzakowski, D.C., "Hot Jet/Wake Turbulent Structure and Laser Propagation: Part I – Jet/Wake Turbulence Modeling," *JANNAF 21st Exhaust Plume Technology Subcommittee Mtg.*, Lockheed Missiles and Space Company, Sunnyvale, CA, Oct. 17-21, 1994.

[38] Lee, R.A. and Dash, S.M., "Advances in 3D Modeling or Aircraft and Helicopter Aerodynamic/Exhaust Flows for Signature Predictions," *JANNAF 3rd SPIRITS Users Group Mtg.*, Lockheed Missiles and Space Company, Sunnyvale, CA, Oct. 17-21, 1994.

[39] Wren, G.P. and Hosangadi, A., "Fundamental Comparative Studies of Solid Propellant Interior Ballistic Flows Using XKTC and CRAFT," *JANNAF 31st Combustion Subcommittee Meeting*, Lockheed Missiles and Space Company, Sunnyvale, CA, Oct. 17-21, 1994.

[40] Sinha, N., Hosangadi, A. and Dash, S.M., "Development of an Upwind/Implicit Computational Model for the Advancement of Army ETC Guns," *ETC Modeling and Diagnostics Workshop Proceedings*, Vol. 2, BRL SP-92, U.S. Army Ballistic Research Laboratory, Aberdeen Proving Ground, MD, October 1991.

[41] Sinha, N., A. Hosangadi, and Dash, S.M., "Simulation of ETC Gun Phenomena Using CRAFT Implicit/Upwind Computer Code," *28th JANNAF Combustion Meeting*, Brooks AFB, San Antonio, TX, Oct. 28 - Nov. 1, 1991.

[42] Wren, G.P., Oberle, W.F., Sinha, N., Hosangadi, A., and Dash, S.M., "U.S. Army Activities in Multidimensional Modeling of Electrothermal-Chemical Guns," *IEEE Conf., Electromagnetic Launcher Symposium*, Austin, TX, April 28-30, 1992.

[43] Hosangadi, A., Sinha, N., and Dash, S.M., "CRAFT Code Multi-Dimensional Simulation of ETC Interior Ballistics," *29th JANNAF Combustion Meeting*, 19-23 Oct. 1992.

[44] Hosangadi, A., Sinha, N., and Dash, S.M., "Numerical Studies of ETC Gun Barrel Blow-Down Using the CRAFT Code," SAIC/FW TM-71, January 1993.

[45] Hosangadi, A., Sinha, N., and Dash, S.M., "Progress in Multi-Dimensional ETC Modeling and Flowfield Simulation," *Workshop on ETC Technology*, Army Research Lab., Aberdeen Proving Ground, MD, Oct. 4-7, 1993.

[46] Hosangadi, A., Sinha, N., Madabhushi, R.K., Dash, S.M., "Multi-Dimensional Simulation of Liquid and Solid Propellant ETC Gun Interior Ballistic Flowfields," *30th JANNAF Combustion Mtg.*, Monterey, CA Nov. 15-19, 1993.

[47] Hosangadi, A., Sinha, N., and Dash, S.M., "CRAFT Code Solid Propellant ETC Gun Simulation via Lagrangian Fluidized Bed Extensions," *JANNAF 31st Combustion Subcommittee Mtg.*, Lockheed Missiles and Space Company, Sunnyvale, CA, Oct. 17-21, 1994.

[48] Dash, S.M., "Unified Three-Dimensional Model for Conventional and Hypervelocity Interior Ballistic Flowfields, CRAFT/IB – Status and Future Direction," *JANNAF 31st Combustion Subcommittee Mtg.*, Lockheed Missiles and Space Company, Sunnyvale, CA, Oct. 17-21, 1994.

[49] Roe, P.L., "Approximate Reimann Solvers, Parameter Vectors, and Difference Schemes," *Journal of Computational Physics*, 43 (1983) pp. 357-372.

[50] Chakravarthy, S.R. and Osher, S., "A New Class of High Accuracy TVD Schemes for Hyperbolic Conservation Laws," AIAA-85-0363, Reno, NV, January 1985.

[51] Rai, M.M., "Navier-Stokes Simulation of Rotor-Stator Interaction Using Patched and Overlaid Grids," AIAA-85-1519, Cincinnati, OH, 1985.

[52] Launder, B.E., Morse, A., Rodi, W., and Spalding, D.B., "Prediction of Free Shear Flows: A Comparison of Six Turbulence Models, " Free Turbulent Shear Flows, Vol. I, NASA SP-321, July 1972, pp. 361-426.

[53] Chien, K.Y., "Predictions of Channel and Boundary Layer Flows with a Low Reynolds Number Turbulence Model, " *AIAA J.*, January 1982, pp. 33-38.

[54] Erlebacher, G., Hussaini, M.Y., Speziale, C.G., and Zang, T.A., "Toward Large Eddy Simulation of Compressible Turbulent Flows, *J. of Fluid Mech.*, Vol. 283, 1992.

[55] Menon, S., "A Numerical Study of Secondary Fuel Injection Techniques for Active Control of Combustion Instability in a Ramjet," AIAA-92-0777, January 1992.

[56] Smagorinsky, J., "General Circulation Experiments with the Primitive Equations," *Mon. Weather Rev.*, (1963), Vol. 91, pp. 99-164.

[57] Liu, K. and Vinokur, M., "Upwind Algorithms for General Thermo-Chemical Nonequilibrium Flows," AIAA-89-0201, January 1989.

[58] Cooper, G.K. and Sirbaugh, J., "The PARC Distinction: A Practical Flow Simulator," AIAA-90-2002, July 1990.

122

[59] Lehr, H.F., "Experiments on Shock-Induced Combustion," *Astronautica Acta*, Vol. 17, Nos. 4&5, 1972, pp. 589-596.

[60] Wilson, G. J. and Sussman, M.A., "Computation of Unsteady Shock-Induced Combustion Using Logarithmic Species Conservation Equations," AIAA Journal, Vol. 31, No. 2, Feb. 1993, pp. 294-301.

[61] Sussman, M.A., "Source Term Evaluation for Combustion Modeling," AIAA-93-0239, Reno, NV, January 1993.

[62] Evans, J.S. and Schexnayder, C.J., Jr., "Critical Influence of Finite-Rate Chemistry and Unmixedness on Ignition and Combustion of Supersonic H_2/Air Streams," AIAA 79-0355, January 1979.

[63] Jachimowski, C.J., "An Analytical Study of the Hydrogen-Air Reaction Mechanism with Application to Scramjet Combustion," NASA TP-2791, Feb. 1988.

[64] Davies, C.B. and Venkatapathy, E., "The Multi-Dimensional Self-Adaptive Grid Code, SAGE," NASA Technical Memorandum 103905, July, 1992.

[65] Brown, G.L. and Roshko, A., On Density Effects and Large Structure in Turbulent Mixing Layers, " *J. Fluid Mechanics*, Vol. 64, 1974, pp. 775-816.

[66] Chien, K.Y., Ferguson, R.E., Kuhl, A.L., Glaz, H.M., and Colella, P., "Inviscid Dynamics of Two-Dimensional Shear Layers," AIAA-91-1678, June 1991.

[67] Kuo, K. and Cheung, F-B, "Droplet Entrainment and Breakup by Shear Flows," 30th JANNAF Combustion Mtg., Monterey, CA, 1993.

[68] Coffee, T.P., "Modeling of Pressure Oscillations in Liquid Propellant Guns, 28th JANNAF Combustion Mtg., Brooks AFB, San Antonio, TX, Oct. 28-Nov. 1, 1991.

[69] Freedman, E., personal communication, Eli Freedman Assoc., Baltimore, MD, May 1992.

[70] Powell, J.D. and Zielinski, A.E., "Theory and Experiment for an Ablating-Capillary Discharge and Applications to Electrothermal-Chemical Guns," Ballistic Research Laboratory Report BRL-TR-3355, July 1992.

[71] Gilligan, J.G., Bourham, M.A., and Hankins, O.E., "Ablation and Melting Behavior of Materials and Electrothermal Launchers," 28th JANNAF Combustion Mtg., Brooks AFB, San Antonio, TX, Oct. 28-Nov. 1, 1991.

[72] Tissier, P.Y, Godfroy, F. and Jacquemin, P., "Simulation of 3-D Flows Inside Solid Propellant Rocket Motors Using 2nd-Order Finite Volume Method: Applications to the Study of Unstable Phenomena," AIAA-92-3275, July 1992.

[73] Keith, J.C. and Banks, N., "Hypervelocity Impact and Aerodynamic Breakup of Liquids," Journal of Impact Engineering, Vol. 10, 1990, pp. 309-322.

[74] Gough, P.S., "Two-Dimensional Convective Flame Spreading in Pack Beds of Granular Propellant," Ballistic Research Laboratory Report, ARBRL-CR-00404, July 1979.

[75] Becker, E. and Gert, B., "Steady One-Dimensional Flow: Structure of Compression Waves," Non-equilibrium Flows: Part I, Ed. Peter P. Wegener, Marcel Dekker, 1969, pp. 71-116.

[76] Gough, P.S., "The NOVA Code: A User's Manual," Final Report, Task I, Contract N00174-79-C-0082, 1979.

[77] Love, A.E.A. and Pidduck, F.B., "Lagrange Ballistic Problem," *Phil. Trans. Roy. Soc.*, Vol. 222, pp. 167-226, 1921-22.

[78] Hosangadi, A., Lee, R.A., York, B.J., Sinha, N., and Dash, S.M., "Advances in Unstructured Grid Methodology for High-Speed Propulsive Problems," submitted for presentation at 33rd AIAA Aerospace Sciences Meeting and Exhibit, Reno, NV, January 9-12, 1995.

[79] Sinha, N., Madabhushi, R.K., Dash, S.M., and Menon, S., "Large Eddy Simulation of Reacting Flows," submitted for presentation at JANNAF 31st Combustion Subcommittee Mtg., Lockheed Missiles and Space Company, Sunnyvale, CA, Oct. 17-21, 1994.

INTENTIONALLY LEFT BLANK.

APPENDIX A

INVISCID FLUX JACOBIAN FOR GAS-LIQUID EQUILIBRIUM FORMULATION*

$$\hat{A} = \begin{bmatrix}
0 & \ell_x & \ell_y & \ell_z & 0 & 0 & 0 & \cdots & 0 \\[2mm]
-Uu+\ell_x\dfrac{\partial p}{\partial \rho} & U+\ell_x u+\ell_x\dfrac{\partial p}{\partial \rho u} & \ell_y u+\ell_x\dfrac{\partial p}{\partial \rho v} & \ell_z u+\ell_x\dfrac{\partial p}{\partial \rho w} & \ell_x\dfrac{\partial p}{\partial e} & \ell_x\dfrac{\partial P}{\partial \rho_1} & \ell_x\dfrac{\partial p}{\partial \rho_2} & \cdots & \ell_x\dfrac{\partial p}{\partial \rho_{n-1}} \\[2mm]
-Uv+\ell_y\dfrac{\partial p}{\partial \rho} & \ell_x v+\ell_y\dfrac{\partial p}{\partial \rho u} & U+\ell_y v+\ell_y\dfrac{\partial p}{\partial \rho v} & \ell_z v+\ell_y\dfrac{\partial p}{\partial \rho w} & \ell_y\dfrac{\partial p}{\partial e} & \ell_y\dfrac{\partial p}{\partial \rho_1} & \ell_y\dfrac{\partial p}{\partial \rho_2} & \cdots & \ell_y\dfrac{\partial p}{\partial \rho_{n-1}} \\[2mm]
-Uw+\ell_z\dfrac{\partial p}{\partial \rho} & \ell_x w+\ell_z\dfrac{\partial p}{\partial \rho u} & \ell_y w+\ell_z\dfrac{\partial p}{\partial \rho v} & U+\ell_z w+\ell_z\dfrac{\partial p}{\partial \rho w} & \ell_z\dfrac{\partial p}{\partial e} & \ell_z\dfrac{\partial p}{\partial \rho_1} & \ell_z\dfrac{\partial p}{\partial \rho_2} & \cdots & \ell_z\dfrac{\partial p}{\partial \rho_{n-1}} \\[2mm]
-UH+\dfrac{\partial p}{\partial \rho}U & \ell_x H+U\dfrac{\partial p}{\partial \rho u} & \ell_y H+U\dfrac{\partial p}{\partial \rho v} & \ell_z H+U\dfrac{\partial p}{\partial \rho w} & \left(1+\dfrac{\partial p}{\partial e}\right)U & \dfrac{\partial p}{\partial \rho_1}U & \dfrac{\partial p}{\partial \rho_2}U & \cdots & \dfrac{\partial p}{\partial \rho_{n-1}}U \\[2mm]
-c_1 U & c_1\ell_x & c_1\ell_y & c_1\ell_z & 0 & U & 0 & \cdots & 0 \\[2mm]
c_2 U & c_2\ell_x & c_2\ell_y & c_2\ell_z & 0 & 0 & U & \cdots & 0 \\[2mm]
\vdots & \vdots & \vdots & \vdots & \vdots & \vdots & \vdots & \ddots & \vdots \\[2mm]
-c_{n-1}U & c_{n-1}\ell_x & c_{n-1}\ell_y & c_{n-1}\ell_z & 0 & 0 & 0 & \cdots & U
\end{bmatrix}$$

where ℓ_x, ℓ_y, ℓ_z represent the component of the cell face area in the ξ direction.

$\hat{U}$ is the contravariant velocity and is defined as

$$\hat{U} = \ell_x u + \ell_y v + \ell_z w$$

The derivatives appearing in the matrix are defined as follows:

$$\frac{\partial P}{\partial \rho} = -D_L + \frac{\bar{\gamma}-1}{2}\left(u^2+v^2+w^2\right)$$

$$\frac{\partial P}{\partial \rho u} = -(\bar{\gamma}-1)u$$

$$\frac{\partial P}{\partial \rho v} = -(\bar{\gamma}-1)v$$

$$\frac{\partial P}{\partial \rho w} = -(\bar{\gamma}-1)w$$

$$\frac{\partial P}{\partial e} = (\bar{\gamma}-1)$$

$$\frac{\partial P}{\partial(\phi_l \rho_i)} = (D_L - D_i) \Big\}\, for\ n-1\ gas\ species$$

_____

* Generalized $\hat{A}$ matrix formulation from Ref. 3.

Here,

$$D_L = (\tilde{\gamma}-1) h_L - \tilde{\gamma} C_L^2 \left[\frac{\sum\limits_{n-1} \rho_i C_i^{\,2}}{\phi_L \sum\limits_{n-1} \rho_i C_i^{\,2} + \phi_g \rho_L C_L^2} \right]$$

$$D_i = (\tilde{\gamma}-1) h_i - \tilde{\gamma} C_i^2 \left[\frac{\sum\limits_{n-1} \rho_L C_L^{\,2}}{\phi_L \sum\limits_{n-1} \rho_i C_i^{\,2} + \phi_g \rho_L C_L^2} \right] \Bigg\} \; \textit{for } n-1 \textit{ gas species}$$

ϕ_g =   volume fraction of gas

ϕ_L =   volume fraction of liquid

C_i = $\sqrt{\left(\dfrac{\partial P_g}{\partial \rho_i}\right)_T}$ =   isothermal speed of sound of ith gas species

C_L = $\sqrt{\left(\dfrac{\partial P_L}{\partial \rho_L}\right)_T}$ =   isothermal speed of sound of liquid

$\tilde{\gamma}$ = $\dfrac{\left(\sum\limits_{n-1} \rho_i \phi_g C_{P_i} + \rho_L \phi_L C_{P_L}\right)}{\left(\sum\limits_{n-1} \rho_i \phi_g C_{P_i} + \rho_L \phi_L C_{P_L}\right) - \beta_{\square}}$

$\beta_{\square}$ = $\left(\dfrac{\phi_g C_L^2 \rho_L}{\phi_L \sum\limits_{n-1} \rho_i C_i^{\,2} + \phi_g \rho_L C_L^2}\right) \dfrac{\partial P_g}{\partial T} + \left[\dfrac{\phi_L \sum\limits_{n-1} \rho_i C_i^{\,2}}{\phi_L \sum\limits_{n-1} \rho_i C_i^{\,2} + \phi_g \rho_L C_L^2}\right] \dfrac{\partial P_L}{\partial T}$

APPENDIX B

EIGENVALUES AND EIGENVECTORS FOR THE GAS-LIQUID FORMULATION*

The eigenvalues of the Jacobian A are represented as

$$\Lambda = DIAG. \ (U + C, \ U - C, \ U, \ \ldots, \ U)$$

$$U = \ell_x u + \ell_y v + \ell_z w$$

and

$$C = C \sqrt{\ell_x^2 + \ell_y^2 + \ell_z^2}$$

where C is the speed of sound and is defined as

$$C^2 = \frac{\tilde{\gamma}}{\rho} \left\{ \left[\frac{\phi_L \sum_{n-1} \rho_i C_i^2}{\phi_L \sum_{n-1} \rho_i C_i^2 + \phi_g \rho_L C_L^2} \right] \rho_L C_L^2 + \left[\frac{\phi_g \rho_L C_L^2}{\phi_L \sum_{n-1} \rho_i C_i^2 + \phi_g \rho_L C_L^2} \right] \sum_{n-1} \rho_i C_i^2 \right\}$$

here, C_i and C_L are the isothermal sound speeds for the ith gas species, and the liquid species, respectively.

The left and right eigenvectors are represented as follows

$$
L =
\begin{bmatrix}
\frac{(u^2+v^2+w^2)}{2} - \frac{c\hat{U}}{(\gamma-1)} - \frac{D_n}{(\gamma-1)} & -u+\frac{c\hat{\ell}_x}{(\gamma-1)} & -v+\frac{c\hat{\ell}_y}{(\gamma-1)} & -w+\frac{c\hat{\ell}_z}{(\gamma-1)} & 1 & \frac{D_n-D_1}{(\gamma-1)} & \frac{D_n-D_2}{(\gamma-1)} & \cdots & \frac{D_n-D_{n-1}}{(\gamma-1)} \\
\frac{(u^2+v^2+w^2)}{2} + \frac{c\hat{U}}{(\gamma-1)} - \frac{D_n}{(\gamma-1)} & -u-\frac{c\hat{\ell}_x}{(\gamma-1)} & -v-\frac{c\hat{\ell}_y}{(\gamma-1)} & -w-\frac{c\hat{\ell}_z}{(\gamma-1)} & 1 & \frac{D_n-D_1}{(\gamma-1)} & \frac{D_n-D_2}{(\gamma-1)} & \cdots & \frac{D_n-D_{n-1}}{(\gamma-1)} \\
-\hat{V} & \hat{m}_x & \hat{m}_y & \hat{m}_z & 0 & 0 & 0 & \cdots & 0 \\
-\hat{W} & \hat{n}_x & \hat{n}_y & \hat{n}_z & 0 & 0 & 0 & \cdots & 0 \\
\frac{(u^2+v^2+w^2)}{2} - h & -u & -v & -w & 1 & 0 & 0 & \cdots & 0 \\
-c_1 & 0 & 0 & 0 & 0 & 1 & 0 & 0 & 0 \\
-c_2 & 0 & 0 & 0 & 0 & 0 & 1 & 0 & 0 \\
\vdots & \vdots & \vdots & \vdots & \vdots & \vdots & \vdots & \ddots & \vdots \\
-c_{n-1} & 0 & 0 & 0 & 0 & 0 & 0 & 0 & 1
\end{bmatrix}
$$

* Generalized L and R matrix formulation from Ref. 3.

B-1

$$R = \begin{bmatrix}
\dfrac{(\gamma-1)}{2c^2} & \dfrac{(\gamma-1)}{2c^2} & 0 & 0 & \dfrac{-(\gamma-1)}{c^2} & \dfrac{(D_1-D_R)}{c^2} & \dfrac{(D_2-D_R)}{c^2} & \cdots & \dfrac{(D_{n-1}-D_R)}{c^2} \\[2ex]
\dfrac{(\gamma-1)u}{2c^2}+\dfrac{(\gamma-1)\hat{\ell}_x}{2c} & \dfrac{(\gamma-1)u}{2c^2}-\dfrac{(\gamma-1)\hat{\ell}_x}{2c} & \hat{m}_x & \hat{n}_x & \dfrac{-(\gamma-1)u}{c^2} & \dfrac{(D_1-D_R)u}{c^2} & \dfrac{(D_2-D_R)u}{c^2} & \cdots & \dfrac{(D_{n-1}-D_R)u}{c^2} \\[2ex]
\dfrac{(\gamma-1)v}{2c^2}+\dfrac{(\gamma-1)\hat{\ell}_y}{2c} & \dfrac{(\gamma-1)v}{2c^2}-\dfrac{(\gamma-1)\hat{\ell}_y}{2c} & \hat{m}_y & \hat{n}_y & \dfrac{-(\gamma-1)v}{c^2} & \dfrac{(D_1-D_R)v}{c^2} & \dfrac{(D_2-D_R)v}{c^2} & \cdots & \dfrac{(D_{n-1}-D_R)v}{c^2} \\[2ex]
\dfrac{(\gamma-1)w}{2c^2}+\dfrac{(\gamma-1)\hat{\ell}_z}{2c} & \dfrac{(\gamma-1)w}{2c^2}-\dfrac{(\gamma-1)\hat{\ell}_z}{2c} & \hat{m}_z & \hat{n}_z & \dfrac{-(\gamma-1)w}{c^2} & \dfrac{(D_1-D_R)w}{c^2} & \dfrac{(D_2-D_R)w}{c^2} & \cdots & \dfrac{(D_{n-1}-D_R)w}{c^2} \\[2ex]
\dfrac{(\gamma-1)\hat{U}}{2c}+\dfrac{(\gamma-1)H}{2c^2} & -\dfrac{(\gamma-1)\hat{U}}{2c}+\dfrac{(\gamma-1)H}{2c^2} & \hat{V} & \hat{W} & 1-\dfrac{(\gamma-1)H}{c^2} & \dfrac{(D_1-D_R)H}{c^2} & \dfrac{(D_2-D_R)H}{c^2} & \cdots & \dfrac{(D_{n-1}-D_R)H}{c^2} \\[2ex]
\dfrac{c_1(\gamma-1)}{2c^2} & \dfrac{c_1(\gamma-1)}{2c^2} & 0 & 0 & \dfrac{-c_1(\gamma-1)}{c^2} & 1+\dfrac{c_1(D_1-D_R)}{c^2} & \dfrac{c_1(D_2-D-n)}{c^2} & \cdots & \dfrac{c_1(D_{n-1}-D_R)}{c^2} \\[2ex]
\dfrac{c_2(\gamma-1)}{2c^2} & \dfrac{c_2(\gamma-1)}{2c^2} & 0 & 0 & \dfrac{-c_2(\gamma-1)}{c^2} & \dfrac{c_2(D_1-D_R)}{c^2} & 1+\dfrac{c_2(D_2-D_R)}{c^2} & \cdots & \dfrac{c_2(D_{n-1}-D_R)}{c^2} \\[2ex]
\vdots & \vdots & \vdots & \vdots & \vdots & \vdots & \vdots & \ddots & \vdots \\[2ex]
\dfrac{c_{n-1}(\gamma-1)}{2c^2} & \dfrac{c_{n-1}(\gamma-1)}{2c^2} & 0 & 0 & \dfrac{-c_{n-1}(\gamma-1)}{c^2} & \dfrac{c_{n-1}(D_1-D_R)}{c^2} & \dfrac{c_{n-1}(D_2-D_R)}{c^2} & \cdots & 1+\dfrac{c_{n-1}(D_{n-1}-D_R)}{c^2}
\end{bmatrix}$$

In the above eigenvectors $\hat{\ell} = \ell_x i + \ell_y j + \ell_z k$ is the normal of the cell face in the ξ direction. The vectors $\hat{m}$ and $\hat{n}$ are two arbitrary, mutually perpendicular vectors to the vector $\hat{\ell}$. The terms $\hat{U}$, $\hat{V}$, $\hat{W}$, are the dot product of the velocity vector with these three unit vectors.

NO. OF
COPIES   ORGANIZATION

2   ADMINISTRATOR
     ATTN DTIC DDA
     DEFENSE TECHNICAL INFO CTR
     CAMERON STATION
     ALEXANDRIA VA 22304-6145

1   DIRECTOR
     ATTN AMSRL OP SD TA
     US ARMY RESEARCH LAB
     2800 POWDER MILL RD
     ADELPHI MD 20783-1145

3   DIRECTOR
     ATTN AMSRL OP SD TL
     US ARMY RESEARCH LAB
     2800 POWDER MILL RD
     ADELPHI MD 20783-1145

1   DIRECTOR
     ATTN AMSRL OP SD TP
     US ARMY RESEARCH LAB
     2800 POWDER MILL RD
     ADELPHI MD 20783-1145

     ABERDEEN PROVING GROUND

5   DIR USARL
     ATTN AMSRL OP AP L (305)

NO. OF COPIES	ORGANIZATION	NO. OF COPIES	ORGANIZATION
1	OSD SDIO IST ATTN DR L CAVENY PENTAGON WASHINGTON DC 20301-7100	1	COMMANDANT ATTN AVIATION AGENCY US ARMY AVIATION SCHOOL FORT RUCKER AL 36360
1	COMMANDER ATTN D HARDISON US ARMY CONCEPTS ANALYSIS AGENCY 8120 WOODMONT AVE BETHESDA MD 20014	1	PRESIDENT ATTN ATZK AD S US ARMY ARMOR & ENGINEERING BOARD FORT KNOX KY 40121
1	DIRECTOR US ARMY BMD ADVANCED TECHNOLOGY CENTER PO BOX 1500 HUNTSVILLE AL 35807	1	DIRECTOR ATTN ATCD MA MAJ WILLIAMS HQ TRAC RPD FT MONROE VA 23651-5143
1	CHAIRMAN DOD EXPLOSIVES SAFETY BOARD HOFFMAN BLDG 1 ROOM 856-C 2461 EISENHOWER AVENUE ALEXANDRIA VA 22331-0600	1	HEADQUARTERS ATTN AMCICP AD M F FISETTE US ARMY MATERIEL COMMAND 5001 EISENHOWER AVE ALEXANDRIA VA 22333-0001
3	PROJECT MANAGER APGM ATTN AMCPM CW F MENKE AMCPM CWW AMCPM CWA H HASSMANN US ARMY ARDEC PCTNY ARSNL, NJ 07806-5000	1	COMMANDER ATTN SMCAR AEE B D DOWNS US ARMY ARDEC PCTNY ARSNL NJ 07806-5000
3	PEO ARMAMENTS PROJECT MANAGER ATTN AMCPM TMA K RUSSELL AMCPM TMA 105 AMCPM TMA 120 TANK MAIN ARMAMENT SYSTEMS PCTNY ARSNL NJ 07806-5000	2	COMMANDER ATTN SMCAR FSA T M SALSBURY SMCAR FSE T GORA US ARMY ARDEC PCTNY ARSNL NJ 07806-5000
1	DIRECTOR ATTN W KITCHENS BENET LABORATORIES US ARMY WATERVLIET ARSENAL WATERVLIET NY 12189	2	COMMANDER ATTN TECHNICAL LIBRARY D MANN US ARMY RESEARCH OFFICE PO BOX 12211 RSRCH TRI PK NC 27709-2211
		1	COMMANDER US ARMY BELVOIR R&D CENTER ATTN STRBE WC TECHNICAL LIBRARY VAULT BLDG 315 FORT BELVOIR VA 22060-5606
1	COMMANDER USACECOM ATTN ASQNC ELC IS L R MYER CENTER R&D TECHNICAL LIBRARY FORT MONMOUTH NJ 07703-5301	1	COMMANDER US ARMY TRAC FORT LEE DEFENSE LOGISTICS STUDIES FORT LEE VA 23801-6140

NO. OF COPIES	ORGANIZATION	NO. OF COPIES	ORGANIZATION
1	PRESIDENT US ARMY ARTILLERY BOARD FORT SILL OK 73503	3	COMMANDER ATTN 610 C SMITH 6110J K RICE 6110C S PETERS NAVAL SURFACE WARFARE CENTER INDIAN HEAD MD 20640-5035
1	COMMANDANT US ARMY COMMAND AND GENERAL STAFF COLLEGE FT LEAVENWORTH KS 66027-5200	2	COMMANDER ATTN CODE G33 T DORAN J COPLEY DAHLGREN VA 22448-5000
1	COMMANDANT ATTN REV AND TNG LIT DIV US ARMY SPECIAL WARFARE SCHOOL FORT BRAGG NC 28307	2	COMMANDER ATTN CODE 5B331 TECHNICAL LIBRARY NAVAL UNDERWATER SYSTEMS CENTER ENERGY CONVERSION DEPT NEWPORT RI 02840
1	COMMANDER ATTN SMCRA QA HI LIBRARY RADFORD ARMY AMMUNITION PLANT RADFORD VA 24141	1	COMMANDER ATTN CODE 388 C F PRICE NAVAL WEAPONS CENTER INFO SCIENCE DIV CHINA LAKE CA 93555-6001
1	COMMANDANT ATTN STSF TSM CN US ARMY FIELD ARTILLERY SCHOOL FORT SILL OK 73503-5600	1	AL TSTL TECHNICAL LIBRARY ATTN J LAMB EDWARDS AFB CA 93523-5000
1	DEPUTY COMMANDER ATTN SSFAE SD HVL STRATEGIC DEFENSE COMMAND PO BOX 1500 HUNTSVILLE AL 35887-8801	1	PENNSYLVANIA STATE UNIVERSITY DEPT OF MECHANICAL ENGR ATTN DR K KUO 312 MECHANICAL ENGINEERING BLDG UNIVERSITY PARK PA 16802
2	CDR US ARMY NGIC ATTN AMXST MC 3 S LEBEAU C BEITER 220 SEVENTH ST NE CHARLOTTESVILLE VA 22901	1	NORTH CAROLINA STATE UNIVERSITY ATTN J G GILLIGAN BOX 7909 1110 BURLINGTON ENGINEERING LABS RALEIGH NC 27695-7909
1	COMMANDANT ATTN ATSF CO MW B WILLIS USAFAC AND SCHOOL FORT SILL OK 73503	2	INSTITUTE FOR ADVANCED STUDIES ATTN DR H FAIR DR T KIEHNE 4030-2 WEST BAKER LANE AUSTIN TX 78759-5329
1	COMMANDER ATTN AIR 954 TECHNICAL LIBRARY NAVAL AIR SYSTEMS COMMAND WASHINGTON DC 20360	1	SRI INTERNATIONAL PROPULSION SCIENCES DIVISION ATTN TECHNICAL LIBRARY 333 RAVENSWOOD AVE MENLO PARK CA 94025
1	NAVAL RESEARCH LABORATORY TECHNICAL LIBRARY WASHINGTON DC 20375		

NO. OF COPIES	ORGANIZATION	NO. OF COPIES	ORGANIZATION
4	FMC CORPORATION ATTN MR G JOHNSON MR M SEALE DR A GIOVANETTI MR J DYVIK 4800 EAST RIVER RD MINNEAPOLIS MN 55421-1498	1	ELI FREEDMAN & ASSOCIATES ATTN E FREEDMAN 2411 DIANA RD BALTIMORE MD 21209
2	ALLIANT TECHSYSTEMS INC ATTN R E TOMPKINS J KENNEDY MN38-3300 10400 YELLOW CIRCLE DR MINNETONKA MN 55343	1	VERITAY TECHNOLOGY INC 4845 MILLERSPORT HWY PO BOX 305 EAST AMHERST NY 14051-0305
		1	BATTELLE TWSTIAC 505 KING AVE COLUMBUS OH 43201-2693
2	OLIN ORDNANCE ATTN V MCDONALD LIBRARY HUGH MCELROY PO BOX 222 ST MARKS FL 32355	1	GENERAL ELECTRIC CO ATTN DR J MANDZY DEFENSE SYSTEMS DIVISION MAIL DROP 43 220 100 PLASTICS AVE PITTSFIELD MA 01201
1	PAUL GOUGH ASSOCIATES INC ATTN P S GOUGH 1048 SOUTH ST PORTSMOUTH NH 03801-5423	1	STATE UNIVERSITY OF NEW YORK DR W J SARGEANT DEPT OF ELECTRICAL ENGNRNG BONNER HALL ROOM 312 BUFFALO NY 14260
1	PHYSICS INTERNATIONAL COMPANY ATTN LIBRARY H W WAMPLER 2700 MERCED ST SAN LEANDRO CA 94577	1	OFFICE OF NAVAL RESEARCH ATTN DR S G LEKOUDIS 800 NORTH QUINCY STREET ARLINGTON VA 22217
2	ROCKWELL INTERNATIONAL ATTN BA08 J E FLANAGAN J GRAY ROCKETDYNE DIVISION 6622 CANOGA AVE CANOGA PARK CA 9134	1	US ARMY MISSILE COMMAND ATTN AMSMI RD SS AT DR B J WALKER REDSTONE ARSENAL AL 35898
1	PRINCETON COMBUSTION RESEARCH LAB ATTN N MESSINA PRINCETON CORPORATE PLAZA 11 DEERPARK DRIVE BLDG IV SUITE 119 MONMOUTH JUNCTION NJ 08852	1	WRIGHT LABORATORY ATTN WL POPS DR BALU SAKAR WRIGHT PAT AFB OH 45433
		1	PRATT & WHITNEY ATTN DR S SYED MAIL STOP 715 89 PO BOX 109600 W PALM BEACH FL 33410-9600
2	SCIENCE APPLICATIONS INC ATTN J BATTEH L THORNHILL 1519 JOHNSON FERRY RD SUITE 300 MARIETTA GA 30062-6438	1	SDI DR L H CAVENY INNOVATIVE SCIENCE AND TECH THE PENTAGON WASHINGTON DC 20301-7100

NO. OF COPIES	ORGANIZATION	NO. OF COPIES	ORGANIZATION
1	UNITED DEFENSE LP ATTN DR J H KOO ARMAMENT SYSTEMS DIV MS M443 4800 EAST RIVER ROAD MINNEAPOLIS MN 55421	1	US ARMY RESEARCH OFFICE ATTN DR D MANN ENGINEERING SCIENCES DIVISION 4300 S MIAMI BLVD RSRCH TRI PK NC 27709
1	US ARMY ERDEC ATTN SCBRD RTM DR M MILLER APG MD 21010-5423	1	WRIGHT LABORATORY ATTN WL FIMG DR J SHANG WRIGHT PAT AFB OH 45433
1	DEPARTMENT OF THE AIR FORCE ATTN AFOSR DR J M TISHKOFF BLDG 410 ROOM 237A C WING BOLLING AFB DC 20332	1	INSTITUTE FOR DEFENSE ANALYSIS ATTN DR H WOLFHARD 1801 N BEAUREGARD STREET ALEXANDRIA VA 22311
1	NAVAL SURFACE WARFARE CENTER ATTN DR G MOORE DAHLGREN DIVISION DAHLGREN VA 22448	1	PHILLIPS LAB ASTRONAUTICS LAB ATTN OLAC PL RKFT DR P KESSEL BUILDING 8350 EDWARDS AFB CA 93523
1	NASA LANGLEY RESEARCH CENTER ATTN DR J M SEINER MAIL STOP 165 HAMPTON VA 23681-0001	1	GENERAL SCIENCES INC ATTN DR P ZAVITSANOS 205 SCHOOLHOUSE ROAD SOUDERTON PA 18964
1	PHILLIPS LAB ASTRONAUTICS LAB ATTN OLAC PL RKFT DR J LEVINE BUILDING 8350 EDWARDS AFB CA 93523	1	NASA MARSHALL SPACE AND FLIGHT CENTER ATTN DR P MCCONNAUGHEY MAIL CODE ED 32 MSFC AL 35812
1	INSTITUTE FOR APPLIED TECHNOLOGY ATTN DR W G REINECKE 4030 2 WEST BREAKER LANE AUSTIN TX 78759	1	NAVAL AIR WARFARE CENTER ATTN DR K C SCHADOW WEAPONS DIVISION CODE C02392 PROPULSION RESEARCH BRANCH CHINA LAKE CA 93555-6001
1	US ARMY CORP OF ENGINEERS ATTN DR J P BALSARA WATERWAYS EXPERIMENT STATION 3909 HALLS FERRY ROAD VICKSBURG, MS 39180-6199	1	NAVAL AIR WARFARE CENTER ATTN DR K A GREEN AIRCRAFT DIVISION OFFICE OF SCIENCE AND TECHNOLOGY CODE 4.0 MS 70 WARMISTER PA 18974-0591
1	DEPUTY COMMANDER ATTN CSSD WD L DR R BECKER US ARMY SP AND STRTGC DEFNS CMND PO BOX 1500 HUNTSVILLE AL 35807	1	DEPUTY DIRECTOR AEROPROPULSION ATTN H M BRILLIANT WRIGHT LABORATORY WRIGHT PAT AFB OH 45433

NO. OF COPIES	ORGANIZATION
1	PETC ATTN DR D WILDMAN COAL COMBUSTION R&D PITTSBURGH PA 15236
1	ARMY HIGH PERFORM CMPTG RSRCH CTR ATTN DR T TEZDUYAR UNIVERSITY OF MINNESOTA 1100 WASHINGTON AVE S SUITE 101 MINNEAPOLIS MN 55415
1	NASA AMES RESEARCH CENTER ATTN DR D COOPER NAS MS 258 5 MOFFET FIELD CA 94035
1	TRW DEFENSE SYSTEMS GROUP ATTN SR T C LIN BALLISTIC MISSILE DIVISION PO BOX 1310 BLDG 527 RM 706 SAN BERNARDINO, CA 92402
1	NAVAL POST GRADUATE SCHOOL ATTN DR D NETZGER DEPT OF AERONAUTICS HALLIGAN HALL BUILDING 234 MONTEREY CA 93943
1	PETC ATTN DR J EKMAN DIRECTOR COAL COMBUSTION R&D PITTSBURGH PA 15236
10	COMBUSTION RESEARCH & FLOW TECHNOLOGY INC 174N MAIN ST BLDG 3 PO BOX 1150 DUBLIN PA 18917
1	DR W J SARGEANT DEPT OF ELCTRCL ENGNRNG BONNER HALL RM 312 BUFFALO NY 14260

NO. OF COPIES	ORGANIZATION
	ABERDEEN PROVING GROUND
4	CDR USACSTA ATTN: S WALTON G RICE D LACEY C HERUD
1	DIR USAHEL ATTN J WEISZ
24	DIR USARL ATTN AMSRL-WT-PA, T MINOR G WREN (2 CP) W OBERLE (2 CP) P TRAN J DESPIRITO T COFFEE M NUSCA G KELLER D KOOKER F ROBBINS R ANDERSON G KATULKA K WHITE P CONROY S RAY A JUHASZ AMSRL-WT-PB, E SCHMIDT P PLOSTINS AMSRL-WT-PC, R FIFER AMSRL-WT-PD, B BURNS AMSRL-WT-WD, J POWELL AMSRL-WT-WG, P KASTE

NO. OF
COPIES   ORGANIZATION

  2   RARDE
         ATTN DR C WOODLEY
         DR G COOK
         GS2 DIVISION
         BUILDING R31
         FORT HALSTEAD
         SEVENOAKS KENT TN14 7BP
         ENGLAND

  1   WEAPONS SYSTEM DIVISION
         ATTN DR ANNA WILDEGGER-GAISSMAIER
         PO BOX 1500
         SALISBURY, SOUTH AUSTRALIA 5108

INTENTIONALLY LEFT BLANK.

USER EVALUATION SHEET/CHANGE OF ADDRESS

This Laboratory undertakes a continuing effort to improve the quality of the reports it publishes. Your comments/answers to the items/questions below will aid us in our efforts.

1. ARL Report Number __ARL-CR-240_____ Date of Report __August 1995_____

2. Date Report Received _____

3. Does this report satisfy a need? (Comment on purpose, related project, or other area of interest for which the report will be used.) _____

_____

_____

4. Specifically, how is the report being used? (Information source, design data, procedure, source of ideas, etc.)

_____

_____

_____

5. Has the information in this report led to any quantitative savings as far as man-hours or dollars saved, operating costs avoided, or efficiencies achieved, etc? If so, please elaborate. _____

_____

_____

6. General Comments. What do you think should be changed to improve future reports? (Indicate changes to organization, technical content, format, etc.) _____

_____

_____

_____

CURRENT
ADDRESS

_____
Organization

_____
Name

_____
Street or P.O. Box No.

_____
City, State, Zip Code

7. If indicating a Change of Address or Address Correction, please provide the Current or Correct address above and the Old or Incorrect address below.

OLD
ADDRESS

_____
Organization

_____
Name

_____
Street or P.O. Box No.

_____
City, State, Zip Code

(Remove this sheet, fold as indicated, tape closed, and mail.)
(DO NOT STAPLE)

DEPARTMENT OF THE ARMY

OFFICIAL BUSINESS

BUSINESS REPLY MAIL
FIRST CLASS PERMIT NO 0001, APG, MD

POSTAGE WILL BE PAID BY ADDRESSEE

DIRECTOR
U.S. ARMY RESEARCH LABORATORY
ATTN: AMSRL-WT-PA
ABERDEEN PROVING GROUND, MD 21005-5066